The University Of Sheffield.

Doctoral Thesis

Development and Applications of Near- and Mid-infrared OCT

Wai Ching Lin

Supervised by Prof Stephen J. Matcher

Thesis submitted to the University of Sheffield

in fulfilment of the requirements for the degree of Doctorate of Philosophy

Electronic & Electrical Engineering

24 September 2021

Abstract

This thesis chronicles the development of a mid-infrared optical coherence tomography (MIR-OCT) system and various applications of near-infrared (NIR) OCT. With regards to the development of MIR-OCT, the ultimate goal is to build a swept-source system with a commercial external cavity quantum cascade laser, using heterodyne detection to improve the signal-to-noise ratio. We have characterized the sources of noise within the system: quantization noise from the analogue-to-digital convertor, shot noise from the detectors and relative intensity noise (RIN) of the laser. By using pulse-to-pulse normalization with two paired detectors, the RIN measured can be reduced -97dB/Hz to -115dB/Hz. Next, we investigate the feasibility of using polarization-sensitive OCT to quantify the severity of striae distensae. We have shown that the estimated tissue birefringence of striae-affected skin is significantly greater (p<0.001) than visually normal skin. There is also a loose correlation between tissue birefringence and the subjective visual scores. In botany, we have shown that even with a weak acid treatment, it is possible to quantify the effect of acid erosion on teeth. Calculating the slope of the reflectivity profile is a reliable method for quantifying and potentially monitoring the demineralisation of teeth. The results show that the initial reflectivity readings before treatment is an important factor in determining the magnitude of reflectivity changes after treatment. In botany, we aimed to investigate the stability of plant petiole diameter measurements using OCT. We have demonstrated that spectrometer-based OCT can accurately track changes in the diameter of plant petioles, with an accuracy of ~1.0 µm. With regards to biofilm, we aimed to determine whether there is a minimum detectable limit when OCT is used for the quantification of biofilm thickness, and have shown that biofilm as thin as 13.1 µm can be measured.

Acknowledgements

I am sincerely grateful to the following people who have helped me throughout my PhD:

My supervisors Prof Stephen Matcher and Dr Kristian Groom, for their insight, guidance and support during my PhD.

Prof Michael Cork and Dr Simon Danby from the Department of Infection, Immunity and Cardiovascular Disease, for their support and discussions on striae distensae.

Prof Paul Hatton and Dr Reham Kilano from the School of Clinical Dentistry, for the preparation of teeth samples.

Dr Adrien Chauvet, Ms Shuangyue Wang and Mr Joseph Williams from the Department of Chemistry, for providing Arabidopsis plant samples.

Dr Katherine Fish and Dr Frances Pick from the Department of Civil and Structural Engineering, for preparation of biofilm samples and discussions on biofilm.

Dr Dmitry Revin, Dr Zenghai Lu, Dr Robert Byers and Dr Wei Li, for their generous assistance in the operation of OCT systems and image processing techniques.

The University of Sheffield and the EPSRC, for their financial support.

And my family and friends, who have always encouraged and supported me.

List of Publications

Journal articles

W.C. Lin, R.A. Byers, W. Li, S.G. Danby, M.J. Cork, and S.J. Matcher, “Imaging striae distensae: a comparison between PS-OCT and digital dermoscopy,” Biomedical Optics Express, 12(6), 3296-3311 (2021).

Conference proceedings

W.C. Lin, and S.J. Matcher, “Swept-source OCT using pulsed mid-infrared light,” Label-free Biomedical Imaging and Sensing, International Society for Optics and Photonics 10890, 108902D (2019).

W.C. Lin, D.G. Revin, and S.J. Matcher, “Methods for reducing relative intensity noise in swept-source mid-infrared OCT,” Biomedical Spectroscopy, Microscopy, and Imaging, International Society for Optics and Photonics 11359, 113590P (2020).

J. Williams, **W.C. Lin**, W. Li, S. Wang, S.J. Matcher, and A.A. Chauvet, “Translating Optical Coherence Tomography Technologies from Clinical Studies to Botany: Real Time Imaging of Long-Distance Signalling in Plants,” Optical Coherence Tomography, Optical Society of America, OM4E-6 (2020).

Contents

List of Figures

List of Tables

List of Abbreviations

ADC	analogue-to-digital convertor
AOC	assimilable organic carbon
CMOS	complementary metal-oxide semiconductor
CPP-ACP	casein phosphopeptide-amorphous calcium phosphate
DEJ	dentine-enamel junction
EC-QCL	external cavity quantum cascade laser
FDML	Fourier domain mode locking
FD-OCT	Fourier-domain OCT
FFT	fast Fourier transform
FTIR	Fourier transform infrared (spectroscopy)
FWHM	full width at half maximum (bandwidth)
GUI	graphical user interface
HDPE	high density polyethylene
LP	linear polarizer
MIR	mid-infrared
NIR	near-infrared
ND	neutral density (filter)
OCT	optical coherence tomography
OPD	optical path difference
PBS	polarizing beam splitter
PC	polarization controller
PMC	polarization-maintaining coupler
PS-OCT	polarization-sensitive OCT
QWP	quarter wave plate
RIN	relative intensity noise
RNFL	retinal nerve fibre layer
SA	striae alba
SD	striae distensae

SD-OCT	spectral-domain or spectrometer-based OCT
SE	standard error
SLD	superluminescent diode
SNR	signal-to-noise ratio
SS-OCT	swept-source OCT
SR	striae rubra
TD-OCT	time-domain OCT

Chapter 1: Introduction & Literature Review

Since its advent in 1991 [1], optical coherence tomography (OCT) has become a method of choice for clinical fields such as ophthalmology and angiography. Huang et al. were the first to demonstrate the power of OCT as an imaging modality, using it to produce the first OCT images of the human retina and coronary artery [1]. The images were obtained using an 830 nm wavelength near-infrared (NIR) light source and had an axial resolution of 15 µm. OCT measures the backscatter of tissue illuminated with infrared light, allowing subsurface morphology within the tissue to be resolved. Typically, light from near-infrared region (750 – 1500 nm wavelengths) is used, as the penetration of light in the mid-infrared (MIR) region (1.5 – 4 µm wavelengths) is highly attenuated by water absorption.

The prevalence of OCT in modern medicine can be partially attributed to the niche it fills between high resolution and high penetration imaging modalities. The mechanism of action used in OCT is comparable to other imaging modalities such as confocal microscopy and ultrasound. Ultrasound is the acoustic analogue of OCT, measuring the echo time delay of ultrasound waves transmitted deep within tissues. The resolution of ultrasound varies depending on the sound wave frequency used (3-40 MHz) but is typically 0.1-1 mm [2]. It is possible for ultrasound to have penetration depths of several centimetres. By increasing the ultrasound frequency, finer resolutions (15-20 µm) have been achieved at the cost of penetration depth. Conversely, confocal microscopy has micrometre resolution but much poorer depth penetration [3]. Confocal microscopy uses pinhole apertures and objective

lenses with high numerical aperture to focus light onto a specific focal plane within a tissue sample, enabling high resolutions of around 1 µm. Due to tissue being highly optically scattering, the effective imaging depth is restricted to hundreds of microns. The axial resolution of OCT ranges between 1-10 µm, where tissue morphology can be resolved. As tissue is highly optically scattering, light is highly attenuated within tissues and penetration depths are limited to around 2mm [4]. OCT has approximately 10 times greater penetration depth than confocal microscopy and 10-100 times better resolution compared to ultrasound.

As well as its high-resolution capabilities, the popularity of OCT is spurred by the development and commercialisation of fibre optics, enabling the manufacture of OCT systems to be relatively low cost, portable and commercially viable [4]. Early OCT systems used the time-domain method, which consists of a Michelson interferometer with a moving reference mirror. Improvements to OCT initially focussed on improving the design of the reference arm to increase image acquisition speeds, in addition to designing more spatially coherent broadband light sources to improve resolutions. The development of spectrometer-based detectors and tunable lasers propelled the switch from time-domain OCT into Fourier-domain OCT, which greatly improved sensitivity and acquisition speeds by 50-100 times. Currently, Fourier-domain OCT systems dominate the market and have been widely accepted into clinical practice, particularly in ophthalmology and cardiology. This literature review will discuss the development of OCT from time-domain to Fourier-domain.

1.1 Time-domain OCT

OCT measures the echo time delay of backscattered light. A typical time-domain (TD) OCT utilizes the Michelson interferometer setup, as shown in Fig. 1.1. It consists of a light source,

a beam splitter, a reference arm mirror and a photodetector. A beam splitter splits the light beam into a reference beam and sample beam. The beam splitting ratio can vary. The highest fringe contrast is achieved when the two interfering light beams have similar intensities. As the sample in the sample arm attenuates light more than the mirror in the reference arm, a 99:1 or 90:10 ratio, with the higher intensity light going into the sample arm, may give the optimal fringe contrast.

The reference beam reflects off a mirror and returns to the beam splitter, where it interferes with reflected light from the sample arm. Biological tissue often consists of several layers with varying refractive indices. When light from the sample arm is directed at the sample, some light is backscattered when it hits a refractive index discontinuity. This backscattered light is reflected onto the beam splitter once more, where it interferes with light returning from the reference arm.

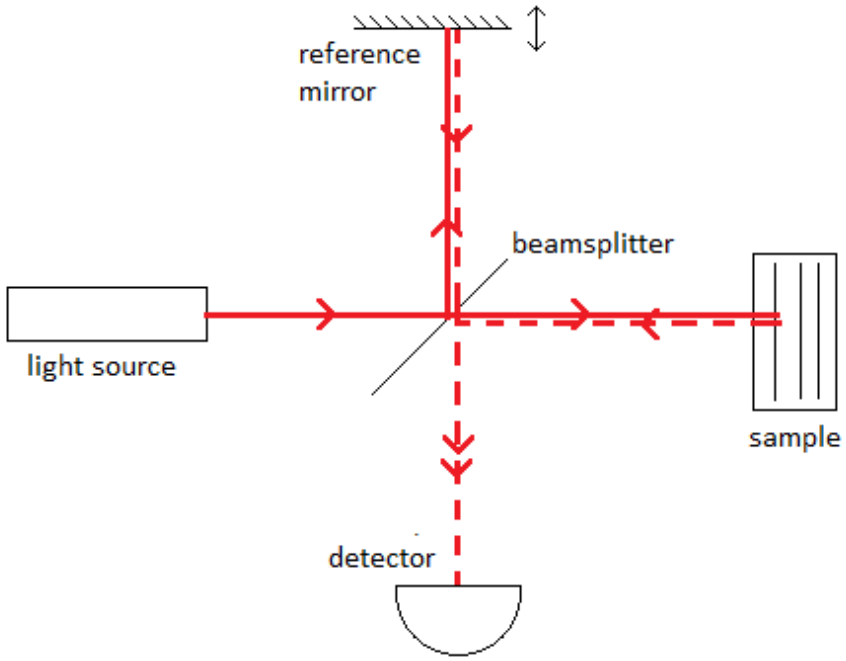

Figure 1.1. Diagram of a typical time-domain OCT setup. A spatially coherent, broadband light source in the near-infrared spectrum is split using a beam splitter into reference and sample arms. A moving mirror in the reference arm translates linearly over time to collect an A-scan. The interference between light from both arms is detected on a single photodetector.

The electric field of the incident light beam $\mathrm{E_{in}}$ can be expressed as a complex exponential (Eq. 1.1), which is a function of frequency ω and time t. $s(\omega)$ is the amplitude spectrum of the source field.

$$\mathrm{E_{in}}(\omega, t) = s(\omega)e^{-i\omega t} \tag{1.1}$$

If the beam splitter transmittance in the reference and sample arms is T_r and T_s respectively, such that $T_r + T_s = 1$, then the optical fields in the reference and sample arms can be written as:

$$\mathrm{E_r}(\omega, t, \Delta z) = \sqrt{T_r T_s}E_{in}(\omega, t)e^{-i\phi(\Delta z)} \tag{1.2}$$

$$\mathrm{E_s}(\omega, t) = \sqrt{T_r T_s}E_{in}(\omega, t)H(\omega) \tag{1.3}$$

Where Δz is the geometric distance translated by the reference mirror, $\phi(\Delta z)$ is the phase accumulated when translating over this distance, and $H(\omega)$ is the frequency domain response function of the sample. As the sample has unknown refractive indices at unknown depths, the sample response function $H(\omega)$ can be described as the sum of all reflected light at varying depth z,

$$H(\omega) = \int_{-\infty}^{\infty} r(\omega, z)\exp\left(\frac{i2n(\omega,z)\omega z}{c}\right)dz \tag{1.4}$$

where for any reflective structure within the sample, $r(\omega, z)$ is the backscattering co-efficient and $n(\omega, z)$ is the refractive index [5]. We can see from this equation that the backscattering co-efficient and refractive index is a function of both frequency ω and distance z. In TD- OCT, the distance is changed to obtain information about the sample response function, whereas in Fourier-domain OCT, the frequency is changed.

The resulting interferogram $\mathrm{E_{out}}(\omega, t, \Delta z)$ would be a summation of Eq. 1.2 and Eq. 1.3. In OCT, square law intensity detectors are used, where the light intensity detected is the time average of the $\mathrm{E_{out}}(\omega, t, \Delta z)$ multiplied by its complex conjugate, i.e.:

$$\mathrm{I}(\omega, \Delta z) = \langle E_{out}(\omega, t, \Delta z) E^*_{out}(\omega, t, \Delta z) \rangle \tag{1.5}$$

It has been previously shown [5] that the intensity detected is given by:

$$\mathrm{I}(\omega, \Delta \mathrm{z}) = \mathrm{T_r} T_s S(\omega) |H(\omega)|^2 + T_r T_s S(\omega) + 2 T_r T_s \Re\{S(\omega) H(\omega) e^{-i\phi(\Delta z)}\} \tag{1.6}$$

where the first two terms denote the intensities of the sample and reference arms respectively, while the last term represents the interference term. $S(\omega)$ is the intensity spectrum of the source amplitude spectrum $S(\omega) = |s(\omega)|^2$, and $\Re$ refers to the real part of the complex term.

To measure the depth profile or an A-scan of the sample, the reference arm mirror is translated over time in the z-direction and an axial 'interferogram' is recorded. At a refractive index discontinuity, some light is reflected. This light only produces an interference signal when the optical path difference between the sample and reference arms (OPD) is less than the coherence length l_c.

To obtain a two-dimensional image or a B-scan, a galvanometer mirror is typically added to the sample arm and translates in the *x*-direction; the sample is scanned in a raster pattern. A three-dimensional image or C-scan is obtained in a similar manner, with a second galvanometer mirror translating in the *y*-direction.

1.1.1 Axial and lateral resolutions

In TD-OCT, the light source is a broadband polychromatic beam. The interference pattern obtained is modulated by the coherence function of the light source $\gamma(z)$ [4]. The coherence function can be approximated as a Gaussian function with the full-width at half-maximum (FWHM) of the Gaussian function being the coherence length l_c. The Fourier transform of the coherence function $\gamma(z)$ is the Gaussian-shaped source intensity spectrum $S(\omega)$. The source intensity spectrum has a central frequency ω_0 and a bandwidth $\Delta\omega$. The wavelength λ can be calculated from the frequency with the formula $\lambda = 2\pi c/\omega$, where c is the speed of light. Thus, the coherence length and axial resolution of an OCT system is given by the equation [6]:

$$l_c = \Delta z = \frac{2ln2}{\pi}\frac{\lambda_0^2}{\Delta\lambda} \tag{1.7}$$

λ_0 is the central wavelength and $\Delta\lambda$ is the FWHM bandwidth of the light source. Decreasing the central wavelength and/or increasing the bandwidth leads to a smaller axial resolution. Work by Schmitt et al. showed that using light of longer wavelengths led to less scattering and greater penetration depths at the expense of the axial resolution [7]. Advances in laser light sources led to improvements in axial resolutions. The first OCT systems [1,4] used broadband light sources, such as the relatively low-cost GaAs superluminescent diodes (SLDs) with a central wavelength of around 800 nm and a bandwidth of 30 nm. In 1995, Bouma et al. developed a Kerr-lens mode-locked Ti:Al_2O_3 femtosecond laser with a 800 nm central wavelength, which had a maximum bandwidth of 350 nm [8]. This gave the subsequent OCT system an axial resolution of 1 µm [9]. Cr^{4+}:Forsterite lasers have been developed by Chudoba et al. with a longer central wavelength of 1300 nm and a 250 nm bandwidth [10], achieving

resolutions of less 5 µm [11]. From an axial resolution of 10-15 µm in early OCT systems, today, ultrahigh resolutions of 2-3 µm can be achieved [12].

An advantage of OCT over other imaging systems such as confocal microscopy is that the axial resolution is decoupled from the lateral resolution. This means that the axial resolution would not be affected when the optical components within an OCT system are changed, for example to achieve the smallest lateral resolution. The lateral resolution of an OCT system in air is given as follows [4].

$$\Delta x = \frac{4\lambda_0 f}{\pi d} \tag{1.8}$$

f is the focal length of the objective lens and *d* is the diameter of the incident laser beam. A smaller central wavelength λ_0 would result in a smaller lateral resolution. For a smaller lateral resolution, the focussing optics used need to produce a sample arm beam that has a large beam diameter and short focal length. The numerical aperture (*NA*) is a term often used to characterize the angle of the incident beam. It is proportional to the beam diameter *d* and inversely proportional to the focal length *f* via the equation:

$$NA = n\frac{d}{2f} \tag{1.9}$$

where *n* is the refractive index of the sample. In Eq. (1.8), we assume that the sample is air, which has a refractive index of 1.

1.1.2 Design improvements to TD-OCT

The design of an OCT system is essentially modular, and separate parts of the system can be conveniently exchanged to improve performance. Endoscopic probes and catheters can be attached to the sample arm to make the OCT system suitable for applications such as

endoscopic and intravascular imaging. The addition of optical circulators, unbalanced couplers and the use of balanced heterodyne detection has been shown by Rollins et al. to reduce noise and hence improve the signal-to-noise ratio (SNR) of OCT systems [13]. This is based on previous work by Abbas et al., which demonstrated that a balanced homodyne or heterodyne detection system using two detectors can suppress excessive relative intensity noise [14].

The development of femtosecond lasers has aided in improvements of image acquisition rates. Although various instruments for the reference arm have also been designed to improve imaging speeds, TD-OCT systems are limited by the rate at which the galvanometer mirror can translate, i.e. by the design of the optical delay line. First commercial OCT systems, introduced in 1996 for ophthalmic applications by Carl Zeiss Meditec, had speeds of around 100 A-scans/s [4]. Kwong et al. utilised tilting mirrors to achieve mechanical scanning speeds of 400 Hz [15]. Other designs include using a retroreflector [16], a rotating prism [17] and a rotary optical delay line [18]. However, due to the inertia that has to be overcome in mechanically scanning a galvanometer, such improvements in design only increased the axial scanning speeds up to several kilohertz. For more significant improvements in imaging speeds, a paradigm shift in the interferometer setup is required.

1.2 Fourier-domain OCT

The concept of a Fourier-domain (FD) OCT system, where interferometric information can be recorded without translating the reference arm, was introduced by Fercher et al. in 1995 [19]. They proposed a spectrometer-based system, where a spectrometer coupled with a line scan camera replaces the detector of a TD-OCT system. In 2003, Choma et al. demonstrated the

sensitivity and speed advantage of FD-OCT systems over their TD-OCT counterparts by 50-100 times [20]. In the same year, these results were observed separately by de Boer et al. [21] and Leitgeb et al [22]. FD-OCT systems have a sensitivity improvement by a factor of *N*, where *N* is the number of pixels in an axial scan. They can be divided into spectrometer-based or spectral-domain (SD) OCT, and swept-source (SS) OCT.

1.2.1 Spectral-domain OCT

Initially proposed by Fercher et al. in 1995 [19], the first in vivo retinal imaging using SD-OCT was performed by Wojtkowski et al. in 2002 [23]. In 2004, Nassif et al. recorded images of the macula and optic nerve head with a 6 µm axial resolution and an imaging speed of 29 000 A-scans per second, demonstrating the ability of FD-OCT systems to collect images at video rate. Furthermore, such high acquisition speeds allowed for volumetric three-dimensional and en face imaging to be possible [24,25]. Fig. 1.2 shows a schematic of SD-OCT.

In an SD-OCT system, the intensity spectrum over a frequency range is measured using a spectrometer, which is typically a linear photodetector array coupled to a diffraction grating. Like the TD-OCT setup in Fig. 1.1, the light source is a broadband laser. Unlike the TD-OCT setup, the mirror in the reference arm is fixed. The spectrometer uses a diffraction grating to split the incident light into different wavelengths and a line-scan camera to detect the interference signal with respect to the wavelength.

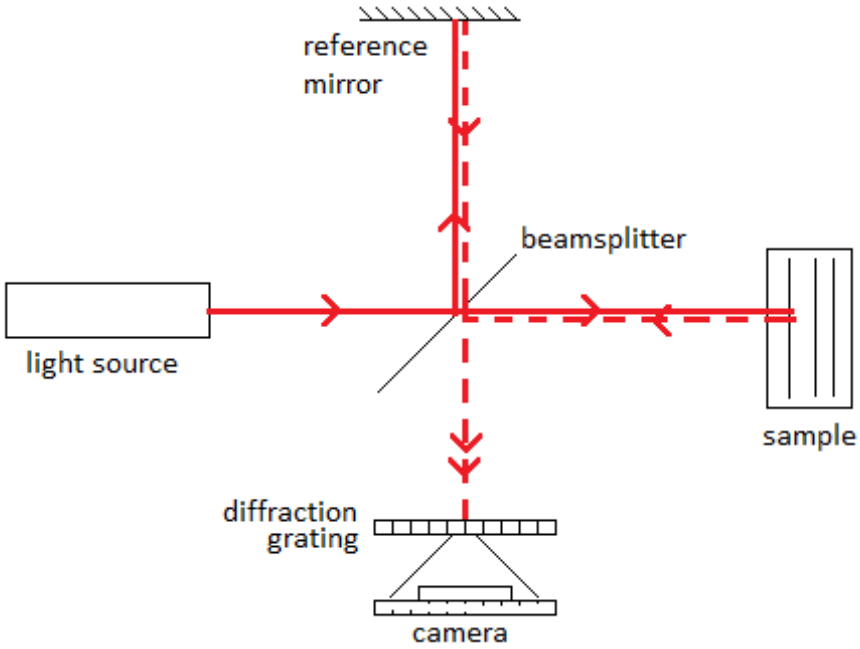

Figure 1.2. Diagram of spectral-domain OCT. The intensity spectrum over a frequency range is measured using a spectrometer, which is typically a linear photodetector array coupled to a diffraction grating. The reference mirror is fixed.

When the reference mirror is stationary, i.e. $\Delta z = 0$, and we assume that the beamsplitter splits the light intensity equally into reference and sample beams ($T_r = T_s = 0.5$), then Eq. 1.6 can be simplified into [5]:

$$I(\omega) = \frac{1}{4} S(\omega)\{H(\omega) + 1\}^2 \tag{1.10}$$

Eq. 1.10 shows that the detected intensity spectrum $I(\omega)$ needs to be 'demodulated' from the intensity source spectrum $S(\omega)$ to extract the frequency response function of the sample $H(\omega)$. This is done by dividing the intensity spectrum by the measured intensity source spectrum. The depth-resolved reflectivity profile or A-scan can then be obtained by performing a Fourier transform on the intensity spectrum, i.e. $I(t) = FT\{I(\omega)\}$, where *FT* represents the Fourier transform. The time variable t in this equation represents the optical time of flight, which can then be converted into the equivalent geometric distance Δz in a TD-OCT system. B-scans and C-scans are obtained similarly to TD-OCT.

A limitation of SD-OCT is the presence of mirror artefacts within the B-scan, which happen when samples are positioned too close to the point of zero OPD. This is because a Fourier transform of the data is symmetrical about the zero frequency. Positive frequencies of the Fourier transform correspond to the axial reflectivity profile, while the negative frequencies contain these mirror artefacts. The result is that the sample appears to "fold" over the top of the B-scan. Another consequence of the symmetrical nature of the Fourier transform is that line scan cameras with *N* number of pixels produce an image with *N/2* pixels in an A-scan. This is because the Fourier transform, which is performed to obtain the reflectivity profile, is symmetrical about the zero-frequency axis. Thus, line scan cameras with a high number of pixels are required to produce images of high axial resolution.

Another limitation is the axial scanning speed of the SD-OCT system, which is limited by the speed at which the line scan camera can acquire data. Improvements to SD-OCT imaging speeds focus on developing better high-speed line scan cameras and rates of 312 500 A-scans per second have been achieved with the use of an ultrahigh speed CMOS (complementary metal-oxide semiconductor) line scan camera [26].

1.2.2 Swept-source OCT

In SD-OCT, line scan cameras are limited in the range of wavelengths that they can detect. Typically, cameras that can detect wavelengths of over 1000 nm are InGaAs cameras, which are more expensive [4]. The axial resolution and scanning rate in SD-OCT are determined by the pixel resolution and acquisition speed of the camera. SS-OCT systems only require photodetectors like those used in TD-OCT systems. Instead, the light source is tuned over a wavelength range in a ramp function over time. A single sweep of the wavelength range

corresponds to a single A-scan. The wavelength range over which the laser is swept determines the axial resolution; the rate at which the laser performs one sweep determines the A-scan acquisition rate.

Fig. 1.3 (left) shows a schematic of an SS-OCT setup. It has a Michelson interferometer setup like TD-OCT with the main difference being the light source. In SS-OCT operation, the wavelength of the light source varies, or sweeps, as a function of time. A single sweep corresponds to one axial scan. Although the laser has a broad bandwidth, at any point in time, the output spectrum has a much narrower linewidth. If the wavelength λ increases linearly as a function of time, then it can be written as $\lambda(t) = \lambda_{min} + \alpha t$, where $\lambda_{\min}$ is the starting wavelength, α is the rate at which the laser sweeps. The detected intensity spectrum is the same as that of SD-OCT in Eq. 1.10, where the reflectivity profile is obtained by performing a Fourier transform. As with the SD-OCT, light of a longer wavelength corresponds to greater sample depth.

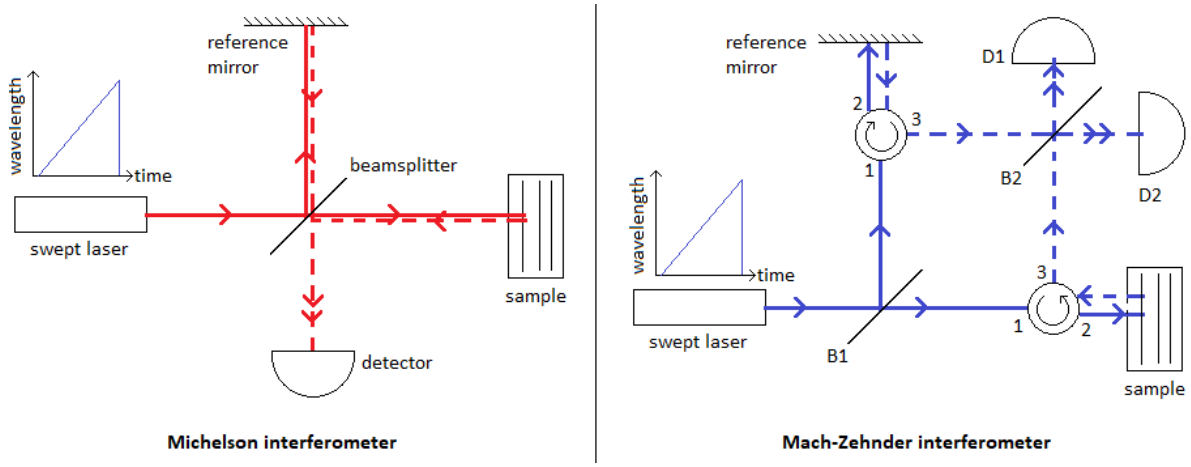

Figure 1.3. Diagram of swept-source OCT using a Michelson interferometer (left) and a Mach-Zehnder interferometer (right). In SS-OCT operation, the wavelength of the light source varies, or sweeps, as a function of time.

Some SS-OCT setups make use of a Mach-Zehnder interferometer, like the one shown in Fig. 1.3 (right). Here, with the use of optical circulators, backscattered light from both sample and

reference arms pass through a second beamsplitter (B2). The interferometric signal gets detected simultaneously by two matched photodetectors (D1 and D2). This balanced dual detection enables relative intensity noise to be removed from the signals, thus improving the SNR. Relative intensity noise is defined as fluctuations in laser output, where a higher power output results in more noise.

SS-OCT relies heavily on the specifications of the laser itself. The most important requirements are that the laser must sweep its wavelength at a high speed, with a wide bandwidth but narrow instantaneous linewidth. The first demonstration of SS-OCT utilised an external cavity semiconductor laser with a central wavelength of 840 nm, capable of tuning the entirety of its spectral bandwidth of 25 nm in 100ms [27]. In the same year, Golubovic et al. demonstrated an SS-OCT system using a Cr^{4+}:Forsterite laser with sweep rates of 75 nm in 500 μs [28]. However, this only gave an axial scanning speed of 2 kHz and an axial resolution of 15 μm, which offered no speed or resolution advantage compared to standard TD-OCT systems at that time. Within the swept laser, the two major components are the laser gain chip, which generates the laser emissions, and a tunable filter, which enables sweeping by tuning the wavelength. Early development in swept lasers have focussed on designing better filters to achieve better tuning rates, such as the use of a polygon-based mirror filter [29] and a Fabry-Perot filter [30]. In 2006, Huber et al. demonstrated that the technique of Fourier Domain Mode Locking (FDML) enabled up to 290 kHz sweep rates for a tuning range of 105 nm [31]. This breakthrough enabled high speed OCT systems to be developed for endoscopic imaging [32,33].

1.2.3 Detection sensitivity

In an OCT system, sensitivity is defined as the ratio between the detected intensity signal i_s^2 and the noise of the system i_n^2. This is also known as the signal to noise ratio (SNR):

$$SNR = {i_s^2}/{i_n^2} \tag{1.11}$$

There are four major noise sources within an OCT system: quantization noise from the analogue-to-digital convertor (ADC), shot noise from the detector photodiode, thermal noise from the detector electronics and laser relative intensity noise (RIN). All the noise sources sum up in quadrature:

$$i_n^2 = i_{adc}^2 + i_{sh}^2 + i_{th}^2 + i_{rin}^2 \tag{1.12}$$

where i_{adc}^2 is the ADC noise and i_{sh}^2 is the detector shot noise. i_{rin}^2 and i_{th}^2 represents laser RIN noise and thermal noise respectively.

Quantization noise refers to the error produced when the ADC discretizes a continuous-time signal. It is proportional to the quantization step size Δ and is represented by the formula [34]:

$$i_{adc} = \frac{\Delta}{\sqrt{12}} \tag{1.13}$$

Shot noise refers to the random arrival of photons reaching a photodiode, leading to random fluctuations in the detected photocurrent. It is dependent on the dc photocurrent i_{dc}, the measurement bandwidth *B* and the detector quantum efficiency q_e [5]:

$$i_{sh} = \sqrt{2 q_e i_{dc} B} \tag{1.14}$$

Laser RIN describes fluctuations in the laser power output and depends on the dc photocurrent i_{dc}, the measurement bandwidth *B* and the source spectral bandwidth $\Delta\omega$ [5]:

$$i_{rin} = i_{dc}\sqrt{\frac{B}{2\pi\Delta\omega}} \tag{1.15}$$

Thermal noise or Johnson-Nyquist noise refers to the agitation of electrons within the detector electronics caused by thermal energy. A higher temperature increases thermal noise. Thermal noise is represented by the equation [5]:

$$i_{th} = \sqrt{\frac{4kTB}{R_{eff}}} \tag{1.16}$$

where k is the Boltzmann's constant, T is the temperature in Kelvin and R_{eff} is the effective resistance in the detector electronics.

When a pair of balanced photodetectors are used in the Mach-Zehnder setup in Fig. 1.3, RIN and thermal noise in the detectors are correlated and can be rendered negligible, either during post-processing or via a differential amplifier. If the ADC has a small quantization step size, the detector shot noise is much larger than the ADC noise, i.e. $i_{adc} \ll i_{sh}$. Thus, the overall noise is dominated by shot noise $i_n = i_{sh}$. Shot-noise-limited sensitivity is the goal when trying to increase the sensitivity of an OCT system.

1.3 Mid-infrared OCT

Most conventional OCT systems rely on near-infrared (NIR) lasers. Current commercial systems typically use light sources with central wavelengths of around 1300 nm. There are several reasons why there is an absence of MIR OCT in literature. Firstly, light in the mid-infrared region is strongly attenuated in biological tissues, as much of it is absorbed by water. Little light is backscattered or back-reflected from the sample, which limits penetration depth. Secondly, an increase in the central wavelength of the light source lowers the axial resolution

of the image. Thirdly, OCT systems, especially swept-source OCT, depend on lasers to produce light of a specified wavelength and until recently, there has not been a spatially coherent tunable swept laser that could produce light in the mid-infrared region. Recently, in-house and commercial external cavity quantum cascade lasers (EC-QCL) have become available [35-37], kickstarting the development of MIR OCT.

Quantum cascade lasers were first realized by Faist et al. in 1994 [38]. Initial QCLs suffered from a limited tuning range of around 10 cm^{-1} [39]. With the aid of diffraction grating, external cavity QCLs demonstrated a higher tuning range of 54 cm^{-1} [40] and even up to 430 cm^{-1} [41]. The first commercial EC-QCL was marketed in 2006 [37].

Colley et al. were the first to demonstrate a MIR TD-OCT system, using an in-house broadband continuous wave QCL in the 6-8 µm wavelength range [35]. The QCL is driven by 300 V 150 ns square pulses at a repetition rate of 10 kHz [42]. The OCT system has an axial resolution of 11µm, a lateral resolution of 45µm and a depth penetration of 460µm. The QCL emission spectrum was measured, before imaging a CaF_2 window of known thickness, as well as glass-embedded gold/palladium-coated collagen constructs. Their system ran into challenges in terms of the relatively poor SNR compared to NIR TD-OCT systems. Areas of improvement include switching to faster FD-OCT systems, better QCL lasers that have sufficiently high optical power and broad bandwidth, and using a fibre-based Mach-Zehnder interferometer setup to improve the SNR.

The first MIR FD-OCT system was a spectral-domain system demonstrated by Zorin et al [43]. The supercontinuum light source used had a central wavelength of 4 µm and a pyroelectric linear array was used to measure the interferometric signal. The system achieved a scanning

speed of 2.5 A-scan/s and was 20 dB more sensitive than the TD-OCT system demonstrated by Colley et al.

Recently, Freer et al. demonstrated a MIR OCT system using a pulsed swept-source laser [44]. The light source was an in-house swept-source QCL that could generate pulses in the tuning range of 6-8 µm. The QCL used was built by Childs et al. and could achieve pulse repetition rates of more than 100 kHz [36]. Freer et al. used the MIR OCT system to collect A-scans from three samples: a mirror, a calcium fluoride sample with germanium coating on one side and another calcium fluoride sample with double-sided germanium coating. The laser was pulsed at a 5 kHz repetition rate and a sweep rate of 1 Hz. The maximum SNR was calculated to be 16 dB and the maximum axial depth was 3.5 mm.

1.4 Polarization-sensitive OCT

Polarization-sensitive (PS) OCT is a functional extension of OCT that can measure the polarization state of the interferometric signal. The addition of such information allows the birefringence and depolarization of a sample to be calculated [45]. PS-OCT is often used to interrogate fibrous tissues such as muscles and tendons [46], and has been used in ophthalmology [46] and dermatology [47]. These types of tissues are optically anisotropic, where the refractive indices of the tissue changes depending on the direction of the incident light. For instance, PS-OCT has been used to measure changes in retardance in the retinal nerve fibre layer (RNFL), to monitor the onset and progression of glaucoma [48]. Utilizing information about polarization changes allows for the earlier detection of the disease, compared to conventional OCT which only measures the RNFL thickness.

PS-OCT uses circularly polarized light to measure the phase retardance and fast axis orientation of birefringent tissue [49-52]. The setup of PS-OCT systems can vary and can be time-domain [49], spectral-domain [53] or swept-source systems [54]. Fig. 1.4 shows a schematic of a generic PS-OCT system. The system can be modified into different setups depending on the type of light source or detector used. For instance, a SS-OCT system would use a swept laser, while a TD-OCT system would have a movable reference mirror. The PS-OCT system includes a linear polarizer (LP), which converts light from the laser source into vertically polarized light. The beam to the reference arm passes through a quarter wave plate (QWP1) oriented at 22.5°, as passes through it once more when it is back-reflected from the mirror. In the sample arm, the quarter wave plate (QWP2) is oriented at 45°, which converts the linearly polarized light into circularly polarized light. The interferometric signal passes through a polarizing beamsplitter. This separates the signal into two orthogonal polarization states (horizontal and vertical), which are detected by two detectors (D1 and D2).

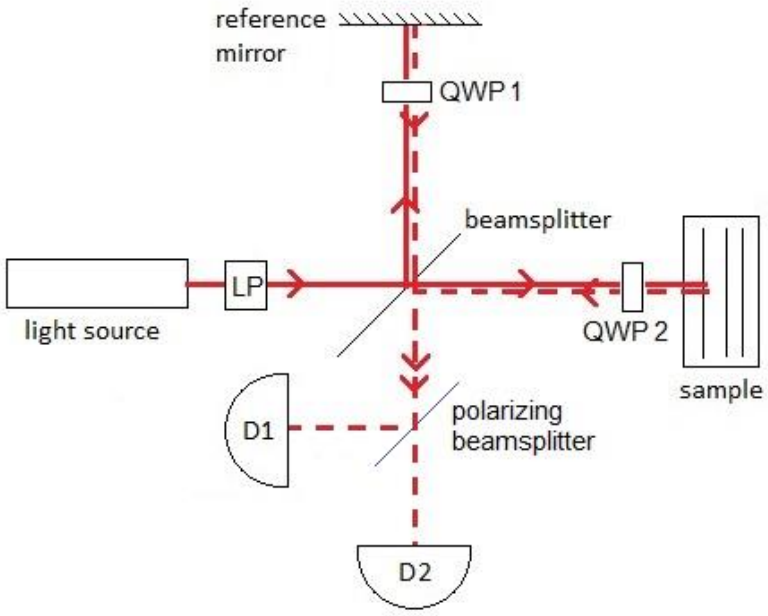

Figure 1.4. Schematic of a polarization-sensitive OCT system. Additional components included are: linear polarizer (LP) to convert the light beam into vertically polarized light, quarter wave plate (QWP1) in the reference arm to ensure the beam is linearly polarized at 45°, quarter wave plate (QWP2) in the sample arm to convert linearly polarized light into circularly polarized light, a polarizing beamsplitter to split the interferometric signal into vertical and horizontal components to be detected separately (D1 and D2).

1.5 Thesis Overview

This section provides a brief overview of the PhD thesis, summarizing the subsequent chapters and giving a brief background on each application of OCT. The initial goal of the PhD was to develop a swept-source MIR OCT using a commercial ECQCL light source. Ch 2 details the work done towards this goal, from the initial characterization of the laser source to the methods for reducing its relative intensity noise. This is a development towards building a MIR OCT with a Mach-Zehnder interferometer setup, which has a significantly improved signal-to-noise ratio compared to a Michelson interferometer. Ch 1.5.1 below discusses the potential applications of MIR OCT, including its use in non-destructive testing and spectroscopy.

Besides the development of MIR OCT, this thesis also focuses on new applications of NIR OCT, particularly in fields such as dermatology (Ch 3), dentistry (Ch 4), botany (Ch 5) and biofilm research (Ch 6). For many of the applications, OCT has been chosen as a potential imaging modality for gaining insight into the underlying biological processes due to similar reasons: non-invasiveness, portability, and a micrometre resolution that can differentiate between different types of tissue. The following sub-sections give an overview of the work that has been done using OCT in these fields.

1.5.1 Potential applications of MIR OCT

Several applications of MIR OCT have been proposed, particularly in terms of non-destructive testing and spectroscopy. Su et al. demonstrated, through Monte Carlo simulations of MIR OCT images, that MIR light could potentially be used to detect defects within ceramic samples, specifically alumina and zirconia [55]. Light in the MIR region could potentially perform better than commercial OCT systems that use NIR light (typically 1300 nm), which are optimised for biological specimens.

Unlike OCT, which collects structural images of subsurface morphology of a sample, Fourier transform infrared (FTIR) spectroscopy has been used to probe the infrared absorption spectrum or interferogram of a sample. The chemical composition of the sample determines the extent to which the light gets absorbed at a specific wavelength. For instance, MIR light is absorbed by biological specimens with high water content. FTIR spectroscopy is similar to TD-OCT, except that the sample arm is replaced with a fixed mirror and the sample is placed in between the beamsplitter and the detector. The interferometer modulates the light beam, with frequencies proportional to the wavenumber. OCT probes the sample using reflection;

FTIR spectroscopy can be used to probe the sample in various ways: transmission, reflection or attenuated total internal reflection. However, in reflection mode, the light flux is typically orders of magnitude weaker than transmission, making FTIR challenging [56].

To probe the MIR spectra of samples, early FTIR spectroscopy systems use broadband spatially incoherent light sources (Globar) much like the SLDs used in TD-OCT systems [56]. Synchrotron radiation and MIR supercontinuum radiation are two broadband light sources that were able to generate the desired spatial coherence within the MIR region [56]. The development of the QCL laser with its tuning capabilities and narrow linewidth offers the possibility of probing the MIR spectra of tissues to within specific tuning ranges. Thus, Childs et al. proposed that FTIR spectroscopy was analogous to TD-OCT and the same advantages in speed and sensitivity gained from transitioning to SS-OCT could be gained by the transition from FTIR to tunable-laser MIR spectroscopy [56]. They demonstrated that such a setup offers MIR spectra acquisition speeds improvements up to 3 orders of magnitude without a reduction in SNR.

1.5.2 OCT in dermatology

Welzel et al. were the first to attempt dermatological imaging using OCT and proposed a few applications for diagnosing skin conditions [57]. They compared OCT images with histological samples obtained through excisional biopsy, which still remains the gold standard for dermatology today. They demonstrated that OCT can distinguish between healthy skin and skin with induced subepidermal and intraepidermal blisters. OCT has been a popular imaging modality for detecting and diagnosing skin tumours such as basal cell carcinoma [58], actinic keratosis [59] and melanoma [60]. Other avenues that have been explored include using OCT

for monitoring psoriasis vulgaris [61] and wound healing [62]. Development in dermatological OCT includes developing algorithms to automatically detect features of interest such as the epidermis-dermis boundary [63] and the epidermal thickness [64], which can be used as a potential quantitative indicator for various skin conditions. Recently, the Sheffield Dermatology Research group at The University of Sheffield have been developing OCT-based biomarkers for assessing the severity of atopic dermatitis and using them to monitor new treatments for the clinical condition [65].

1.5.3 OCT in dentistry

Colston et al. were the first to image hard tissue in vitro using OCT and demonstrate the efficacy of OCT as a potential diagnostic tool for periodontal diseases [66]. They were able to resolve the enamel-cementum and gingiva-tooth junctions in porcine periodontal tissue. By designing a handheld optical probe for the OCT system, the first in vivo images of human dental tissue were obtained [67]. This intraoral OCT system had a penetration depth of 3 mm in hard tissue and 1.5 mm in soft tissue. In the same year, Feldchtein et al. conducted in vitro and in vivo studies on the potential of OCT in diagnosing periodontal diseases [68]. Their OCT system had an axial and lateral resolution of 13-17 μm and 17-22 μm respectively. It was able to distinguish between keratinized and non-keratinized mucosa, as well as caries and non-caries lesions. Use of polarization-sensitive OCT was shown to be effective in detecting early-stage caries lesions and tracking its progression [69]. OCT has since been applied to various dental applications such as assessing the quality of dental sealants [70] and detecting how orthodontic movement changes the underlying periodontal ligament [71].

1.5.4 OCT in botany

The first use of OCT in botany was a study conducted by Loeb and Barton [72], where they showed the potential of OCT in imaging fruits and lettuce. They were able to image a number of morphological features such as parenchyma cell vacuoles of a kiwifruit and the oil glands of an orange peel. Since then, OCT has been used in a variety of botanical applications. A few examples are measuring the hull thickness in lupin seeds [73], monitoring the progression of grey leaf spot disease in *Capsicum annuum* leaves [74] and quantifying the microstructural changes in *Acer serrulatum Hayata* leaves during senescence [75]. The difficulty in imaging plant cells compared to human or other animal tissue is that plant cells are surrounded by cell wall. The refractive index of plant tissue is often unknown, which makes it difficult to accurately determine distances within the sample.

1.5.5 OCT in biofilm research

Unlike other biomedical applications, OCT is not used in biofilm research primarily for deducing subsurface morphology. Instead, its ability to image in real-time and resolve the three-dimensional volume of biofilm are what makes OCT useful in understanding the mechanisms for biofilm development [76]. Xi et al. were the first to use OCT to demonstrate the growth of *Pseudomonas aeruginosa* biofilm in a capillary flow-cell and compared their results to images obtained using confocal laser scanning microscopy [77]. Besides the controlled conditions of a flow-cell, OCT is also used to analyse biofilm formation in vivo in membrane filtration systems [78]. Wagner et al. made the first attempt at quantifying biofilm, in terms of its porosity [79]. They showed that the porosity was a result of changes to biofilm growth based on flow conditions within the bioreactor. Other parameters used in the

quantification of biofilm include thickness, volume and roughness [76,80]. Biofilm thickness is the most common parameter used and varies from 30-40 μm [81] to 1.3-1.6 mm [79]. Recently, OCT has also aided in the estimation of the mechanical properties of biofilm, such as its shear modulus and Young's modulus [82].

References

[1] D. Huang, E. Swanson, C. Lin, J. Schuman, W. Stinson, W. Chang, M. Hee, T. Flotte, K. Gregory, C. Puliafito, and J. Fujimoto, "Optical coherence tomography," Science **254**(5035), 1178–1181 (1991).

[2] T. L. Szabo, "Diagnostic Ultrasound Imaging: Inside Out," 2nd ed. San Diego: Elsevier Science & Technology (2013).

[3] B. R. Masters and M. Böhnke, "Three-Dimensional Confocal Microscopy of the Living Human Eye," Annu. Rev. Biomed. Eng. **4**(1), 69–91 (2002).

[4] J.A. Izatt and M.A. Choma, "Theory of optical coherence tomography," in *Optical Coherence Tomography*, 2nd ed., W. Drexler and J. G. Fujimoto, Eds., Cham: Springer International Publishing, 47-72 (2015).

[5] P.H. Tomlins and R.K Wang, "Theory, developments and applications of optical coherence tomography," J. Appl. Phys. D: Appl. Phys. **38**(15), 2519 (2005).

[6] E. A. Swanson, D. Huang, C. P. Lin, C. A. Puliafito, M. R. Hee, and J. G. Fujimoto, "High-speed optical coherence domain reflectometry," Opt. Lett. **17**(2), 151 (1992).

[7] J. M. Schmitt, A. Knuttel, M. Yadlowsky, and M. A. Eckhaus, "Optical-coherence tomography of a dense tissue: statistics of attenuation and backscattering," Phys. Med. Biol. **39**(10), 1705–1720 (1994).

[8] B. Bouma, M. E. Brezinski, J. G. Fujimoto, G. J. Tearney, S. A. Boppart, and M. R. Hee, "High-resolution optical coherence tomographic imaging using a mode-locked Ti:Al_2O_3 laser source," Opt. Lett. **20**(13), 1486 (1995).

[9] W. Drexler, U. Morgner, F. X. Kärtner, C. Pitris, S. A. Boppart, X. D. Li, E. P. Ippen, and J. G. Fujimoto, "In vivo ultrahigh-resolution optical coherence tomography," Opt. Lett. **24**(17), 1221 (1999).

[10] C. Chudoba, J. G. Fujimoto, E. P. Ippen, H.A. Haus, U. Morgner, F. X. Kärtner, V. Scheuer, G. Angelow, and T. Tschudi, "All-solid-state Cr:forsterite laser generating 14-fs pulses at 13 µm," Opt. Lett. **26**(5), 292 (2001).

[11] P. Herz, Y. Chen, A. D. Aguirre, J. G. Fujimoto, H. Mashimo, J. M. Schmitt, A. Koski, J. Goodnow, and C. Petersen, "Ultrahigh resolution optical biopsy with endoscopic optical coherence tomography.," Opt. Express **12**(15), 3532–42 (2004).

[12] W. Drexler, U. Morgner, R. K. Ghanta, F. X. Kärtner, J. S. Schuman, and J. G. Fujimoto, "Ultrahigh-resolution ophthalmic optical coherence tomography," Nat. Med. **7**(4), 502–506 (2001).

[13] A. M. Rollins and J. A. Izatt, "Optimal interferometer designs for optical coherence tomography," Opt. Lett. **24**(21), 1484 (1999).

[14] G. L. Abbas, V. W. S. Chan, and T. K. Yee, "Local-oscillator excess-noise suppression for homodyne and heterodyne detection," Opt. Lett. **8**(8), 419 (1983).

[15] K. F. Kwong, D. Yankelevich, K. C. Chu, J. P. Heritage, and A. Dienes, “400-Hz mechanical scanning optical delay line,” Opt. Lett. **18**(7), 558 (1993).

[16] D. C. Edelstein, R. B. Romney, and M. Scheuermann, “Rapid programmable 300 ps optical delay scanner and signal-averaging system for ultrafast measurements,” Rev. Sci. Instrum. **62**(3), 579–583 (1991).

[17] J. Szydlo, N. Delachenal, R. Gianotti, R. Wälti, H. Bleuler, and R. . Salathé, “Air-turbine driven optical low-coherence reflectometry at 28.6-kHz scan repetition rate,” Opt. Commun. **154**(1–3), 1–4 (1998).

[18] Y. S. Jin, S. G. Jeon, G. J. Kim, J. I. Kim, and C. H. Shon, “Rotary Optical Delay Line for Terahertz Pulse Detection,” Conference on Lasers and Electro-Optics - Pacific Rim 2007, 1–2 (2007).

[19] A. F. Fercher, C. K. Hitzenberger, G. Kamp, and S. Y. El-Zaiat, “Measurement of intraocular distances by backscattering spectral interferometry,” Opt. Commun., **117**(1–2), 43–48 (1995).

[20] M. Choma, M. Sarunic, C. Yang, and J. Izatt, “Sensitivity advantage of swept source and Fourier domain optical coherence tomography,” Opt. Express **11**(18), 2183 (2003).

[21] J. F. de Boer, B. Cense, B. H. Park, M. C. Pierce, G. J. Tearney, and B. E. Bouma, “Improved signal-to-noise ratio in spectral-domain compared with time-domain optical coherence tomography,” Opt. Lett., **28**(21), 2067 (2003).

[22] R. Leitgeb, C. Hitzenberger, and A. Fercher, “Performance of fourier domain vs time domain optical coherence tomography,” Opt. Express **11**(8), 889 (2003).

[23] M. Wojtkowski, R. Leitgeb, A. Kowalczyk, T. Bajraszewski, and A. F. Fercher, “In vivo human retinal imaging by Fourier domain optical coherence tomography,” J. Biomed. Opt. **7**(3), 457 (2002).

[24] V. J. Srinivasan, M. Wojtkowski, A. J. Witkin, J. S. Duker, T. H. Ko, M. Carvalho, J. S. Schuman, A. Kowalczyk, and J. G. Fujimoto, “High-Definition and 3-dimensional Imaging of Macular Pathologies with High-speed Ultrahigh-Resolution Optical Coherence Tomography,” Ophthalmology **113**(11), 2054–2065 (2006).

[25] M. Wojtkowski, V. Srinivasan, J. G. Fujimoto, T. Ko, J. S. Schuman, A. Kowalczyk, and J. S. Duker, “Three-dimensional Retinal Imaging with High-Speed Ultrahigh-Resolution Optical Coherence Tomography,” Ophthalmology **112**(10), 1734–1746 (2005).

[26] B. Potsaid, I. Gorczynska, V. J. Srinivasan, Y. Chen, J. Jiang, A. Cable, and J. G. Fujimoto, “Ultrahigh speed Spectral / Fourier domain OCT ophthalmic imaging at 70,000 to 312,500 axial scans per second,” Opt. Express **16**(19), 15149 (2008).

[27] S. R. Chinn, E. A. Swanson, and J. G. Fujimoto, “Optical coherence tomography using a frequency-tunable optical source,” Opt. Lett. **22**(5), 340 (1997).

[28] B. Golubovic, B. E. Bouma, G. J. Tearney, and J. G. Fujimoto, “Optical frequency-domain reflectometry using rapid wavelength tuning of a Cr4+:forsterite laser.,” Opt. Lett. **22**(22), 1704–1706 (1997).

[29] W. Y. Oh, S. H. Yun, G. J. Tearney, and B. E. Bouma, “115 kHz tuning repetition rate ultrahigh-speed wavelength-swept semiconductor laser,” Opt. Lett. **30**(23), 3159 (2005).

[30] R. Huber, M. Wojtkowski, K. Taira, J. Fujimoto, and K. Hsu, “Amplified, frequency swept lasers for frequency domain reflectometry and OCT imaging: design and scaling principles.,” Opt. Express **13**(9), 3513–3528 (2005).

[31] R. Huber, M. Wojtkowski, and J. G. Fujimoto, “Fourier Domain Mode Locking (FDML): A new laser operating regime and applications for optical coherence tomography,” Opt. Express **14**(8), 3225 (2006).

[32] D. C. Adler, Y. Chen, R. Huber, J. Schmitt, J. Connolly, and J. G. Fujimoto, “Three-dimensional endomicroscopy using optical coherence tomography,” Nat. Photonics **1**(12), 709–716 (2007).

[33] D. C. Adler, C. Zhou, T.-H. Tsai, J. Schmitt, Q. Huang, H. Mashimo, and J. G. Fujimoto, “Three-dimensional endomicroscopy of the human colon using optical coherence tomography,” Opt. Express **17**(2), 784 (2009).

[34] R. Gray, and D. Neuhoff, “Quantization,” IEEE transactions on information theory **44**(6), 2325-2383 (1998).

[35] C. S. Colley, J. C. Hebden, D. T. Delpy, A. D. Cambrey, R. A. Brown, E. A. Zibik, W. H. Ng, L. R. Wilson, and J. W. Cockburn, “Mid-infrared optical coherence tomography,” Rev. Sci. Instrum. **78**(12), 123108 (2007).

[36] D. T. D. Childs, A. B. Krysa, K. L. Kennedy, D. G. Revin, J. W. Cockburn, R. A. Hogg, and S. J. Matcher, “A Rapid Swept-Source Mid-Infrared Laser,” International Semiconductor Laser Conference **2014**, 155–156 (2014).

[37] M.J. Weida, D. Arnone, and T. Day, “Tunable QC laser opens up mid-IR sensing applications,” Laser focus world **42**(7), S13 (2006).

[38] J. Faist, F. Capasso, D.L. Sivco, C. Sirtori, A.L. Hutchinson, and A.Y. Cho, “Quantum cascade laser,” Science **264**(5158), 553-556 (1994).

[39] A. Wittmann, Y. Bonetti, M. Fischer, J. Faist, S. Blaser, and E. Gini, “Distributed-Feedback Quantum-Cascade Lasers at 9 μm Operating in Continuous Wave Up to 423 K,” IEEE Photon. Technol. Lett., **21**(12), 814-816 (2009).

[40] G. Luo, C. Peng, H.Q. Le, S.S. Pei, H. Lee, W.Y. Hwang, B. Ishaug, and J. Zheng, “Broadly wavelength-tunable external cavity, mid-infrared quantum cascade lasers,” IEEE J. Quantum Electron., **38**(5), 486-494 (2002).

[41] A. Hugi, R. Terazzi, Y. Bonetti, A. Wittmann, M. Fischer, M. Beck, J. Faist, and E. Gini, “External cavity quantum cascade laser tunable from 7.6 to 11.4 μm,” Appl. Phys. Lett. **95**(6), 061103 (2009).

[42] J. Faist, F. Capasso, C. Sirtori, D.L. Sivco, J.N. Baillargeon, A.L. Hutchinson, S.N.G. Chu, and A.Y. Cho, “High power mid-infrared (λ~ 5 μm) quantum cascade lasers operating above room temperature,” Appl. Phys. Lett. **68**(26), 3680-3682 (1996).

[43] I. Zorin, R. Su, A. Prylepa, J. Kilgus, M. Brandstetter, and B. Heise, “Mid-infrared Fourier-domain optical coherence tomography with a pyroelectric linear array,” Opt. Express **26**(25), 33428-33439 (2018).

[44] S. Freer, D. Revin, K. Groom, and S. J. Matcher, “Towards swept-source mid-infrared OCT,” Biophotonics: Photonic Solutions for Better Health Care VI **2018**, 70 (2018).

[45] C. K. Hitzenberger and M. Pircher, "MUW Approach of PS OCT," Optical Coherence Tomography: Technology and Applications, 1103-1136 (2015).

[46] B. Baumann, "Polarization sensitive optical coherence tomography: a review of technology and applications," Appl. Sci. **7**(5), 474 (2017).

[47] M. Pircher, E. Goetzinger, R. Leitgeb, and C. K. Hitzenberger, "Three dimensional polarization sensitive OCT of human skin in vivo," Opt. Express **12**(14), 3236-3244 (2004).

[48] B. Fortune, C.F. Burgoyne, G. Cull, J. Reynaud, and L. Wang, “Onset and progression of peripapillary retinal nerve fiber layer (RNFL) retardance changes occur earlier than RNFL thickness changes in experimental glaucoma,” Investig. Ophthalmol. Vis. Sci. **54**(8), 5653-5661 (2013).

[49] J. F. De Boer, T. E. Milner, M. J. Van Gemert, and J. S. Nelson, "Two-dimensional birefringence imaging in biological tissue by polarization-sensitive optical coherence tomography," Opt. Lett. **22**(12), 934-936 (1997).

[50] C. K. Hitzenberger, E. Götzinger, M. Sticker, M. Pircher, and A. F. Fercher, "Measurement and imaging of birefringence and optic axis orientation by phase resolved polarization sensitive optical coherence tomography," Opt. Express **9**(13), 780-790 (2001).

[51] J. Zhang, S. Guo, W. Jung, J. S. Nelson, and Z. Chen, "Determination of birefringence and absolute optic axis orientation using polarization-sensitive optical coherence tomography with PM fibers," Opt. Express **11**(24) 3262-3270 (2003).

[52] S. Makita, M. Yamanari, and Y. Yasuno, "Generalized Jones matrix optical coherence tomography: performance and local birefringence imaging," Opt. Express **18**(2), 854-876 (2010).

[53] E. Götzinger, M. Pircher, and C. K. Hitzenberger, "High speed spectral domain polarization sensitive optical coherence tomography of the human retina," Opt. Express **13**(25), 10217-10229 (2005).

[54] M. Yamanari, S. Makita, V. D. Madjarova, T. Yatagai, and Y. Yasuno, "Fiber-based polarization-sensitive Fourier domain optical coherence tomography using B-scan-oriented polarization modulation method," Opt. Express **14**(14), 6502-6515 (2006).

[55] R. Su, M. Kirillin, E. W. Chang, E. Sergeeva, S. H. Yun, and L. Mattsson, “Perspectives of mid-infrared optical coherence tomography for inspection and micrometrology of industrial ceramics,” Opt. Express **22**(13), 15804 (2014).

[56] D. T. D. Childs, R. A. Hogg, D. G. Revin, I. U. Rehman, J. W. Cockburn, and S. J. Matcher, “Sensitivity Advantage of QCL Tunable-Laser Mid-Infrared Spectroscopy Over FTIR Spectroscopy,” Appl. Spectrosc. Rev. **50**(10), 822–839 (2015).

[57] J. Welzel, E. Lankenau, R. Birngruber, and R. Engelhardt, “Optical coherence tomography of the human skin,” J. Am. Acad. Dermatol. **37**(6), 958-963 (1997).

[58] J.M. Olmedo, K.E. Warschaw, J.M. Schmitt, and D.L. Swanson, “Optical coherence tomography for the characterization of basal cell carcinoma in vivo: a pilot study,” J. Am. Acad. Dermatol. **55**(3), 408-412 (2006).

[59] M.A. Boone, S. Norrenberg, G.B. Jemec, and V. Del Marmol, “Imaging actinic keratosis by high-definition optical coherence tomography. Histomorphologic correlation: a pilot study,” Exp. Dermatol. **22**(2), 93-97 (2013).

[60] T. Gambichler, P. Regeniter, F.G. Bechara, A. Orlikov, R. Vasa, G. Moussa, M. Stücker, P. Altmeyer, and K. Hoffmann, “Characterization of benign and malignant melanocytic skin lesions using optical coherence tomography in vivo,” J. Am. Acad. Dermatol. **57**(4), 629-637 (2007).

[61] H. Morsy, S. Kamp, L. Thrane, N. Behrendt, B. Saunder, H. Zayan, E. Abd Elmagid, and G.B. Jemec, “Optical coherence tomography imaging of psoriasis vulgaris: correlation with histology and disease severity,” Arch. Dermatol. Res. **302**(2), 105-111 (2010).

[62] M.J. Cobb, Y. Chen, R.A. Underwood, M.L. Usui, J. Olerud, and X. Li, “Noninvasive assessment of cutaneous wound healing using ultrahigh-resolution optical coherence tomography,” J. Biomed. Opt. **11**(6), 064002 (2006).

[63] M.R. Avanaki, and A. Hojjatoleslami, “Skin layer detection of optical coherence tomography images,” Optik **124**(22), 5665-5668 (2013).

[64] J. Weissman, T. Hancewicz, and P. Kaplan, “Optical coherence tomography of skin for measurement of epidermal thickness by shapelet-based image analysis,” Opt. Express **12**(23), 5760-5769 (2004).

[65] R.A. Byers, R. Maiti, S.G. Danby, E.J. Pang, B. Mitchell, M.J. Carré, R. Lewis, M.J. Cork, and S.J. Matcher, "Sub-clinical assessment of atopic dermatitis severity using angiographic optical coherence tomography," Biomed. Opt. Express **9**, 2001-2017 (2018).

[66] B.W. Colston, M.J. Everett, L.B. Da Silva, L.L. Otis, P. Stroeve, and H. Nathel, “Imaging of hard- and soft-tissue structure in the oral cavity by optical coherence tomography,” Appl. Opt. **37**(16), 3582-3585 (1998).

[67] B.W. Colston, U.S. Sathyam, L.B. DaSilva, M.J. Everett, P. Stroeve, and L.L. Otis, “Dental OCT,” Opt. Express **3**(6), 230-238 (1998).

[68] F.I. Feldchtein, G.V. Gelikonov, V.M. Gelikonov, R.R. Iksanov, R.V. Kuranov, A.M. Se7geev, N.D. Gladkova, M.N. Ourutina, J.A. Warren, and D.H. Reitze, “In vivo OCT imaging of hard and soft tissue of the oral cavity,” Opt. Express **3**(6), 239-250 (1998).

[69] D. Fried, J. Xie, S. Shafi, J.D. Featherstone, T. Breunig, and C.Q. Le, “Imaging caries lesions and lesion progression with polarization sensitive optical coherence tomography,” J. Biomed. Opt. **7**(4), 618-627 (2002).

[70] A.K. Braz, C.M. Aguiar, and A.S. Gomes, “Evaluation of the integrity of dental sealants by optical coherence tomography,” Dent. Mater. **27**(4), e60-e64 (2011).

[71] J.H. Baek, J. Na, B.H. Lee, E. Choi, and W.S. Son, “Optical approach to the periodontal ligament under orthodontic tooth movement: a preliminary study with optical coherence tomography,” Am. J. Orthod. Dentofacial Orthop. **135**(2), 252-259 (2009).

[72] G. Loeb, and J.K. Barton, “Imaging botanical subjects with optical coherence tomography: a feasibility study,” Transactions of the ASAE, **46**(6), 1751 (2003).

[73] J.C. Clements, A.V. Zvyagin, K.K.M.B.D. Silva, T. Wanner, D.D. Sampson, and W.A. Cowling, “Optical coherence tomography as a novel tool for non-destructive measurement of the hull thickness of lupin seeds,” Plant Breed. **123**(3), 266-270 (2004).

[74] N.K. Ravichandran, R.E. Wijesinghe, M.F. Shirazi, K. Park, S.Y. Lee, H.Y. Jung, M. Jeon, and J. Kim, “In vivo monitoring on growth and spread of gray leaf spot disease in capsicum annuum leaf using spectral domain optical coherence tomography,” J. Spectrosc. 2016 (2016).

[75] T. Anna, S. Chakraborty, C.Y. Cheng, V. Srivastava, A. Chiou, and W.C. Kuo, “Elucidation of microstructural changes in leaves during senescence using spectral domain optical coherence tomography,” Sci. Rep. **9**(1), 1-10 (2019).

[76] M. Wagner, and H. Horn, “Optical coherence tomography in biofilm research: a comprehensive review,” Biotechnol. Bioeng. **114**(7), 1386-1402 (2017).

[77] C. Xi, D.L. Marks, S. Schlachter, W. Luo, and S.A. Boppart, “High-resolution three-dimensional imaging of biofilm development using optical coherence tomography,” J. Biomed. Opt. **11**(3), 034001 (2006).

[78] S. West, M. Wagner, C. Engelke, and H. Horn, “Optical coherence tomography for the in situ three-dimensional visualization and quantification of feed spacer channel fouling in reverse osmosis membrane modules,” J. Membr. Sci. **498**, 345-352 (2016).

[79] M. Wagner, D. Taherzadeh, C. Haisch, and H. Horn, “Investigation of the mesoscale structure and volumetric features of biofilms using optical coherence tomography,” Biotechnol. Bioeng. **107**(5), 844-853 (2010).

[80] R. Murga, P.S. Stewart, and D. Daly, “Quantitative analysis of biofilm thickness variability,” Biotechnol. Bioeng. **45**(6), 503-510 (1995).

[81] Y. Shen, C. Huang, G.L. Monroy, D. Janjaroen, N. Derlon, J. Lin, R. Espinosa-Marzal, E. Morgenroth, S.A. Boppart, N.J. Ashbolt, and W.T. Liu, “Response of simulated drinking water biofilm mechanical and structural properties to long-term disinfectant exposure,” Environ. Sci. Technol. **50**(4), 1779-1787 (2016).

[82] F. Blauert, H. Horn, and M. Wagner, “Time-resolved biofilm deformation measurements using optical coherence tomography,” Biotechnol. Bioeng. **112**(9), 1893-1905 (2015).

Chapter 2: Development of Mid-Infrared OCT

The following chapter is mainly based on material previously published in [1]. The paper characterizes the various sources of noise in an in-house mid-infrared swept-source OCT system, and demonstrates various methods of reducing the laser relative intensity noise. This is a follow-up on work done previously in [2], where the individual components of the MIR-OCT system, such as the laser source, the detector and analogue-to-digital convertor, were investigated. Figures from this work [2] have also been incorporated into the chapter.

Methods for reducing relative intensity noise in swept-source mid-infrared OCT

Wai Ching Lin[a], Dmitry G. Revin[a], Stephen J. Matcher[a]

[a] Dept. of Electronic & Electrical Engineering, The University of Sheffield, S1 3JD, UK

Abstract

Mid-infrared optical coherence tomography (MIR OCT) has shown promise in the last few years in applications such as spectroscopy and non-destructive testing. Previously, we have successfully demonstrated a MIR swept-source OCT and measured its noise from three main sources: quantization noise from the ADC, shot noise from the detectors and relative intensity noise (RIN) of the laser. Of these sources, RIN places an upper limit on the SNR of swept-source OCT systems. We attempt to characterize RIN in greater depth and determine whether it can be reduced through normalization. The pulsed laser used (Block Engineering Lasertune) is tunable within the wavelength range of 5.4-12.8 µm. The laser output was held at a fixed wavelength, repetition rate and pulse width. Each laser pulse was integrated to find its average power along the pulse duration. A Fourier transform of the result was used to calculate the ratio of the AC power to DC power, giving a value for RIN. By using a beamsplitter and aspheric lenses to carefully focus the beam onto two detectors (Vigo System's PVMI-4TE), the two pulse trains can be normalized. Through normalization, RIN was reduced from -74dB/Hz to -92dB/Hz. Increasing the repetition rate and pulse width leads to a decrease in RIN, but an upper limit on the laser duty cycle constrains improvements to RIN via this

method. As the swept laser has four integrated quantum cascade laser (QCL) chips, we also examine the effect of different emission wavelengths on RIN.

2.1 Introduction

Mid-infrared optical coherence tomography (MIR OCT) has potential as a spectroscopic tool to non-invasively study biological tissue [3,4]. It has already shown promise in areas such as non-destructive testing [5]. By looking at the mid-infrared absorption spectrum, biological properties of tissue could be determined for pathological conditions such as eczema. It is theorized that MIR spectroscopy could potentially provide a sensitivity and speed advantage to the current method of FTIR spectroscopy in a similar way to how Fourier-domain OCT has a higher sensitivity and faster acquisition speeds compared to time-domain OCT [3]. The development of MIR OCT systems has followed the same trajectory, with early MIR OCT systems using the time-domain setup [6] and later systems using spectral-domain configurations [5,7].

Previously, we have demonstrated a swept-source MIR OCT using a home-built external cavity system with a commercial quantum cascade laser (QCL) [8,2]. This system had a signal-to-noise ratio (SNR) of around 17 dB. Reducing the sources of noise in an OCT system improves the SNR. Relative intensity noise (RIN) from the laser is the predominant noise source and places an upper limit on the SNR. RIN is a measure of fluctuations in laser intensity in excess of shot noise. The other noise sources, mainly quantization noise from an ADC and receiver noise from a detector, are inherent to the detection system.

In this paper, we aim to quantify RIN and develop ways to reduce this noise source in order to improve the resultant SNR of the interferogram and the sensitivity of our OCT system. By

using a hot soldering iron tip as a constant source of mid-infrared radiation, the lowest detectable limit for this setup can be calculated. Using two detectors instead of one allows for the pulse-to-pulse normalization of the data. We investigate whether normalization has an effect on RIN and if it can be used as a method to reduce RIN. Another way of changing RIN would be to vary the repetition rate and pulse width of the laser. We investigate how effective and feasible such a method is in reducing RIN. Last, we see how different emission wavelengths of the laser can affect RIN.

2.2 Method

2.2.1 About the QCL source

2.2.1.1 Laser tuning curve

The laser used is the Block Engineering LaserTune, with a tunable 5.4 – 12.8 µm wavelength range (1863-763 cm^{-1}). The QCL has 4 internal laser modules and a maximum allowable duty cycle of 8%. In the default settings, the laser is pulsed at a repetition rate of 1 MHz with a 50 ns pulse duration and 5% duty cycle.

A broadband power meter (13PEM001, Melles Griot Inc.) with spectral range of 200 nm to 20 µm was used to measure the average power output of a MIR QCL over its entire tuning range in incremental steps of 10 cm^{-1} (Fig. 2.1). Using a 5% duty cycle, the laser has an average power output of 0.5mW – 5mW, with a peak in average power of 5mW occurring at 880cm^{-1}. Pulses of 1MHz repetition rate and 50ns duration and 0.5MHz repetition rate and 100ns duration have the same duty cycle and therefore show similar power outputs. Halving the duty cycle, either by decreasing the pulse repetition rate or pulse duration, halves the average

power output. The laser has 4 QCL modules and the boundary between 2 modules can be clearly seen as regions of low power output, for example at 1620cm^{-1} and 1350cm^{-1}.

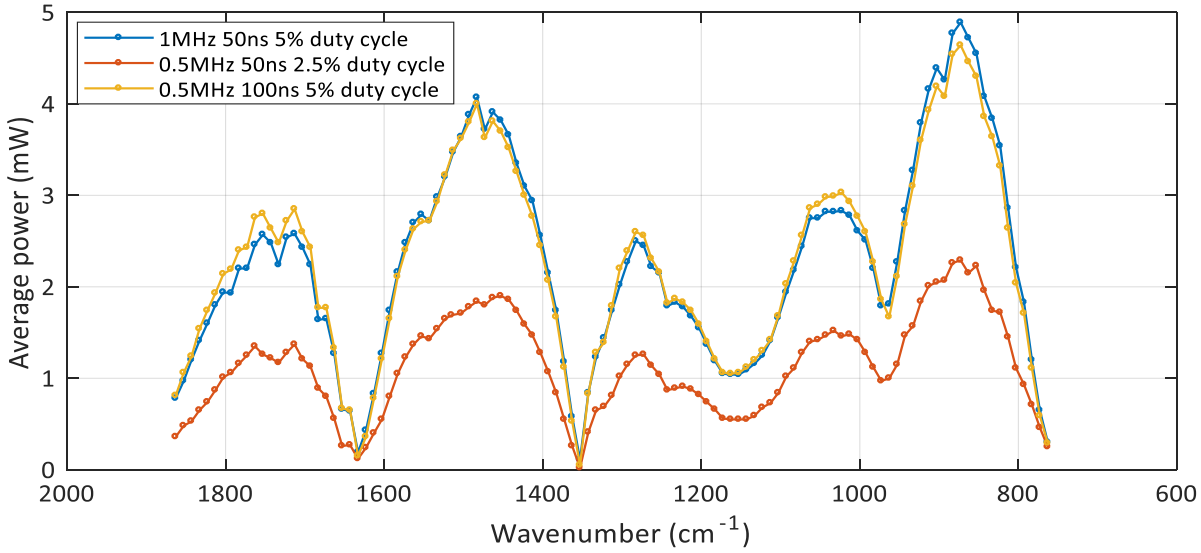

Fig. 2.1. Average power output of the tunable QCL laser light source at various wavelengths. The QCL has 4 laser modules and this can be clearly seen as a low power output at the boundary between two modules (e.g. at 1620cm^{-1} and 1350cm^{-1}). Decreasing the duty cycle, either by decreasing the pulse repetition rate or pulse duration, decreases the average power output proportionately.

2.2.1.2 Pulse profile

Fig. 2.2 shows the shape of a typical 500ns laser pulse. This is the longest pulse width possible for the laser and the pulse repetition rate had to be lowered to 5 kHz to stay within the duty cycle limits. The beam intensity fluctuates over the entire duration of the pulse, possibly due to the bandwidth of the photodiode, mode hopping, etc.

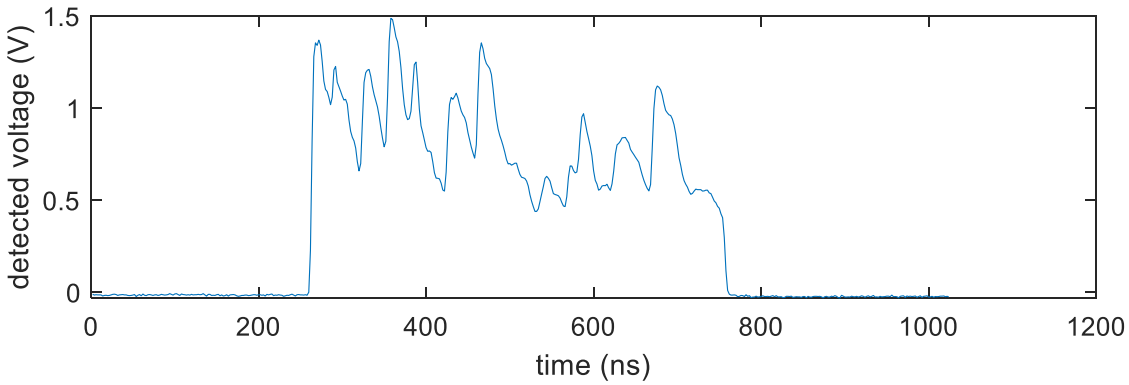

Fig. 2.2. 500ns pulse shape for the swept laser. The laser was operating at a pulse repetition rate of 5 kHz. The pulse intensity fluctuates over the entire duration.

2.2.1.3 *k*-space linearization

When the laser is swept across a wavelength range, the wavelength does not change linearly with time. This is due to a variety of reasons such as phase noise in the laser or vibrations in the galvo mirror used for sweeping. Resampling of the time series raw data is necessary to ensure the data is linear with respect to wavenumber *k*. The depth-resolved reflectivity profile can then be attained by computing the Fourier transform of the resampled data.

To resample the raw data, we need to know specifically how the wavenumber changes when the laser is swept. To do this, we utilize the fact that the manufacturer has allowed for the QCL to be operated in two modes. In “step” mode, the laser can be set to pulse at a single wavelength for a duration of time. In “sweep” mode, the laser is swept (non-)linearly over a set wavelength range for a duration of time.

Firstly, using “step” mode, the laser is pulsed at 1 cm^{-1} intervals from 1250 to 1350 cm^{-1} for 10ms each – 100 intervals in total for a total duration of 1s. The intensity over time is recorded using a broadband power meter. Secondly, in “sweep” mode, the laser is swept over the same wavelength range for a 1s duration and the intensity is also recorded using the same power meter. Power readings from the “step” mode measurement can be matched to the

corresponding power readings from the “sweep” mode measurement. Since wavelengths in the “step” profile are set by the user and therefore known, we can use both measurements to determine the wavelength at each time point in the “sweep” profile. Fig. 2.3 shows the graph of wavenumber against time. A simple linear regression is used to resample the raw data.

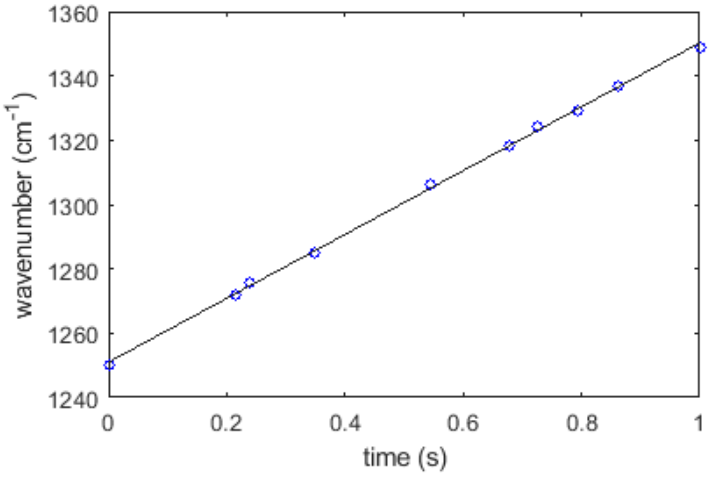

Fig. 2.3. Wavelength over time for a 1s sweep duration with a 1250 cm^{-1} to 1350 cm^{-1} wavelength range.

2.2.2 Swept-source OCT using Michelson interferometer

Previously [2], we assembled a swept-source OCT system using the Block Engineering Lasertune, a mid-infrared swept laser. The laser emits vertically polarized light in pulses at repetition rates of 1 kHz – 1 MHz, with pulse durations of 20-500ns. The emission wavelength of the laser can be varied between 5.4-12.8 µm. Fig. 2.4 shows a schematic diagram of the swept-source system. OCT systems make use of the Michelson interferometer, where the light beam is split into two similar-intensity reference and sample beams using a calcium fluoride based 50:50 beamsplitter. The reference beam is reflected off a fixed flat mirror. The

sample beam is directed onto a sample with layers of differing refractive indices. When the incident beam meets a refractive index discontinuity, some light is back-reflected. This backscattered light interferes with the beam returning from the reference mirror. While the laser operating wavelength is being swept across a required wavelength range, the resultant interferometric signal is captured by a detector. The detector used is a thermoelectrically cooled HgCdTe detector with a detectable area of 1x1mm (PVMI-4TE, VIGO System S.A., Poland). An analogue-to-digital convertor (ADC), is used to record the interferogram. The ADC (ATS9350, Alazar Technologies Inc, Canada) has a maximum sampling rate of 500 MS/s.

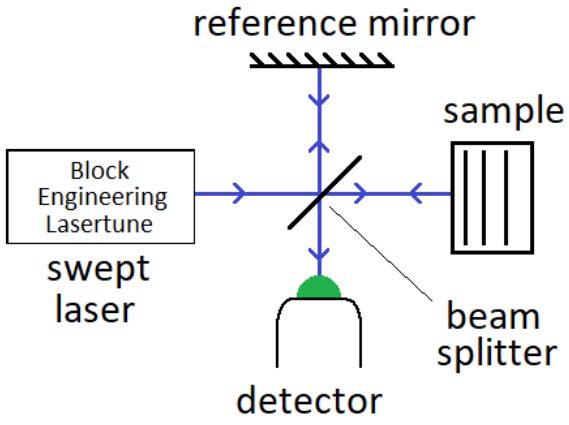

Fig. 2.4. Setup of the swept-source OCT system. Light from the laser is split using a beamsplitter. The beam is reflected off a mirror in the reference arm. In the sample arm, some light is backscattered when it reaches a refractive index discontinuity. The interferometric signal is recorded by a detector.

2.2.3 Characterization of ADC and detector noise

An OCT system has three main noise sources: the analogue-to-digital converter (ADC), the photodetectors and the relative intensity noise (RIN). The total noise in the system is found by adding the three noise sources in quadrature.

The ADC and detector noise are characterised by their noise spectral density and are independent of the laser intensity. The AlazarTech ATS9350 12-bit ADC was used to measure the voltage output of the photodetector. The ADC was controlled using LabVIEW (National

Instruments, 2015) and the noise spectral density calculated using MATLAB (MathWorks, 2015b). A 500 MS/s acquisition rate, 12-bit digitisation and a voltage range of ±40 mV was used. 2^{17} data points were collected, giving a frequency resolution of 3.8 kHz. The power spectral density was calculated by taking the squared modulus of the Fourier Transform of the data, as shown by Eq. 2.1.

$$P[f] = \frac{\Delta t}{N}\left|\sum_{n=0}^{N-1} x[n] \cdot e^{-i2\pi f n}\right|^2 \quad , \frac{-1}{2\Delta t} < f < \frac{1}{2\Delta t} \tag{2.1}$$

Δt is the sampling interval, *N* is the number of data points, *f* is the frequency and *x* is the value of the data point at $t = n \cdot \Delta t$. The noise spectral density is calculated as the square root of the mean of the power spectral density, over the detector bandwidth of 100 MHz. The noise density of the detector is compared against the expected value given in the manufacturer's data sheet. The noise spectral density of the ADC is also measured.

2.2.4 Relative intensity noise

To measure RIN, the sample arm of the setup in Fig. 2.4 is closed to prevent two-beam interference. A minimum of 2000 pulses is recorded for each RIN measurement. An ADC sampling rate of 500MS/s is used to capture the details of each pulse. The recorded pulses are processed using MATLAB. Fig. 2.5 illustrates how the data is handled. Fig. 2.5A shows the typical time series data of a laser pulse train. While 2000 consecutive pulses are recorded, the data here has been truncated to show the individual pulses in good resolution. A repetition rate of 1 MHz and pulse width of 50ns were used here. The graph clearly demonstrates that pulse shape and intensity fluctuate during the pulses and from pulse to pulse. Each pulse is averaged over its duration to give a single data point. The resultant averaged pulse train data is shown in Fig. 2.5B. A single data point on this graph represents the averaged value of a

single pulse. The data in this graph has once again been truncated to show the fluctuations between pulses. A Fourier transform of the pulse train allows the power spectrum to be calculated (Fig. 2.5C). RIN is calculated by finding the ratio of the AC to DC power, divided by the frequency interval. This AC power is calculated by finding the mean of the noise floor, whereas the value of the power spectrum at 0 Hz is the DC power. The error is taken to be the standard deviation of the noise floor, which results in an error in the RIN computed of ±0.5dB/Hz.

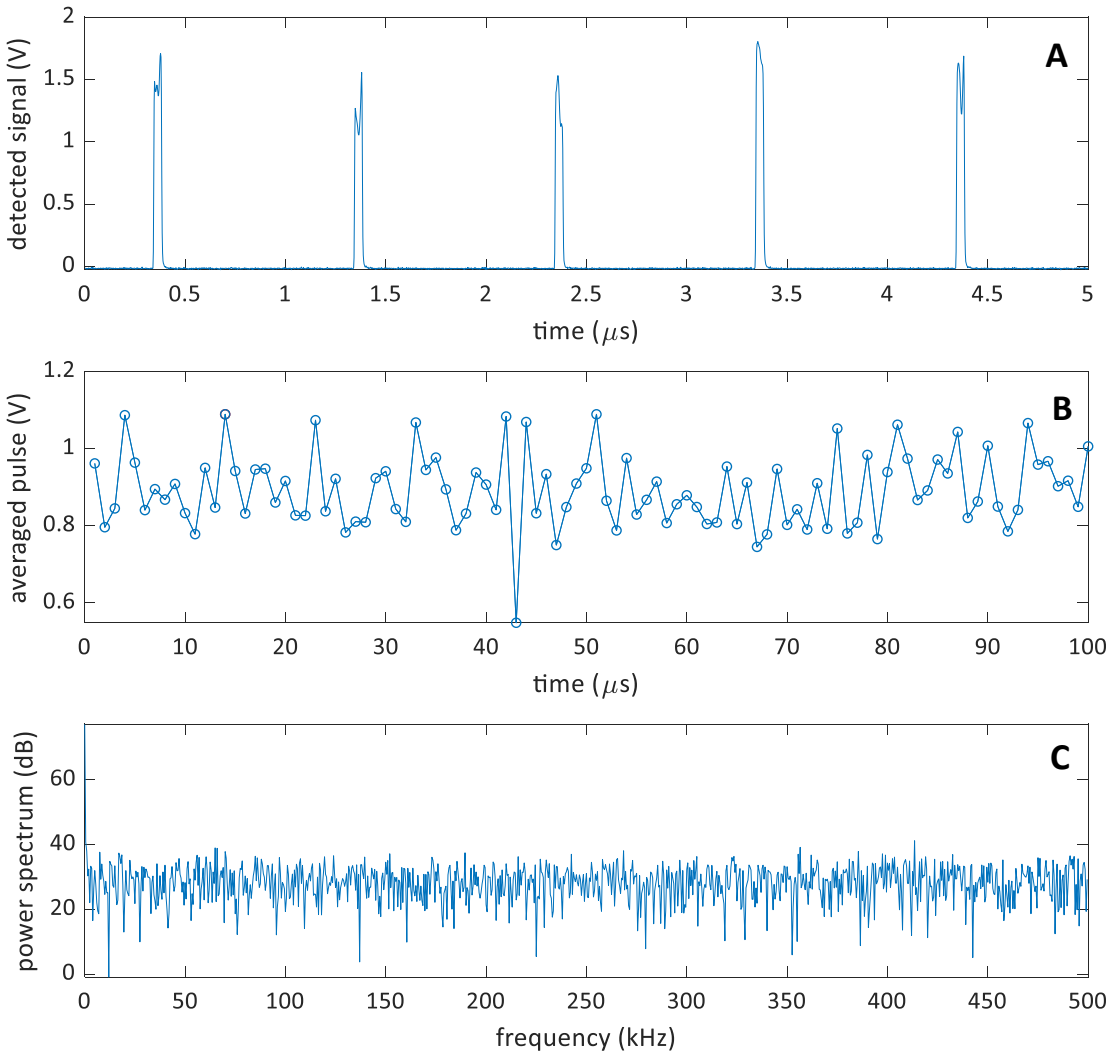

Fig. 2.5. Graphs showing how RIN is calculated. (A) Time series data of the laser pulse train. (B) Each pulse is averaged over its duration to give a single data point per pulse. (C) A Fourier transform of (B) gives the power spectrum. The ratio of the AC to DC power is the RIN + detector noise + ADC noise. Given the high laser power, the RIN is assumed to be the dominant term.

To investigate the effect of intensity normalization on RIN, the interferometer setup above is reconfigured into the following (Fig. 2.6). The laser beam still passes through the beamsplitter, but the two beams are immediately measured by two matched detectors, DetA and DetB. Normalization was achieved by dividing the averaged pulses from DetA by the averaged pulses from DetB. Nickel-coated ZnSe neutral density filters (NDIR03B and NDIR10B, Thorlabs Inc., USA) are used to reduce laser power to avoid saturating the detectors. Chalcogenide aspheric lenses (390028-F, Thorlabs Inc., USA) in front of the detectors, with a 5.95mm focusing length and 8.0mm diameter, were investigated as a way to reduce the noise introduced by an uncontrolled steering of the laser beam, by ensuring that the full beam profile remains on the detector active area, even if the beam steers slightly.

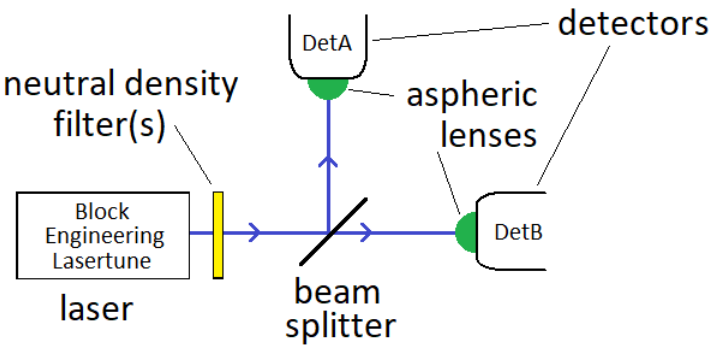

Fig. 2.6. Setup with two matched detectors for RIN measurements. A 50:50 beamsplitter was used to split the laser beam into two equal intensity beams. Neutral density filters were used to reduce the power of the laser. Aspheric lenses help to reduce the noise introduced by the beam steering.

2.3 Results

2.3.1 Initial interference fringes using Michelson interferometer

A swept-source OCT system was built using the setup shown in Ch 2.2.2. As this is an initial measurement of the interference fringes, no other optical components, such as focusing lenses to account for beam divergence, were incorporated into the setup. A zero dB reflector was used as the sample, the reference mirror was positioned at 1.5 mm from the zero OPD position and the interferogram was recorded. Fig. 2.7 and Fig. 2.8 show graphs of the light intensity detected over time for a 1s and 200ms sweep duration respectively, interference as the laser is swept over a tuning range of 8.00–7.41 µm. While the 200ms sweep has less noise compared to the 1s sweep, changing the sweep duration does not seem to have an effect on the depth modulation. This is as expected. As explained in Ch 1.1, the depth modulation depends on the OPD and the FWHM bandwidth of the laser source. The laser and the OPD have not been altered when changing the sweep duration and thus, the depth modulation is not expected to change.

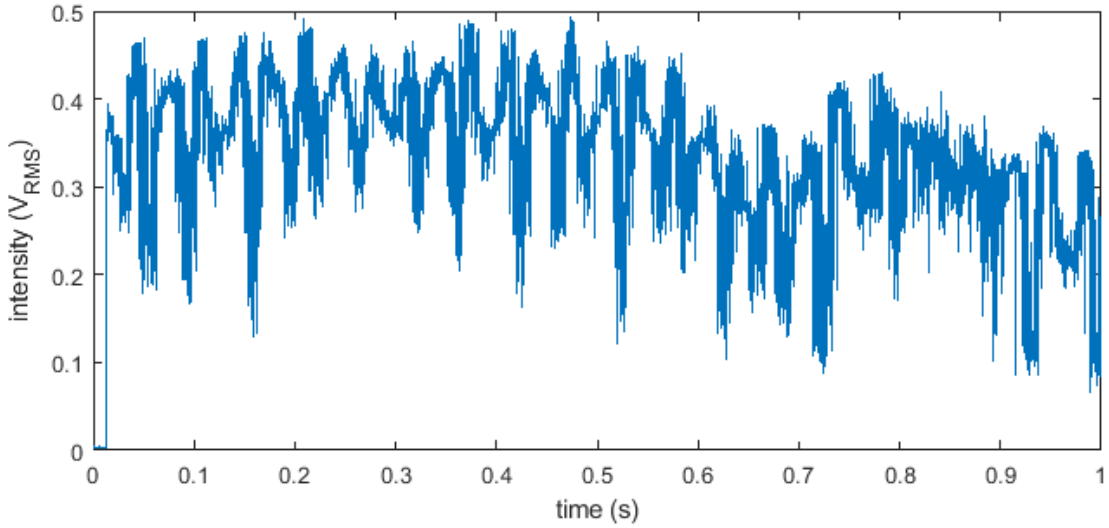

Fig. 2.7. Graph of light intensity detected over time for a 1s sweep duration.

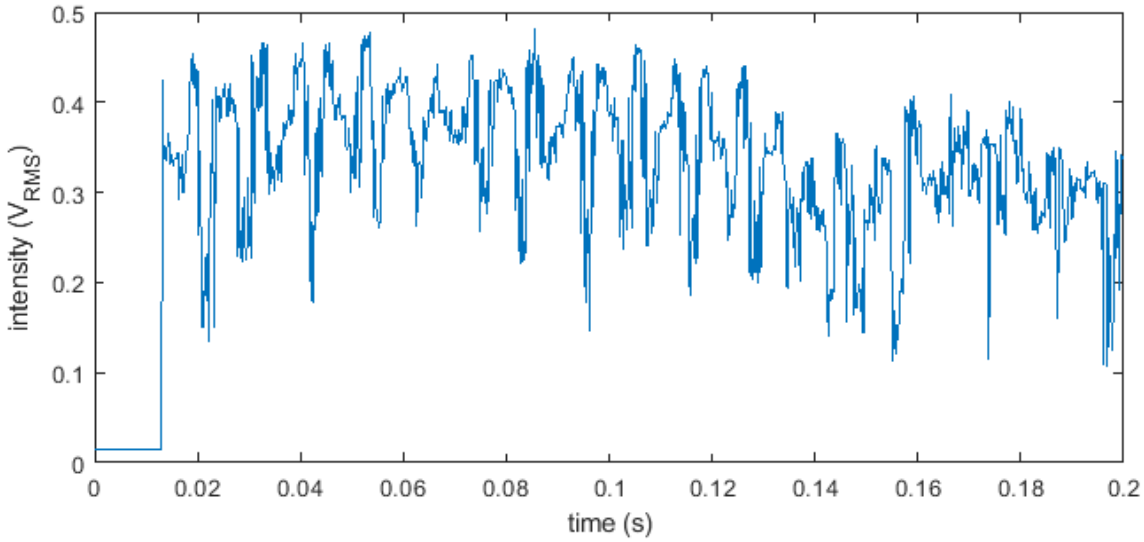

Fig. 2.8 Graph of light intensity detected over time for a 200ms sweep duration.

The depth-resolved reflectivity profile for Fig. 2.7 and 2.8 are obtained by first resampling the raw data and then calculating its Fourier transform. Fig. 2.9 shows the reflectivity profile for a 1s sweep and Fig. 2.10 shows the reflectivity profile for the 200ms sweep. Both show a peak at an axial depth of 1.5mm, which matches the position of the sample at 1.5mm from the zero OPD position. The secondary peaks present at 2.5mm, 8.5mm and 11.5mm are possibly due to the laser itself, giving rise to a modulated laser spectrum and producing secondary lobes in the Fourier transform.

The SNR is calculated as the difference between the peak amplitude (i.e., at 1.5mm axial depth) and the noise floor. In Fig. 2.9, there is a peak at an axial depth of 1.5 mm with an amplitude of 20.5dB, and a high-frequency noise floor of 3dB, which gives an SNR of 17.5dB. The plot in Fig. 2.9 has been truncated to highlight the peaks present near 0mm axial depth. The noise floor is calculated as the mean of the spectrum from 15mm onwards. (N.B. all dB figures have a common, arbitrary offset.) Similarly, the SNR for the 200ms sweep (Fig. 2.10) is 13.9dB. The reflectivity profile for the 1s sweep (Fig. 2.9) has a 4dB higher noise floor compared the 200ms sweep (Fig. 2.10), which correlates with observations of Fig. 2.7 and 2.8.

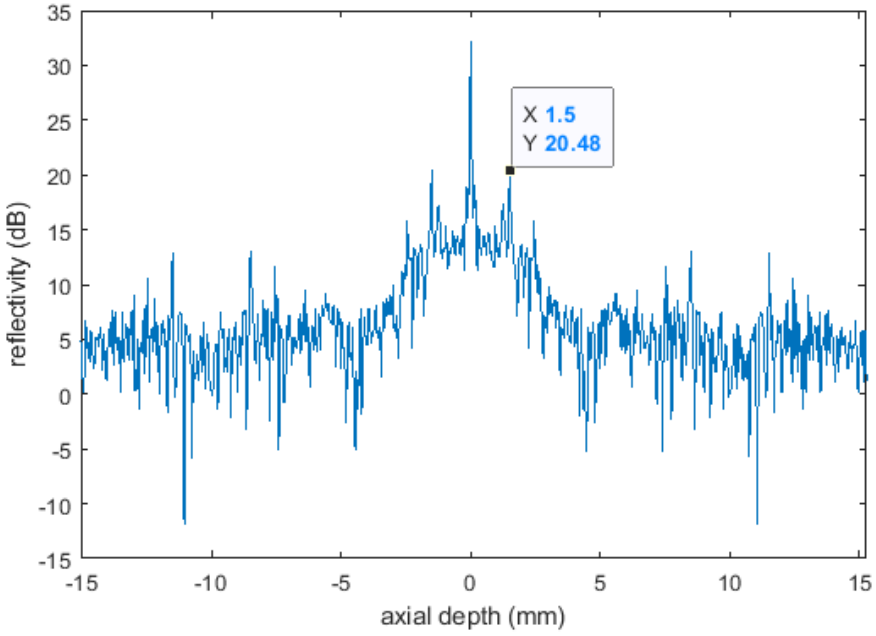

Fig. 2.9. Reflectivity profile for a 1s sweep, calculated by resampling the raw data shown in Fig. 2.7 and performing a Fourier transform. The SNR is 17.5dB.

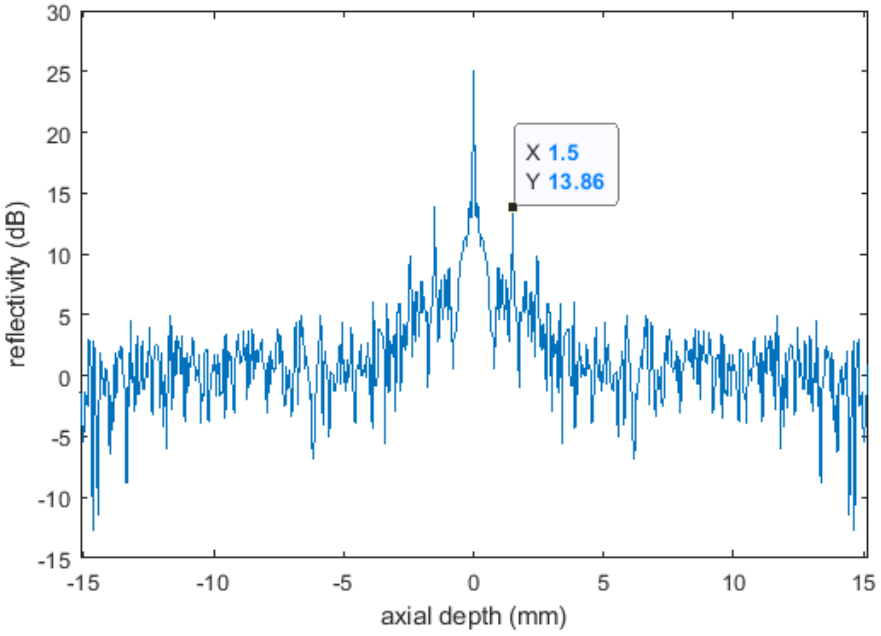

Fig. 2.10. Reflectivity profile for a 200ms sweep, calculated using the raw data shown in Fig. 2.8. The SNR is 13.9dB.

2.3.2 Characterization of ADC and detector noise

The power spectral density of both the ADC and detector, over a measurement bandwidth of 250 MHz, is shown in Fig. 2.11. The ADC noise density is constant at 2.8 pW/√Hz, over a 100 MHz bandwidth. The noise density of the detector is 21.4 pW/√Hz for a 100 MHz bandwidth. At the high cut-off frequency of 100 MHz, the power spectral density begins to decrease to ADC noise levels. The calculated noise density of the detector is slightly lower than the manufacturer's specifications (29.3 pW/√Hz), perhaps due to the manufacturer using an unspecified ADC acquisition rate and bandwidth.

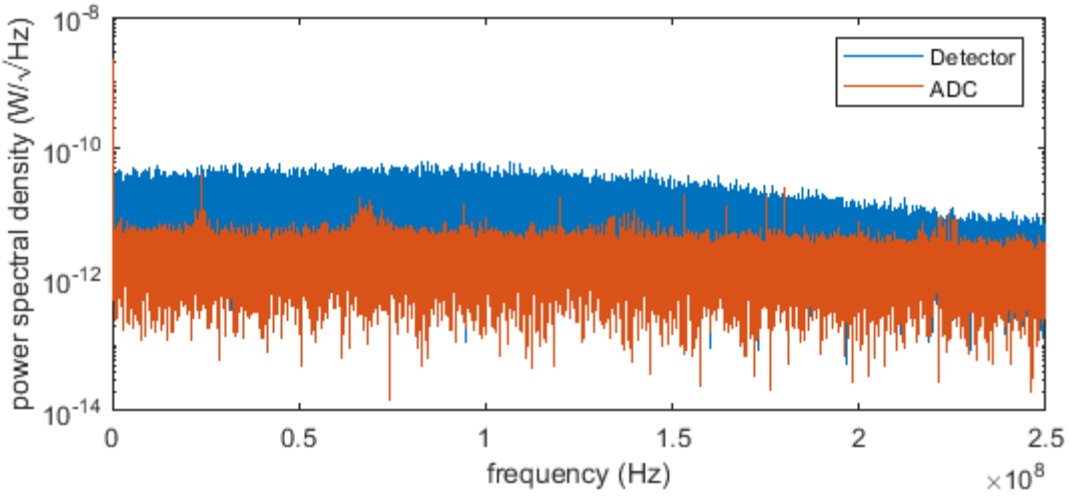

Fig. 2.11. Power spectral density over a 250 MHz bandwidth, for the ADC and detector. The noise density over 100 MHz is 2.8 pW/√Hz and 21.4 pW/√Hz for the ADC and detector respectively.

2.3.3 Lowest detectable limit of RIN

The hot tip of a soldering iron providing continuous mid-infrared radiation is chosen to simulate a low noise continuous wave spatially and temporally incoherent light source and estimate the lowest level of the noise detectable by the current system. The ADC is a 12-bit system that allows the use of different input voltage ranges. The data was collected and processed using the same method as other RIN calculations. Details of the method can be found above in section 2.2.4. Even though there were no pulses present in the data, the same time intervals were used for calibration.

Table 2.1 shows the effect of various dynamic ranges on the calculated RIN of such a modelled source. The error in RIN calculation, as mentioned in section 2.2.4 above, is ±0.5dB/Hz. The lowest input range of this ADC is ±0.4V and it results in a RIN of -133 dB/Hz. The largest dynamic range in this ADC is ±2V, which results in a RIN of -123 dB/Hz. The use of higher dynamic range leads to the reduction of the RIN values. Since the RIN of the swept pulsed laser would be measured using the dynamic range of ±2V, the lowest RIN that can be

measured in subsequent experiments is -123 dB/Hz. This shows that the “RIN” measured is actually composed of the true RIN plus the detector and ADC noise.

Table 2.1. The effect of ADC dynamic range on RIN. The smallest dynamic range of this ADC is ±0.4V and this results in a RIN of -133 dB/Hz. The largest dynamic range in this ADC is ±2V, which results in a RIN of -123 dB/Hz. Increasing the dynamic range reduces the value of RIN that can be measured using this detection system.

ADC dynamic range (V)	**RIN (±0.5 dB/Hz)**
±0.4	-133
±1	-125
±2	-123

2.3.4 The effect of normalization on RIN

Each detector was digitised in a separate channel of the ADC and then normalized in post-processing. Normalization was achieved by dividing the averaged pulses of DetA by the averaged pulses of DetB. Analogue electronics such as differential amplifiers could have been used to normalize the detected signals. However, they introduce another source of noise into the system, which would be undesirable when our objective is noise characterisation.

Fig. 2.12 shows the effect of normalization on the averaged pulse train. The figure clearly shows a reduction in noise with normalization. RIN was -74 dB/Hz before normalization and -92 dB/Hz after normalization, which is an improvement of -18 dB/Hz.

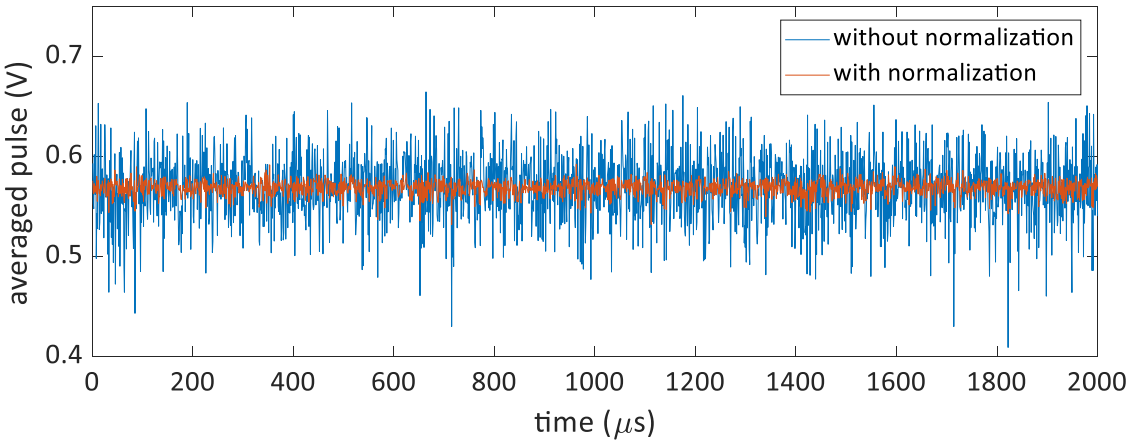

Fig. 2.12. Laser pulses averaged over their duration, with and without normalization. Normalization was achieved by dividing the averaged pulses of DetA by the averaged pulses of DetB. RIN is -74 dB/Hz before normalization and -92 dB/Hz after normalization. Parameters used: 1 MHz repetition rate, 50ns pulse duration, wavelength fixed at 1300 cm-1, 2000 pulses recorded at 500MS/s sampling rate, ±2V dynamic range.

Fig. 2.13 shows the time series data of the averaged pulses for both detector channels without (top) and with (bottom) the use of aspheric lenses. Without aspheric lenses, the averaged pulses in DetA and DetB do not have good correlation. When this set of data is normalized, there was no reduction in RIN; RIN remained around -75 dB/Hz. With the lenses, there is visible correlation between the averaged pulses captured by the two detector channels. When this data is normalized, the calculated RIN is - 92dB/Hz. This suggests that the shape and/or position of the beam spot fluctuates over time.

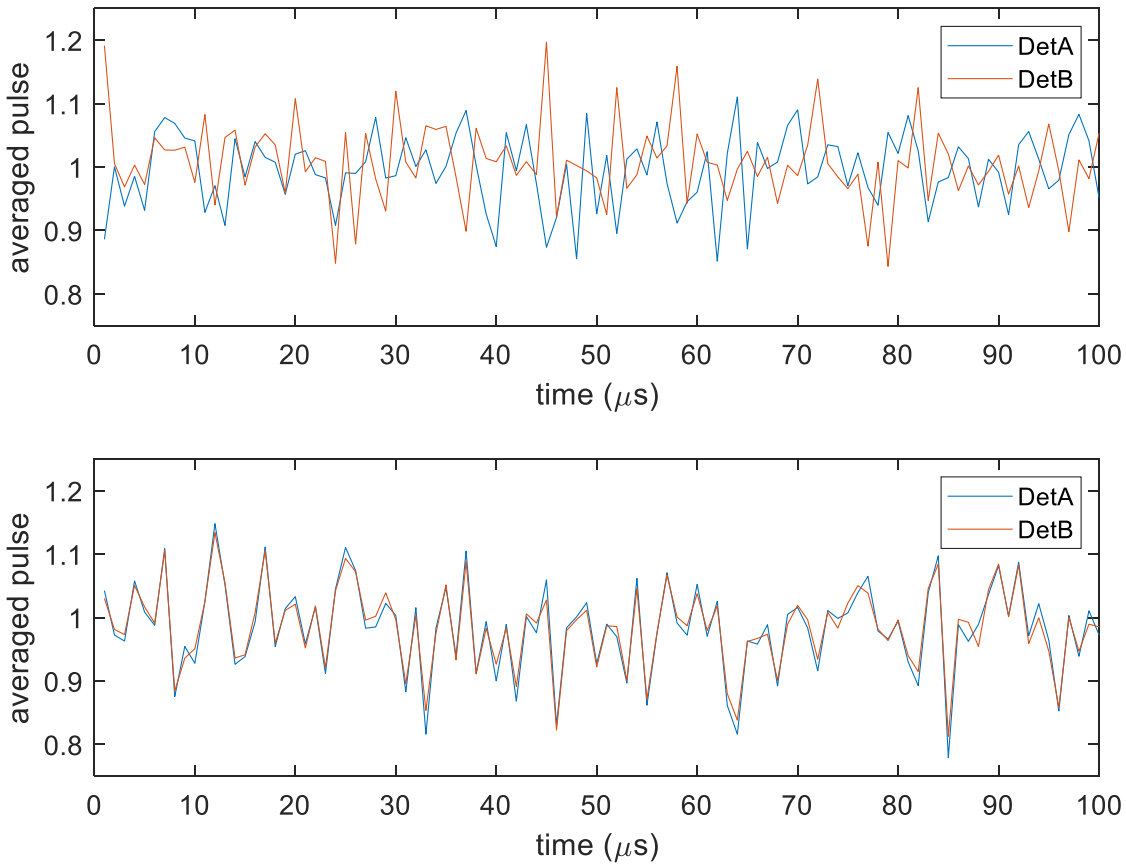

Fig. 2.13. Averaged pulses for both detector channels without (top) and with (bottom) the use of aspheric lenses. The data shown here is truncated for better visualization of the correlation between the two detector channels. Without aspheric lenses, the averaged pulses in DetA and DetB do not have good correlation. When this set of data is normalized, there was no reduction in RIN. With the lenses, there is visible correlation between the averaged pulses captured by the two detector channels. When this data is normalized, there is an improvement to RIN by around -18 dB/Hz.

Aspheric lenses placed directly in front of the detectors helped to focus the entire beam spot onto the detectable area. There is improved correlation between the measured signals on the two detectors, which results in a reduced RIN after pulse-to-pulse normalization. The detectors themselves are optically immersed, i.e. they already have a hyper-hemispherical lens fitted in front of the 1mm×1mm detector active area. However, it is clear that these hyper-hemispherical lenses alone do not optimally fill the detector active area.

When an OCT system is in operation, it is useful to be able to reduce laser power in the reference arm, in order to reduce artefacts and attenuate RIN. Table 2.2 shows two possible methods for reducing laser power and their effect on RIN: using the neutral density (ND)

filters mentioned in Ch 2.2.4 or using an iris diaphragm with a 1mm-diameter aperture. Without normalization, RIN when using the iris diaphragm was -97 dB/Hz, while the RIN when using ND filters was -74 dB/Hz. With normalization, that value was reduced to -115 dB/Hz when using the iris and -92 dB/Hz when using ND filters. Normalization consistently reduced RIN by around -18 dB/Hz for both the ND filters and the iris diaphragm.

Using the iris results in a lower RIN compared to ND filters by 23 dB/Hz. The ND filters attenuate the beam across its entire spot size, while the iris diaphragm only allows a 1mm-diameter section of the beam to pass through. One reason for the discrepancy in RIN between the ND filters and iris diaphragm could therefore be that the laser is a multi-mode laser. The RIN detected using the iris diaphragm might only measure fluctuations from a single mode, while using ND filters meant that the fluctuations from multiple modes are measured. This results in a higher RIN when ND filters are used.

Table 2.2. Methods of laser power reduction and its effect on RIN. Using the iris diaphragm resulted in a lower RIN compared to using ND filters. Normalization consistently reduced RIN by around -18 dB/Hz for both the ND filters and the iris diaphragm. Parameters used: 1 MHz repetition rate, 50ns pulse duration, wavelength fixed at 1400 cm^{-1}, 2000 pulses recorded at 500MS/s sampling rate, ±2V dynamic range.

Method of power reduction	**Normalization?**	**RIN (±0.5 dB/Hz)**
ND filter	N	-74
	Y	-92
Iris diaphragm	N	-97
	Y	-115

2.3.5 Changing repetition rate and pulse width

We investigate whether changing the pulse parameters has any effect on RIN and whether it is feasible to use such a method in future MIR OCT systems. Table 2.3 shows the RIN achieved for different pulse repetition rates, given a constant pulse width of 50ns. In previous experiments using ND filters above, the pulse repetition rate used was 1 MHz, with a pulse width of 50ns. This is once again reflected in this table. Decreasing repetition rate increases RIN. When the repetition rate decreases by 10 times from 1 MHz to 100 kHz, RIN (without normalization) decreases by -16 dB/Hz from -74 dB/Hz to -58 dB/Hz. Reducing the repetition rate even further, to 5kHz, results in a RIN of -49 dB/Hz. At higher repetition rates, there are more pulses within the same time period and hence, as pulse-to-pulse fluctuations are averaged over more pulses, RIN is expected to decrease. These results agree with expectations.

Table 2.3. RIN for different pulse repetition rates. Pulse width for all is 50ns. Increasing repetition rate reduces RIN. Normalization improves RIN on average by -15 dB/Hz.

Repetition rate	**Normalization?**	**RIN (±0.5 dB/Hz)**
1 MHz	N	-74
	Y	-92
100 kHz	N	-58
	Y	-74
5 kHz	N	-49
	Y	-60

Next, we investigate the effect of changing pulse width on RIN. Our goal was to investigate whether pulse-to-pulse variation might fall if each pulse value represented an average over a

larger emission duration. Table 2.4 shows the value of RIN for different pulse widths, with and without normalization. Due to duty cycle limits imposed on the laser by the manufacturer, the pulse repetition rate is kept at a low value of 5kHz for all these measurements. As the pulse width is increased, the laser pulse energy also increases. Since changing the averaging duration along the laser pulse was found to have a very small effect on RIN calculations, changing the pulse width is not expected to have a large effect on RIN. As the pulse width increases from 50ns to 100ns to the maximum of 500ns, RIN only decreases slightly from -49 dB/Hz to -52 dB/Hz and to -55 dB/Hz.

Table 2.4. RIN for different pulse widths. The pulse repetition rate used here is reduced to 5 kHz for all pulse width, in order to accommodate the duty cycle limit.

Pulse width (ns)	**Normalization?**	**RIN (±0.5 dB/Hz)**
50	N	-49
	Y	-60
100	N	-52
	Y	-66
500	N	-55
	Y	-68

2.3.6 Changing emission wavelength

Fig. 2.14 shows the shape of a laser pulse at wavelengths with high and low emission power. At a wavelength with high emission power (λ = 5.8 μm), the value of RIN without normalization is -58 dB/Hz. At a wavelength with low emission power (λ = 7.4 μm), the value of RIN is -61 dB/Hz. Although the laser was set to emit 500ns pulses at both wavelengths, the

resultant pulse width at λ = 7.4 µm is only around 150ns. Similar levels of RIN was achieved regardless of emission wavelength.

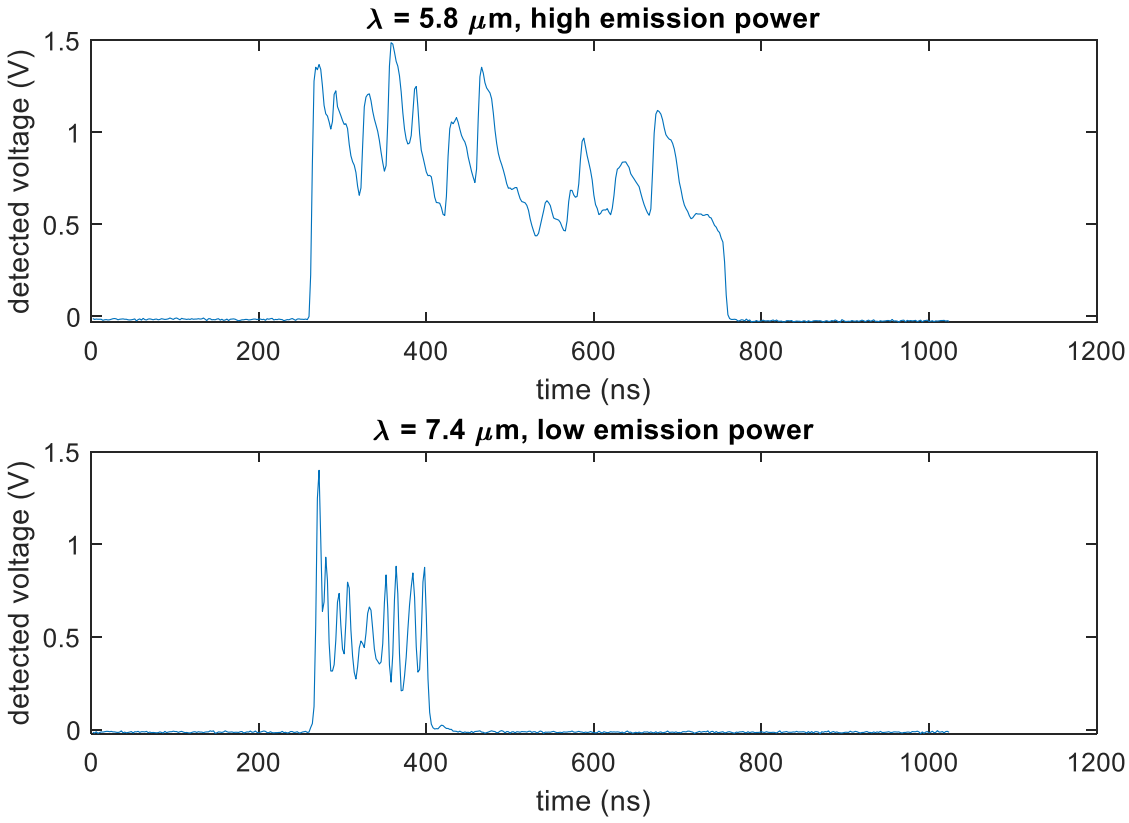

Fig. 2.14. Pulse profile of a single 500ns pulse at two different wavelengths. Top: wavelength with high emission power. The value of RIN at a wavelength of 5.8 µm is -58 dB/Hz. Bottom: wavelength with low emission power. The value of RIN at this wavelength (λ = 7.4 µm) is -61 dB/Hz. Although the laser is set to emit with a 500ns pulse width, the measured pulse width is only ~150ns. Pulse parameters: 5 kHz repetition rate, 500ns nominal pulse width.

2.4 Discussion & Future Outlook

In this paper, we attempted to characterize RIN in more detail. Firstly, by using a soldering iron as a continuous source of mid-infrared black-body radiation, the value of RIN calculated gives us an indication of the lowest possible value of RIN that can be attained using this detection system. Regardless of the pulse-to-pulse stability of the laser output, the minimum RIN that can be measured is -133 dB/Hz when using an input range of ±0.4V. Increasing the input range of the ADC increases the RIN calculated. Subsequent experiments used a dynamic

range of ±2V. The lowest attainable RIN that can be measured is therefore -123 dB/Hz. All RIN values calculated subsequently are above this limit.

Regardless of the experimental setup and pulse parameters, normalization consistently reduces RIN by about -15dB/Hz. The use of aspheric lenses was essential in focusing the beam spot onto the detector's optical area for pulse-to-pulse normalization. Without the aspheric lenses, the averaged pulses from DetA and DetB had much reduced correlation between each other. With the lenses, normalization helped to reduce RIN from -74 dB/Hz to -92 dB/Hz, given a pulse repetition rate of 1MHz and pulse width of 50ns.

Using an iris diaphragm to reduce laser output power resulted in a lower RIN compared to ND filters. When using the iris diaphragm, it is possible to reduce RIN to -115 dB/Hz with normalization. This is the lowest RIN measured in this paper. The reason for this discrepancy in RIN using the two methods could be due to the fact that the ND filter is a nickel coated highly parallel zinc selenide plate, which could have introduced additional noise into the system due-to Fabry-Perot effect.

At higher repetition rates, there are more pulses within the same time period and hence, RIN is expected to decrease. Our results agreed with these expectations. Changing the pulse width had little beneficial effect on RIN. This is because changing the pulse width is essentially changing the averaging length during RIN calculations and as previously shown, changing the averaging length had negligible effect on RIN. Due to duty cycle constraints, there is a limit on how much RIN can be reduced by simply changing pulse parameters.

We have characterized RIN for a fixed emission wavelength. The next step would be to quantify RIN while using the Michelson interferometer setup shown in Fig. 2.4. The laser

would be swept across a range of wavelengths and we would investigate whether using pulse-to-pulse normalization can improve the signal-to-noise ratio.

References

[1] W.C. Lin, D.G. Revin, and S.J. Matcher, "Methods for reducing relative intensity noise in swept-source mid-infrared OCT," Proc. SPIE **11359**, 113590P (2020).

[2] W.C. Lin, and S.J. Matcher, “Swept-source OCT using pulsed mid-infrared light,” Proc. SPIE **10890**, 108902D (2019).

[3] D.T. Childs, R.A. Hogg, D.G. Revin, I.U. Rehman, J.W. Cockburn, and S.J. Matcher, “Sensitivity advantage of QCL tunable-laser mid-infrared spectroscopy over FTIR spectroscopy,” Appl. Spectrosc. Rev. **50**(10), 822-839 (2015).

[4] D.T.D. Childs, R.A. Hogg, D.G. Revin, I.U. Rehman, J.W. Cockburn, and S.J. Matcher, “The mid-infrared swept laser: life beyond OCT?,” Proc. SPIE **9312**, 9312-39 (2015).

[5] I. Zorin, R. Su, A. Prylepa, J. Kilgus, M. Brandstetter, and B. Heise, “Mid-infrared Fourier-domain optical coherence tomography with a pyroelectric linear array,” Opt. Express **26**(25), 33428-33439 (2018).

[6] C.S. Colley, J.C. Hebden, D.T. Delpy, A.D. Cambrey, R.A. Brown, E.A. Zibik, W.H. Ng, L.R. Wilson, and J.W. Cockburn, “Mid-infrared optical coherence tomography,” Rev. Sci. Instrum. **78**(12), 123108 (2007).

[7] N.M. Israelsen, C.R. Petersen, A. Barh, D. Jain, M. Jensen, G. Hannesschläger, P. Tidemand-Lichtenberg, C. Pedersen, A. Podoleanu, and O. Bang, “Real-time high-resolution mid-infrared optical coherence tomography,” Light Sci. Appl. **8**(1), 1-13 (2019).

[8] S. Freer, D. Revin, K. Groom, and S.J. Matcher, “Towards swept-source mid-infrared OCT,” Biophotonics: Photonic Solutions for Better Health Care VI, 70 (2018).

Chapter 3: Imaging of Birefringence in Striae Distensae

The contents of this chapter have been previously published in [1].

Imaging striae distensae: a comparison between PS-OCT and digital dermoscopy

Wai Ching Lin[1], Robert A Byers[1,2], Wei Li[1], Simon G Danby[2], Michael J Cork[2], and Stephen J Matcher[1]

[1] Department of Electronic and Electrical Engineering, University of Sheffield, Sir Frederick Mappin Building, Sheffield, S1 3JD, UK

[2] Sheffield Dermatology Research, Department of Infection & Immunity & Cardiovascular Disease, University of Sheffield, Beech Hill Road, Sheffield, S10 2RX, UK

Abstract

Stretch marks or striae distensae (SD) cause emotional distress and negatively affect the psychological well-being of patients. We investigate and compare two methods for quantifying the severity of SD: visual scoring of images captured using a clinical visible-light dermatological camera (C-Cube, Pixience Inc) and measuring the local birefringence of skin using polarization-sensitive optical coherence tomography (PS-OCT). Data on skin visually affected by SD and visually normal skin were collected from 19 human volunteers. Our results show a weak correlation between visual scores of the C-Cube images and the birefringence values obtained from the PS-OCT system. SD datasets have a significantly larger birefringence values compared to visually normal datasets.

3.1 Introduction

Striae distensae (SD), more commonly known as stretch marks, are dermal scarring lesions on the skin [2]. They are caused by excess mechanical stretching of the dermis over time [3, 4], an increase in hormonal receptor activity [5] and/or a reduced expression of collagen, elastin and fibronectin [6]. An initial reaction in dermal collagen expression is hypothesized to mechanically weaken the dermis and make it susceptible to tearing. The resulting wound-healing response lays down scar tissue of highly aligned collagen and elastin, which forms the visible SD. They are aesthetically undesirable, place a psychosocial burden on patients and negatively affect their quality of life [7,8]. SD often occurs as a result of pregnancy (striae gravidarum), obesity and growth spurts [9]. Risk factors for SD include Cushing syndrome and chronic corticosteroid usage [4]. Treatment for SD typically involve the use of topical products, either therapeutically or prophylactically [2]. Topical tretinoin is one such product [10,11]. Chemical peel treatments [12], Galvano-puncture [13] and laser-based treatments [14] are also available. The goal of most treatments is to stimulate collagen production and realignment [7].

SD typically begin as reddish lesions [2] called striae rubra (SR). These appear as raised, erythematous regions with a pink to reddish coloration [9]. Over time, the epidermis gradually atrophies and SR progresses into atrophic, hypopigmented (white) lesions called striae alba (SA). SA lesions are flatter and more depressed compared to surrounding healthy tissue [15].

Currently, no gold standard exists for quantifying SD severity. Many studies and clinical trials investigating treatment efficacy used subjective scoring systems that vary from study to study [7]. Some studies numerically rate photographs of SD skin [10] or survey patient satisfaction

[11], while others measure the length and width of SD lesions [11]. Biopsies for histological staining are also commonly used for a more objective but still qualitative measurement [10,11]. A recent study by Cho et al. [9] compared SD skin and healthy skin by measuring a number of biophysical properties. They found that SD skin had higher surface roughness [9,15], lower skin elasticity [9] and lower dermal echo density [9]. However, the study did not attempt to quantify SD severity through these methods. There is a need for objective measurement tools that can quickly and accurately detect the localized health of the skin. The reliance of such a tool on subjective evaluation should be minimal. To develop such a measurement standard, it is necessary to have a marker that can quantify a physiological property of the skin that differentiates SD skin from normal skin.

Optical coherence tomography (OCT) is a non-invasive imaging modality that detects near-infrared light backscattered from the tissue sample. It produces high-resolution cross-sectional images of tissue morphology. It has a penetration depth of a few millimeters [16] and is capable of imaging the epidermis and dermis of skin tissue [17]. Polarization-sensitive (PS) OCT is a functional extension to OCT. Polarimetric information measured by the PS-OCT is used to find the phase retardance [18,19] and fast birefringent axis orientation [20] of the sample. The phase retardance is especially useful in estimating birefringence, the degree of fiber alignment in tissues. This is particularly useful in fibrous tissues with a high degree of collagen and elastin. PS-OCT has been successfully utilized in dermatology [17], ophthalmology [21], dentistry [22] and an enhanced study of bones, tendons, ligaments and cartilage [23]. To date, there have been no known studies measuring the birefringent properties of SD skin.

The onset of SD results in changes to the collagen and elastin fiber alignment within the skin. In healthy skin, elastin and collagen fibres are arranged in a random orientation [7]. Regardless of the specific cause, SD onset results in an over-production of elastin and collagen over time. Histological specimens show densely packed elastin and collagen fibres aligned parallel to the skin [7]. We hypothesize that this increase in fibre alignment will result in an increase in the localized phase retardance, leading to quantifiable differences in the birefringence between SD and healthy skin.

This paper aims to assess the feasibility of using PS-OCT in objectively quantifying SD severity. It is an exploratory study to measure the birefringence of SD and healthy skin. Results from the PS-OCT measurements will be compared against subjective visual scoring.

3.2 Method

3.2.1 Participants

This study was favourably reviewed by The University of Sheffield Research Ethics Committee (UREC #030680). 19 adult volunteers were recruited and the striae in different locations around their body were imaged. Participants were screened against other skin conditions such as eczema, acne, suntan, hyperpigmentation, tattoos, blemishes and dense body hair.

A total of 75 datasets containing striae were collected. These were visually inspected at the time of screening to categorize them as either striae rubra or striae alba. For each dataset, a corresponding dataset at a site adjacent to the affected skin was also collected. This adjacent dataset is hereafter referred to as “healthy” data, whilst recognizing that it may possibly correspond to sub-clinical SD skin.

3.2.2 C-Cube imaging and scoring

A clinical visible-light dermatological camera (C-Cube, Pixience Inc, France) was used to capture high-resolution close-up en-face images of the skin. It is able to image the region of interest under controlled lighting conditions, thus giving a more objective view of the striae lesions that is unaffected by surrounding ambient light intensity and direction. The camera also has a mode that estimates surface profiles from shading, but this mode was not used here. If the participant presents with more than one striae lesion, multiple scans were acquired. Each 2D C-Cube image covers an area of approximately 16×12 mm. A black marker, approved for dermatological use, was used to mark the center of the images to ensure the same area was imaged by both C-Cube and PS-OCT. Visual scoring of the striae-affect C-Cube images was done using the criteria shown in Table 3.1. The images were scored by 3 individuals independently and then the arithmetic mean of these scores was reported. To our knowledge, there is no agreed upon scoring system for quantifying SD severity. In a comparable study, Rangel et al have used a scoring system for quantifying SD severity by rating photographs [10]. However, this scoring system gave a numerical score based on the improvement in SD lesions after treatment rather than the severity of each lesion. Therefore, the scoring system used here was generated in our lab for this study.

Table 3.1. Criteria for visual scoring of striae using C-Cube images

Score	Description of C-Cube image
0	No visible striae
1	Barely perceptible striae
2	Visible striae
3	Clear visible striae with evidence of deep furrows

3.2.3 PS-OCT data collection

The OCT system used is a polarization-maintaining (PM) fiber-based PS-OCT system. Its configuration was first reported by Al-Quasi et al in [24]. A more detailed report of our in-house system can be found in [25]. Fig. 3.1 shows a schematic diagram of the setup. The measured axial resolution of the system is approximately 10 µm in air. The light source used is a commercially available swept-source laser (HSL-2000-10-MDL, Santec, Japan) with a center wavelength of 1315 nm and a full-width-half-maximum (FWHM) of 128 nm. It has a sweep range of 157 nm and a sweep rate of 10 kHz. The laser has a duty cycle of 60% and an output power of 10mW.

The setup in Fig. 3.1 is a Mach-Zehnder interferometer that uses Panda PM-fibers. The laser output beam first passes through a polarization controller (PC) and an in-line linear polarizer (IL-LP), which ensures linearly polarized light. Using a 2x2 PM coupler (PMC1, OLCPLP-22-131-10-90-FA, Opto-link Corp., China), the light beam is split into the reference arm and sample arm in a 10:90 ratio. A pair of three-port PM circulators (C, OLCIR-P-3-131-300-90-FA, Opto-link Corp., China) direct the light beams to the sample and reference reflector. In the reference arm, the light beam passes through a linear polarizer (LP) oriented at 45° to the slow axis of the PM-fiber before being reflected by a static plane mirror. Light in the sample arm is passed through a quarter wave plate (QWP, NT55-547, Edmund Optics, USA) whose fast-axis is oriented at 45° to the fast-axis of the PM fiber, thus converting the polarization to a circular state before reaching the sample. A set of 2 galvanometers (Galvo, 6215, Cambridge Technology, USA) raster scan the beam in the en-face plane. Light from both arms interfere when they reach the second PM coupler (PMC2, OLCPL-P-22-131-50-90-FA, Opto-link Corp., China). After the light beam is separated into horizontal (H) and vertical (V) polarization states

using polarizing beam splitters (PBS, PBS-31-P-2-L-3-Q, NovaWave Techno., USA), they are detected by two balanced detection channels (1817-FC, New Focus, USA). A 14-bit transient recorder (M2i.4022, Spectrum GmbH, Germany) is used to measure the two signals at a 20 MS/s sampling rate.

A MATLAB graphical user interface (GUI) was used to control the system and capture volumetric C-scans.

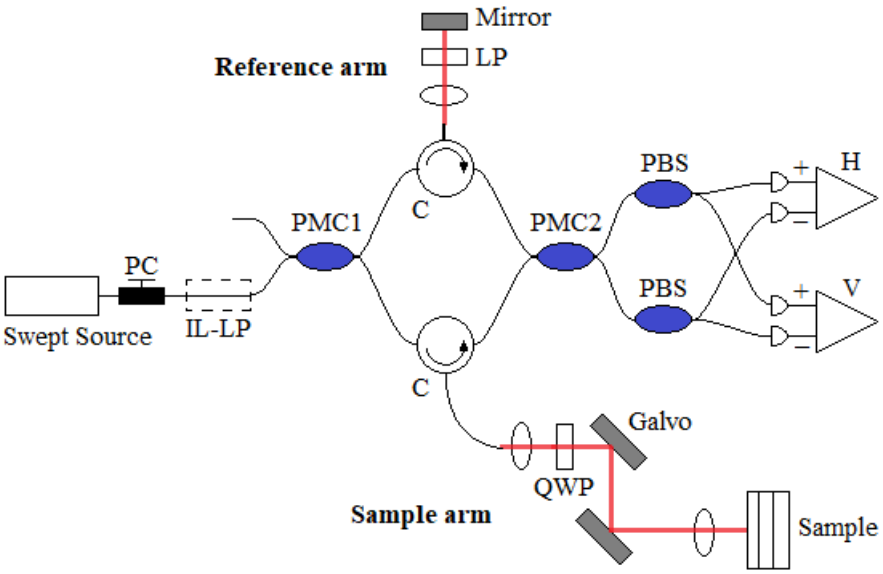

Fig. 3.1. Schematic diagram of PS-OCT system. A swept-source light beam passes through a polarization controller (PC) and an in-line polarizer (IL-LP). A polarization-maintaining coupler (PMC1) and PM circulators (C) split the beam into reference and sample arms in a 10:90 ratio. In the reference arm, the beam passes through a linear polarizer (LP) and reflects off a mirror. Light in the sample arm is passed through a quarter wave plate (QWP) before reaching the sample. 2 galvanometers (Galvo) allow volumetric scanning. Interference from both arms occur at a second PM coupler (PMC2). The signals are separated using 2 polarizing beamsplitters (PBS) into horizontal (H) and vertical (V) channels before being detected by 2 balanced detectors.

3.2.4 PS-OCT image processing

Each volume scan covers an area of 6×6mm with a lateral step size of 10 µm. All data processing steps were done in MATLAB (2019a, MATLAB) with the Signal Processing, Image Processing and Wavelet toolboxes. A fast Fourier transform (FFT) was performed on each raw

interferometric signal to obtain the intensity profile of each A-scan. A wavelet-FFT filtering algorithm was applied to remove the presence of ghost artifacts in the B-scans, which are caused by mode dispersion in the PM fibers [26]. A surface flattening algorithm was also used to detect and flatten the surface of each C-scan [26].

Both the amplitude and phase of the horizontal and vertical signals were used to calculate the Stokes vector (S) of each voxel. The Stokes vector was computed using Eq. (3.1), which was taken from [27].

$$S = \begin{pmatrix} I \\ Q \\ U \\ V \end{pmatrix} = \begin{pmatrix} {A_V}^2 + {A_H}^2 \\ {A_V}^2 - {A_H}^2 \\ 2A_V A_H \cos\Delta\phi \\ 2A_V A_H \sin\Delta\phi \end{pmatrix} \tag{3.1}$$

I, *Q*, *U* and *V* are elements of the Stokes vector. $A_{H,V}$ are the amplitudes of the horizontal and vertical channels respectively, while $\Delta\phi$ is the phase difference between the vertical and horizontal signals. The Stokes vector in Eq. (3.1) is further normalized by dividing the *Q*, *U*, *V* values by *I*, as shown by Eq. (3.2). The conversion of Stokes vectors into an enface image of birefringence broadly follows the procedure described by Chin et al. [28].

$$\hat{S} = \begin{pmatrix} \hat{Q} \\ \hat{U} \\ \hat{V} \end{pmatrix} = \begin{pmatrix} \mathrm{Q/I} \\ \mathrm{U/I} \\ \mathrm{V/I} \end{pmatrix} \tag{3.2}$$

The phase retardance at a discrete depth z_i (ϕ_r) can be calculated by taking the dot product between the Stokes vector at the surface $\hat{S}_{ref}$ and the Stokes vector at z_i [Eq. (3.3)]. The derivation of Eq. (3.3) is explained in greater detail by Chin et al. [28]. On the assumption of weakly varying sample fast-axis orientation with depth, local birefringence can then be estimated by the local gradient of ϕ_r with respect to depth. To give a more precise estimate of the gradient and reduce the effects of random noise, 2D averaging using a 3×3 pool is

performed on the Stokes vectors before the dot product is computed. In other words, the averaged Stokes vector was calculated by finding the arithmetic mean of every 3×3 block of Stokes vectors.

$$\cos \phi_r(z_i) = \hat{S}_{ref} \cdot \hat{S}(z_i) \qquad (3.3)$$

The phase retardance profile $\phi_r(z_i)$ is demodulated by forming the analytic signal of Eq. (3.3) and finding the resulting phase angle, which yields the demodulated wrapped phase retardance ϕ_w. The latter is unwrapped by using the *unwrap* function in MATLAB. Using a simple linear regression, the slope of the unwrapped phase retardance was calculated at a depth of 3 – 53 pixels from the surface of the skin, which correlates to a depth of 12 – 212 µm. The slope of the unwrapped phase retardance $\delta\phi_w$ is converted to an estimate of the tissue birefringence Δn using Eq. (3.4):

$$\Delta n = \frac{\delta\phi_w(\lambda_0)(RI)}{4\pi(\Delta z)} \qquad (3.4)$$

where λ_0 is the central wavelength of the PS-OCT system (1301 nm), Δz represents the pixel size in air (4 µm) and RI is the refractive index of tissue (1.4). This estimate of the tissue birefringence *Δn*, calculated using the slope of phase retardance, represents the combined effect of local birefringence and fast optic axis of the tissue.

An important caveat about our measurements of tissue birefringence is that we measure what we have previously termed the “apparent birefringence”. This only equals the “true birefringence” when the collagen fibers are aligned parallel to the skin surface [25]. The clinical etiology of SD is that they orient themselves along tears in the dermal collagen, i.e. along directions of maximum tensile stress [29]. Therefore, we consider it reasonable to assume that the fast optic axis is constant with respect to depth and the slope of phase retardance is proportional to tissue birefringence. As healthy skin consists of randomly

oriented collagen and elastin fibres, the slope of the phase retardance in healthy skin is expected to be approximately zero.

3.2.5 Thresholding and (un)wrapping

Unwrapping the phase retardance prior to slope estimation produced artifacts within the tissue birefringence image in areas of low expected tissue birefringence. In Fig. 3.2 (left), the en-face tissue birefringence image was calculated with the phase retardance ϕ_w unwrapped. Areas with striae show high tissue birefringence (>1.5×10^{-3}) as expected, but areas where there should be no striae, for example in the white circle, also seem to have high tissue birefringence. Conversely, when the tissue birefringence image was calculated using the wrapped phase retardance, as in Fig. 3.2 (right), areas without striae have low tissue birefringence. However, areas of high tissue birefringence, for example in the black circle, also have very low (close to zero) tissue birefringence. To understand the reason for this, we look at the phase retardance profiles at these locations.

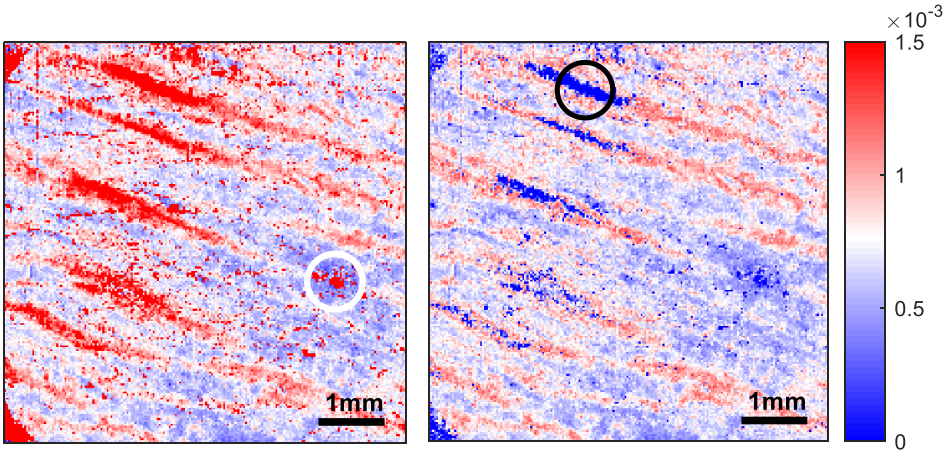

Fig. 3.2. Example of tissue birefringence image with artifacts. The overall C-Cube visual score is 1. Left: Local tissue birefringence estimated using the unwrapped phase retardance. Areas with striae show high tissue birefringence, but areas where there should be no striae (white circle) show uncommonly high tissue birefringence. Right: Local tissue birefringence estimated using wrapped phase retardance. Areas where striae are located (black circle) should have high tissue birefringence (>1.5×10^{-3}) but instead the tissue birefringence calculated is close to zero.

Firstly, Fig. 3.3 shows the demodulated wrapped phase retardance (ϕ_w) profile of an A-scan in the black circle in Fig. 3.2. The structural and retardance images at the top of the figure include a dashed vertical line, which shows the A-scan location used to calculated the phase retardance profile. The centre graph shows a close-up of the wrapped phase retardance with respect to depth. The phase increases as the depth increases. At a depth of 136 μm, the phase 'wraps' and decreases sharply by 2π. However, the slope of the phase profile before and after this phase jump is similar. With increasing depth, noise becomes more prevalent and it is impossible to reliably determine where other phase wraps occur. Slope estimation by linear regression occurs in between the 2 red dots at a depth of 12-212 μm. The slope calculated is close to zero due to the phase wrap.

The bottom graph in Fig. 3.3 includes both the wrapped and unwrapped phase profile. When the phase is unwrapped, slope estimation between the 2 points is positive and an accurate indication the birefringence. After 600 μm, where noise becomes more prevalent, the unwrapping algorithm is unable to reliably determine a true phase wrap. Noise fluctuations cause the unwrapping algorithm to incorrectly add 2π phase offsets at numerous locations. Thus, the slope after 600 μm becomes artifactually higher than the slope calculated at 12 – 212 μm.

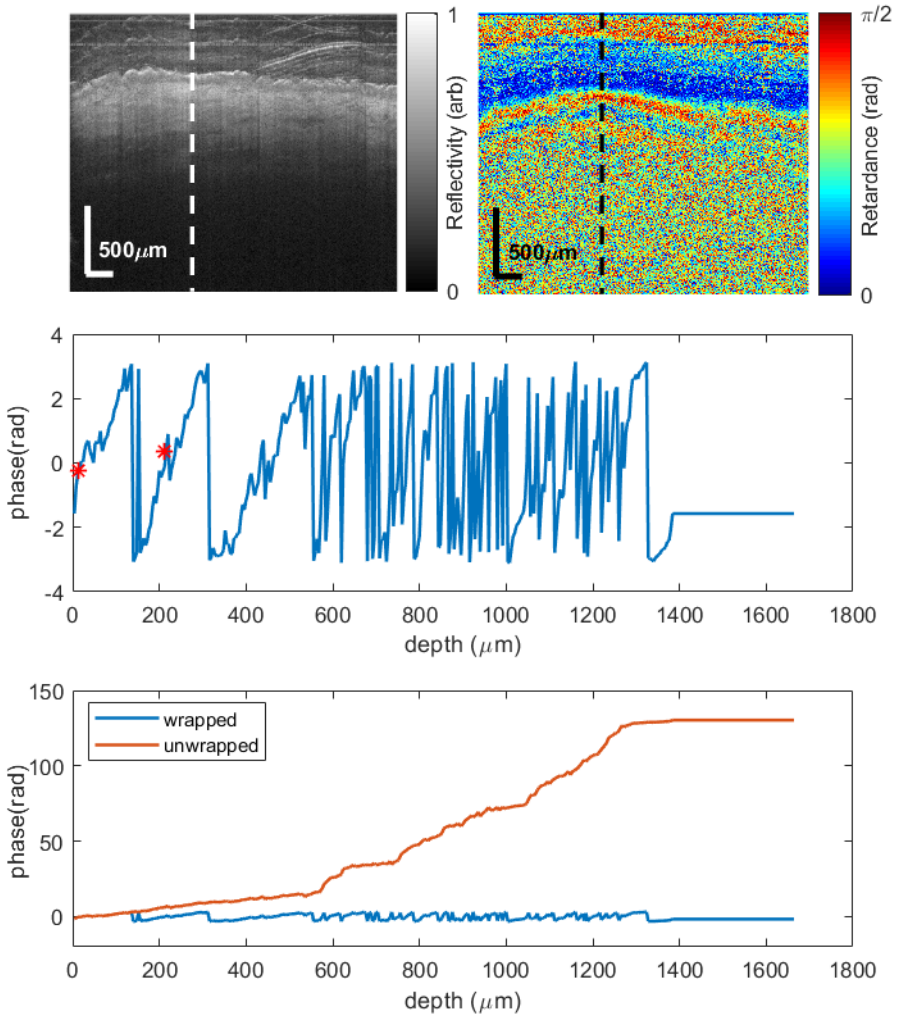

Fig. 3.3. Demodulated wrapped and unwrapped phase retardance (ϕ_w) profile of a region with striae (high expected birefringence). Top: Structural and retardance images of the region of interest. The dashed vertical line shows the shows the A-scan location used for the phase retardance profiles. Centre: close-up of the wrapped phase retardance. The phase increases as the depth increases. At 136 µm, the phase 'wraps' and decreases sharply by 2π. The slope is estimated using the profile between the two red points. Bottom: graph of both the wrapped and unwrapped phase. When the phase is unwrapped, slope estimation between the 2 points is positive and indicative of the true birefringence value. After 600 µm, noise becomes more prevalent and the unwrapping algorithm is unable to reliably detect a true phase wrap from noise.

Fig. 3.4 shows a phase retardance profile of a voxel within the white circle in Fig. 3.2, a low-birefringence (based on visual inspection) region of a striae image. This is a region without striae and tissue birefringence is expected to be close to zero. There are no clear signs of a true phase wrap within this phase profile. In fact, the entire phase profile is dominated by noise. The slope estimated is thus approximately zero. The bottom graph in Fig. 3.4 shows both the wrapped and unwrapped phase. When the phase is unwrapped, it increases at a

higher rate compared to the unwrapped phase in Fig. 3.3. For instance, in Fig. 3.4, at a depth of 12 – 212 µm, the phase increases from around 0 to 27 rad. At the same depth, the phase in Fig. 3.3 only increased by 6 rad. This is because MATLAB's *unwrap* function cannot distinguish between a true phase wrap and noise. Most of the unwrapping in Fig. 3.4 is due to noise, and the subsequent slope and hence tissue birefringence calculated are not indicative of striae severity. In these instances of high noise and low tissue birefringence, the slope estimated using the wrapped phase is more accurate.

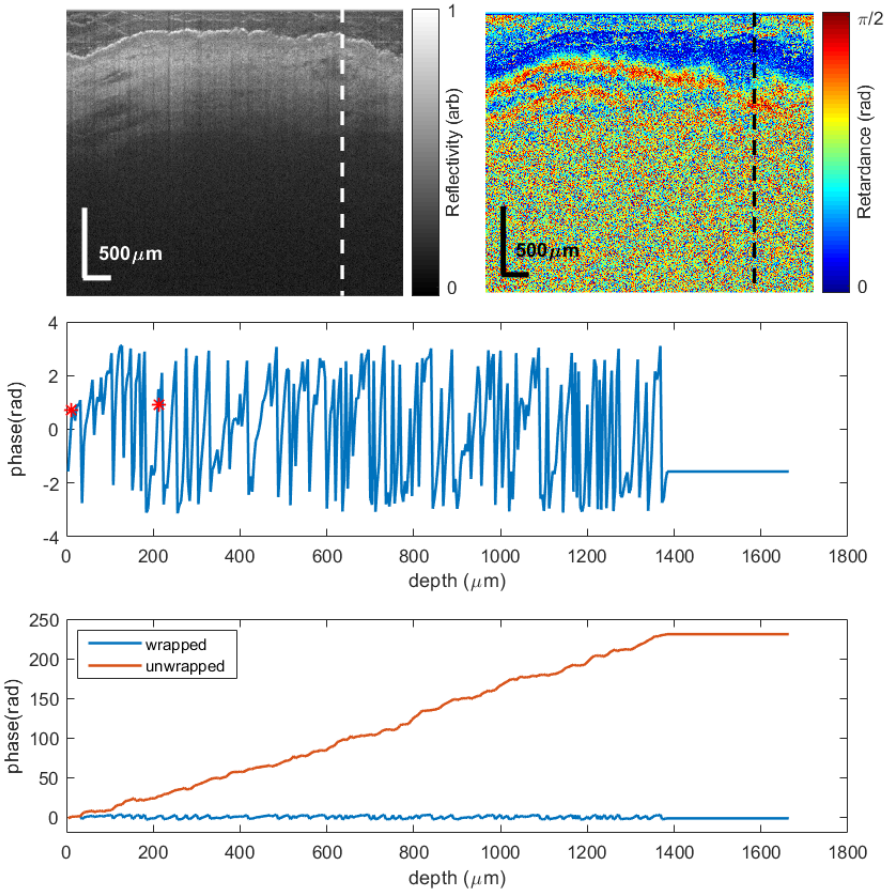

Fig. 3.4. Demodulated wrapped and unwrapped phase retardance profile of a healthy region (low expected birefringence). Top: Structural and retardance images of the region of interest. The dashed vertical line shows the shows the A-scan location used for the phase retardance profiles. Centre: close-up of the wrapped phase retardance profile. There are no clear signs that a wrap has occurred within this phase profile. The slope estimated between the two red points is approximately zero. Bottom: wrapped and unwrapped phase profiles. At a depth of 12 – 212 µm, the phase increases from 0 to 27 rad. At the same depth in Fig. 3.3, the phase only increased by 6 rad. Most of the unwrapped phase jumps in this graph is due to noise.

To improve the accuracy of tissue birefringence estimations, it is necessary to separate voxels of high noise from those with genuinely high tissue birefringence. Fig. 3.5 shows histograms of the wrapped and unwrapped enface images. For the wrapped image, there are a large number of pixels with zero tissue birefringence due to the aforementioned issues. The zero-slope estimate means the voxel is either a non-striae region or a striae region with a wrapped phase. The maximum tissue birefringence calculated in the wrapped image is around 1.5×10^{-3}. The unwrapped image had a greater range of tissue birefringence values. There are a small number of pixels with tissue birefringence larger than the 5×10^{-3} shown in the graph. They have been truncated from this histogram for ease of viewing. As discussed above, regions of low tissue birefringence and high noise tend to have slopes (and hence estimated tissue birefringence) that are higher than striae regions, when unwrapped phase profiles are used. Tissue birefringence values are first estimated using the unwrapped phase. By looking at the histogram plot, we can select a threshold (for this dataset, it is 3×10^{-3}). For any pixel exceeding this threshold, the tissue birefringence value is re-calculated using the original, wrapped phase profile. Fig. 3.6 highlights all pixels above this threshold in black. Only healthy regions with low expected tissue birefringence are highlighted.

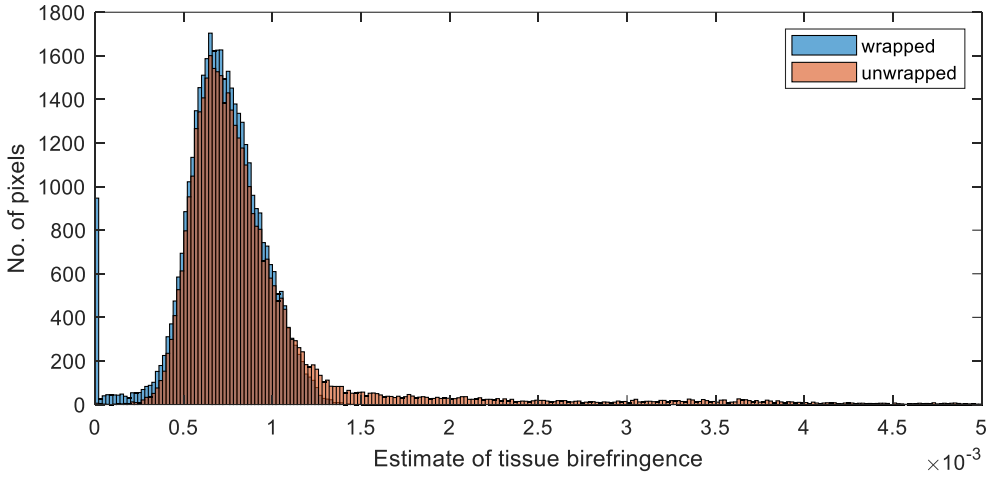

Fig. 3.5. Histogram of wrapped and unwrapped enface local tissue birefringence image. In the wrapped histogram, there are a large number of pixels with zero tissue birefringence. The maximum tissue birefringence calculated in the wrapped image is around 1.5×10^{-3}. The unwrapped histogram has a greater range of tissue birefringence values, but the histogram is truncated at 5×10^{-3} for ease of viewing.

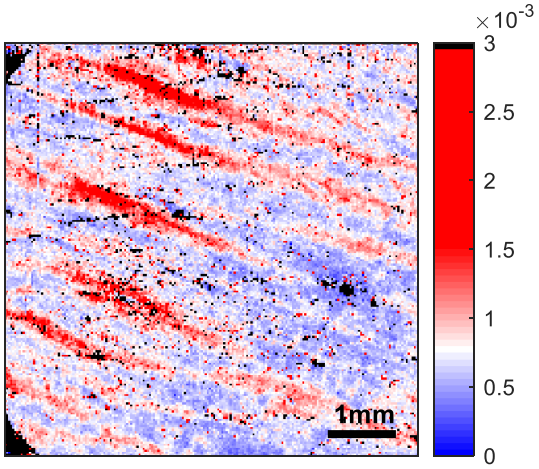

Fig. 3.6. Enface image of tissue birefringence (estimated using the unwrapped phase), with black pixels highlighting areas where the tissue birefringence is larger than 3×10^{-3}.

Fig. 3.7 (left) shows the result of using this thresholding. Areas with striae now have high tissue birefringence values (up to the threshold of 3×10^{-3}), while areas without striae have low tissue birefringence values.

However, speckle noise is still present in the image, which could affect the statistical analysis of tissue birefringence values within the image. To reduce this noise, a 3×3 median filter is

applied. Fig. 3.7 (right) shows the enface image after median filtering. While the image resolution is reduced, the speckle noise has also reduced.

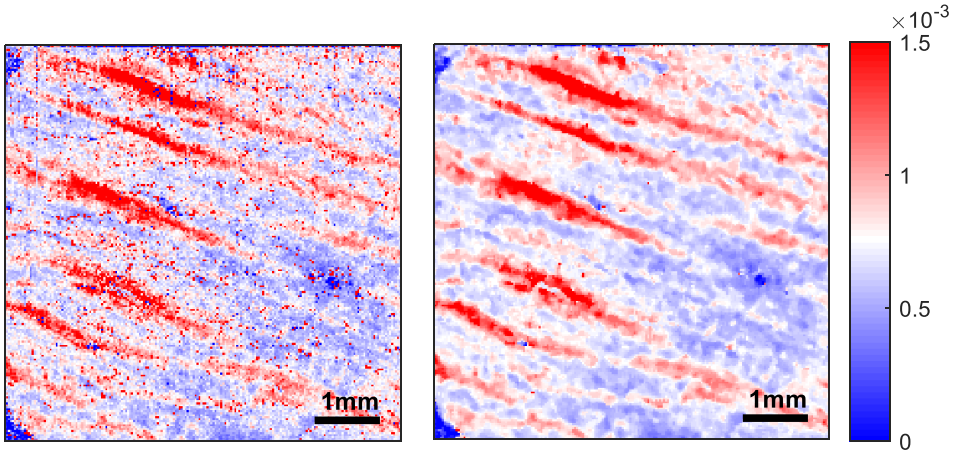

Fig. 3.7. Enface image of tissue birefringence after thresholding. Left: Pixels with a tissue birefringence value higher than 3×10^{-3} use the wrapped phase for slope estimations, and vice versa. Right: Enface image of tissue birefringence after thresholding and applying a 3×3 median filter.

Thresholding was only applied to images where it is clear that the areas without striae have high birefringence. The threshold is selected individually for each image. If the threshold chosen is too high, areas without striae would still have a high tissue birefringence. The modified image would look like the image in Fig. 3.2 (left). If the threshold is too low, regions of striae in the modified image would have low tissue birefringence. The resultant image would look similar to Fig. 3.2 (right).

3.3 Results and discussion

A total of 150 datasets were collected, 75 samples with striae and 75 samples of adjacent healthy skin. Each dataset comprises of a photograph captured by the C-Cube camera and a volume scan measured using the PS-OCT system. Of the samples with striae, 60 were of striae alba, 11 were of striae rubra and the remaining 4 were classified as a mixture of both. Fig. 3.8 shows an example of striae rubra and striae alba. The images on the left were taken using the

C-Cube camera and the images on the right show the enface images of tissue birefringence. N.B. the angular offset is not matched between the different imaging modalities. The top image in Fig. 3.8 is an example of striae rubra, which has an overall visual score of 1. The bottom image, an example of striae alba, has a score of 2. In the tissue birefringence images, there are clear differences between areas of healthy skin (low tissue birefringence, coloured blue) and areas of striae (high tissue birefringence, coloured red). Moreover, the sample with striae alba is visibly more severe than the sample with striae rubra in terms of the area covered and the level of tissue birefringence.

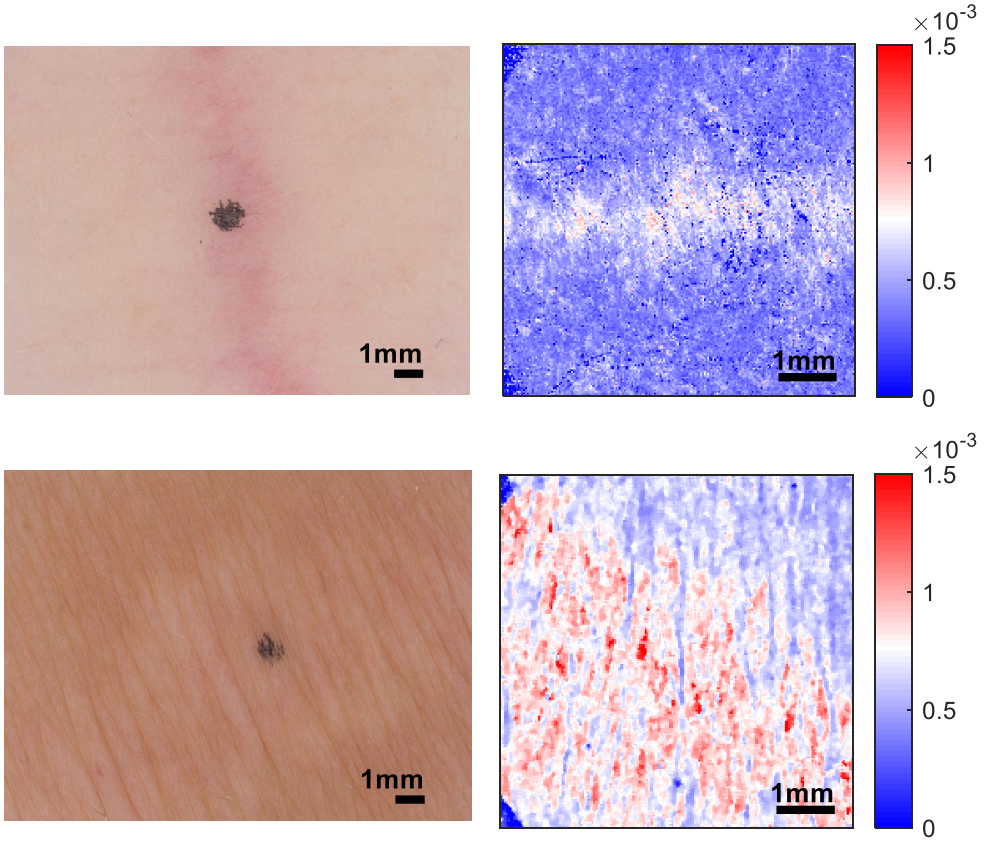

Fig. 3.8. Examples of striae rubra (top) and striae alba (bottom). The images on the left are from the C-Cube camera; the images on the right from the PS-OCT. Striae rubra: overall visual score of 1. Striae alba: overall visual score of 2. N.B. the angular offset is not matched between the different imaging modalities. For instance, in the striae rubra example, the PS-OCT image has been rotated by 90° compared to the C-CUBE image.

In contrast, Fig. 3.9 shows an example of healthy skin. This sample is the corresponding healthy dataset to the striae alba sample in Fig. 3.8. Both the C-Cube and tissue birefringence images in Fig. 3.9 are more uniform in appearance.

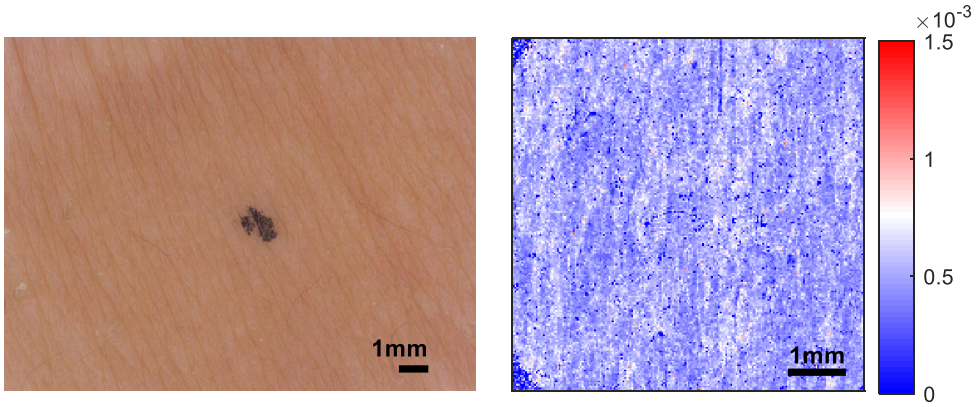

Fig. 3.9. Example of healthy skin. Left: C-Cube image. Right: enface image of tissue birefringence. This sample was the corresponding healthy dataset to the striae alba sample in Fig. 3.8. N.B. the angular offset is not matched between the different imaging modalities.

Table 3.2 summarizes the number of samples categorized into each visual score category. The overall visual score is an average of 3 independent scorings, rounded to the nearest 0.5. Even though striae lesions were considered to be visually apparent during the screening, 6 of the striae-affected samples had a score of zero (no visible striae). This is because the scoring is judged from the C-Cube images and we sometimes find, particularly for the non-pigmented striae alba, that the striae-affected skin do not look like they have striae under the controlled lighting conditions of the C-Cube camera. C-Cube images with striae rubra are more likely to be given a higher score compared to images with striae alba. This is most likely due to a higher colour contrast between the striae and the surrounding healthy skin.

Table 3.2. Number of striae-affected samples in each C-Cube visual score category

Averaged score	Description	No. of samples
0	no visible striae	6
0.5		4
1	barely perceptible striae	32
1.5		8
2	visible striae	16
2.5		3
3	clearly visible striae with evidence of deep furrows	6

3.3.1 Statistical analysis

The result of the image processing steps described above yields a 200×200-pixel enface image and brightness histogram of the average tissue birefringence. A number of metrics were used to determine the best method of describing striae severity including: the arithmetic mean of the birefringence values, the median average and the arithmetic mean of the 75^{th} and 90^{th} percentiles. All analyses were carried out using MATLAB (2019a, MATLAB).

Using an unpaired two-sampled *t*-test, we aim to determine if the distribution of the means, defined in these 4 ways, are statistically different between striae-affected datasets (n=75) and the visually normal datasets (n=75). Table 3.3 shows the *p*-value of the tests for the four types of mean. The *p*-value is less than 0.05 for all of the metrics used. Thus, we can reject the null hypothesis at the 5% significance level and conclude that the SD datasets show significantly different tissue birefringence values compared to the visually normal datasets.

The tests show that the tissue birefringence values show a greater standard deviation for the striae datasets compared to the visually normal datasets, indicating greater variation in tissue birefringence of striae skin compared to visually normal skin. Among the different metrics used, the 90th percentile values show the greatest standard deviation for striae datasets. This suggests that it is the best candidate for differentiating striae severity based on the metrics considered here.

However, these differences are not large enough to place an unknown sample into either a striae or visually normal category with high accuracy. One reason for this may be because the visually normal samples were collected from a location that is adjacent to the striae samples. There is a possibility that the healthy samples also contain striae albeit with a lower severity. For a more conclusive verdict, more data is needed from a control group of healthy volunteers with no presentations of striae anywhere on the body. This would give us a benchmark for which to determine the healthy range of tissue birefringence measured using the PS-OCT.

Table 3.3. Results of *t*-test for various tissue birefringence metrics.

Metric	***p*-value of *t*-test**	**Mean and standard deviation of datasets**	
		Striae	**Visually normal**
Mean	4×10^{-6}	$6.5\pm1.7\times10^{-4}$	$5.4\pm0.9\times10^{-4}$
Median	3×10^{-6}	$6.1\pm1.2\times10^{-4}$	$5.4\pm0.9\times10^{-4}$
75th percentile	48×10^{-6}	$7.5\pm1.9\times10^{-4}$	$6.3\pm1.0\times10^{-4}$
90th percentile	3×10^{-6}	$9.2\pm3.5\times10^{-4}$	$7.3\pm1.0\times10^{-4}$

These metrics were calculated for each dataset, plotted against the corresponding C-Cube score and the coefficient of determination (R^2) was calculated. Fig. 3.10 plots the different tissue birefringence metrics calculated for each enface image against the C-Cube visual scores. There is greater variation of tissue birefringence values in samples with higher visual scores compared to those with lower scores. A regression line was fitted to the plots. Table

3.4 shows the coefficient of determination (R^2) for the metrics used. All have similar R^2 values, indicating a weak correlation between the visual scores and the tissue birefringence. No one metric is markedly better than the other in terms of their correlation with the C-Cube scores. A reason for the low R^2 value could be that the data is heavily skewed towards the lower visual scores; almost half of all striae samples have a visual score of 1. The weak correlation might suggest that PS-OCT is detecting complimentary information to visible-light dermoscopy.

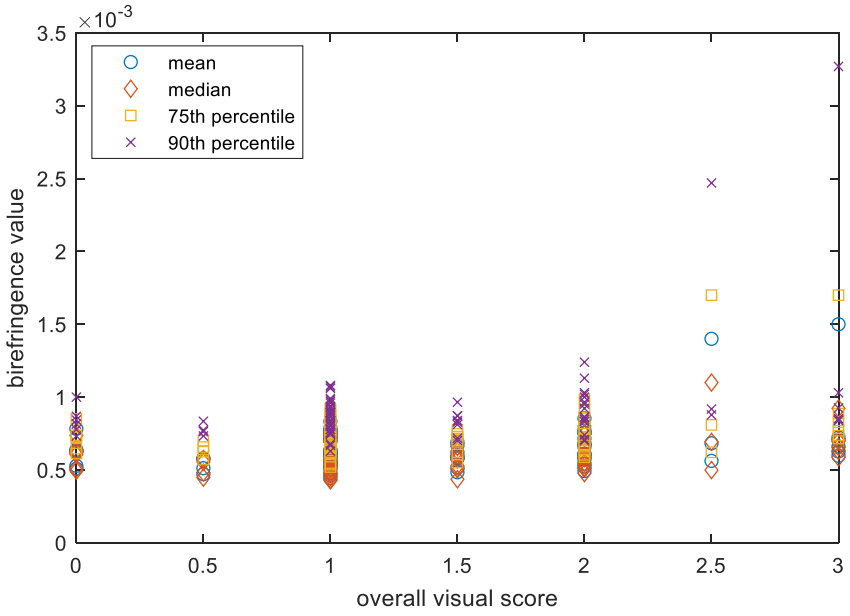

Fig. 3.10. Graph comparing the correlation between each of the four tissue birefringence metrics (mean, median 75th and 90th percentile) against the corresponding C-Cube scores. These metrics were calculated for each tissue birefringence image (each open circle of a particular colour represents a given metric for a particular image) in order to determine whether a reliable birefringence-based metric can be used to represent striae severity. A linear regression line was calculated for each metric and the coefficient of determination was calculated. All show a weak correlation between the tissue birefringence scores and C-Cube scores, as indicated by Table 3.4.

Table 3.4. Coefficient of determination for difference metrics used to represent striae severity.

Metric	**Gradient of linear regression**	**Coefficient of determination (R^2)**
Mean	7.1×10^{-5}	0.11
Median	4.2×10^{-5}	0.08
75th percentile	8.4×10^{-5}	0.12
90th percentile	15.7×10^{-5}	0.12

A higher tissue birefringence value is expected for SA compared to SR, as a key feature of SA is the presence of densely packed collagen fibers that run parallel to the surface of the skin [7]. However, as we only have 11 samples of SR compared to 60 samples for SA, it is not possible to determine whether this is true, with high statistical confidence. More samples for SR are needed. Furthermore, different patients may exhibit different tissue birefringence values due to differences in striae severity, genetics, etc. A larger sample size is needed to conclude whether tissue birefringence differs significantly between SR and SA.

3.4 Conclusions

To the best of our knowledge, this is the first exploratory study comparing visible-light dermoscopy with enface PS-OCT tissue birefringence imaging to assess the severity of striae distensae, in a clinically useful cohort size (150 measurement sites in 19 volunteers). Measuring the severity of striae would be useful, for example in assessing the effectiveness of treatment options and has, thus far, been done mostly by subjective visual scoring. The C-Cube camera captures images under fixed lighting conditions which are then given a visual score. We attempt in this paper to compare this method of scoring to quantified tissue birefringence metrics obtained using a PS-OCT system. It is hypothesized that the PS-OCT, with its ability to measure the sub-surface local birefringence of tissues, will provide score that is more reflective of the underlying physiology of striae.

Our data demonstrates that there is a statistically significant difference between visually normal skin and striae-affected skin. Using enface images of tissue birefringence, the striae samples are shown to have a higher mean, median, 75^{th} and 90^{th} percentile values in comparison to the visually normal samples. The 90^{th} percentile value seems to have a larger

standard deviation among striae samples compared to the other metrics, suggesting that it is the best metric for differentiating SD severity. There seems to be a loose correlation between the tissue birefringence percentile scores and the C-Cube scores.

PS-OCT may thus show promise as a method for assessing striae severity, either alone or in combination with other modalities, but more studies are needed before it meets the requirements of a gold standard. Further potential investigations include collecting data on a control group of healthy volunteers and improving image processing techniques by increasing the 2D averaging pool size.

Recent developments in PS-OCT, such as Jones matrix PS-OCT systems [30], could give more insights into the spatial variation of local birefringence and optic axis that characterize SD. We are actively pursuing these new developments in our lab. A similar study investigating the local birefringence of human burn scars using Jones matrix OCT has successfully shown the efficacy of this technique [31]. Quantifying the spatial variation in Stokes vectors due to multiple scattering [32], modifying the scanning probe to include fiducial markers and the use of vascular masking techniques to aid in artefact removal [33] are also potentially useful avenues to explore.

As corticosteroid usage is a risk factor for SD [4], we are also developing PS-OCT in combination with structural and angiographic OCT to compare the effect of topical corticosteroids and new treatments for atopic dermatitis on the epidermis and dermis.

References

[1] W.C. Lin, R.A. Byers, W. Li, S.G. Danby, M.J. Cork, and S.J. Matcher, “Imaging striae distensae: a comparison between PS-OCT and digital dermoscopy,” Biomed. Opt. Express **12**(6), 3296-3311 (2021).

[2] S. Ud-Din, D. McGeorge, and A. Bayat, “Topical management of striae distensae (stretch marks): Prevention and therapy of striae rubrae and albae,” J. Eur. Acad. Dermtol. Venereol. **30**(2), 211-222 (2016).

[3] S. Shuster, “The cause of striae distensae,” Acta Derm. Venereol. Suppl. **59**(85), 161 (1979).

[4] S. Cho, E. S. Park, D. H. Lee, K. Li, and J. H. Chung, “Clinical features and risk factors for striae distensae in Korean adolescents”, J. Eur. Acad. Dermatol. Venereol. **20**(9), 1108-1113 (2006).

[5] R. C. T. Cordeiro, K. G. Zecchin, and A. M. de Moraes, “Expression of estrogen, androgen, and glucocorticoid receptors in recent striae distensae,” Int. J. Dermatol. **49**(1), 30–32 (2010).

[6] K. S. Lee, Y. J. Rho, S. I. Jang, M. H. Suh, and J. Y. Song, “Decreased expression of collagen and fibronectin genes in striae distensae tissue,” Clin. Exp. Dermatol. **19**(4), 285–288 (1994).

[7] A. Hague, and A. Bayat, “Therapeutic targets in the management of striae distensae: A systematic review,” J. Am. Acad. Dermatol. **77**(3), 559-568 (2017).

[8] K. Yamaguchi, N. Suganuma, and K. Ohashi, “Quality of life evaluation in Japanese pregnant women with striae gravidarum: a cross-sectional study,” BMC Res. Notes **5**(1), 450 (2012).

[9] C. Cho, E. Cho, N. Kim, J. Shin, S. Woo, J. Lee, J. Lee, E. Lee, and J. Ha, "Biophysical properties of striae rubra and striae alba in human skin: Comparison with normal skin," Skin Res. Technol. **25**(3), 283-288 (2019).

[10] O. Rangel, I. Arias, E. García, and S. Lopez-Padilla, “Topical tretinoin 0.1% for pregnancy-related abdominal striae: an open-label, multicenter, prospective study,” Adv. Ther. **18**(4), 181-186 (2001).

[11] D. Hexsel, M. Soirefmann, M. D. Porto, J. Schilling-Souza, C. Siega, and T. Dal'Forno, “Superficial dermabrasion versus topical tretinoin on early striae distensae: a randomized, pilot study,” Dermatol. Surg. **40**(5), 537-544 (2014).

[12] P. Deprez, “Easy Peel for the Treatment of Stretch Marks,” Int. J. Cosmet. Surg. Aesthet. Dermatol. **2**(3), 201-204 (2002).

[13] S. Bitencourt, A. Lunardelli, R. H. Amaral, H. B. Dias, E. S. Boschi, and J. R. de Oliveira, “Safety and patient subjective efficacy of using galvanopuncture for the treatment of striae distensae,” J. Cosmet Dermatol. **15**(4), 393-398 (2016).

[14] A. S. Aldahan, V. V. Shah, S. Mlacker, S. Samarkandy, M. Alsaidan, and K Nouri, “Laser and light treatments for striae distensae: a comprehensive review of the literature,” Am. J. Clin. Dermatol. **17**(3), 239-256 (2016).

[15] M. Bleve, P. Capra, F. Pavanetto, and P. Perugini, “Ultrasound and 3D skin imaging: Methods to evaluate efficacy of striae distensae treatment,” Dermatol. Res. Pract. **2012**, (2012).

[16] D. Huang, E. A. Swanson, C. P. Lin, J. S. Schuman, W. G. Stinson, W. Chang, M. R. Hee, T. Flotte, K. Gregory, and C. A. Puliafito, “Optical Coherence Tomography,” Sci. New Ser. **254**(5035), 1178–1181 (1991).

[17] M. C. Pierce, J. Strasswimmer, B. H. Park, B. Cense, and J. F. De Boer, “Advances in Optical Coherence Tomography Imaging for Dermatology,” J. Invest. Dermatol. **123**(3), 458-463 (2004).

[18] M. R. Hee, E. A. Swanson, J. G. Fujimoto, and D. Huang, “Polarization-sensitive low-coherence reflectometer for birefringence characterization and ranging,” J. Opt. Soc. Am. B **9**(6), 903-908 (1992).

[19] M. J. Everett, K. Schoenenberger, B. W. Colston, and L. B. Da Silva, “Birefringence characterization of biological tissue by use of optical coherence tomography,” Opt. Lett. **23**(3), 228-230 (1998).

[20] C. Hitzenberger, E. Goetzinger, M. Sticker, M. Pircher, and A. Fercher, “Measurement and imaging of birefringence and optic axis orientation by phase resolved polarization sensitive optical coherence tomography,” Opt. Express **9**(13), 780-790 (2001).

[21] M. Pircher, C. K. Hitzenberger, and U. Schmidt-Erfurth, “Polarization sensitive optical coherence tomography in the human eye,” Prog. Retin. Eye Res. **30**(6), 431–451 (2011).

[22] J. Walther, J. Golde, L. Kirsten, F. Tetschke, F. Hempel, T. Rosenauer, C. Hannig, and E. Koch, “In vivo imaging of human oral hard and soft tissues by polarization-sensitive optical coherence tomography,” J. Biomed. Opt. **22**(12), 121717 (2017).

[23] B. Baumann, “Polarization Sensitive Optical Coherence Tomography: A Review of Technology and Applications,” Appl. Sci. **7**(5), 474 (2017).

[24] M. K. Al-Qaisi, and T. Akkin, “Polarization-sensitive optical coherence tomography based on polarization-maintaining fibers and frequency multiplexing,” Opt. Express **16**(17), 13032–13041 (2008).

[25] Z. Lu, D. Kasaragod, and S. J. Matcher, “Conical scan polarization-sensitive optical coherence tomography,” Biomed. Opt. Express **5**(3), 752–762 (2014).

[26] R. Byers, and S. Matcher, “Attenuation of stripe artifacts in optical coherence tomography images through wavelet-FFT filtering,” Biomed. Opt. Express **10**(8), 4179-4189 (2019).

[27] E. Götzinger, M. Pircher, W. Geitzenauer, C. Ahlers, B. Baumann, S. Michels, U. Schmidt-Erfurth, and C. K. Hitzenberger, "Retinal pigment epithelium segmentation by polarization sensitive optical coherence tomography," Opt. Express **16**(21), 16410-16422 (2008).

[28] L. Chin, X. Yang, R. A. McLaughlin, P. B. Noble, and D. D. Sampson, "En face parametric imaging of tissue birefringence using polarization-sensitive optical coherence tomography," J. Biomed. Opt. **18**(6), 066005 (2013).

[29] P. Zheng, R.M. Lavker, and A.M. Kligman, “Anatomy of striae,” Br. J. Dermatol. **112**(2), 185-193 (1985).

[30] S. Makita, M. Yamanari, and Y. Yasuno, "Generalized Jones matrix optical coherence tomography: performance and local birefringence imaging," Opt. Express **18**, 854-876 (2010).

[31] M. E. H. Jaspers, F. Feroldi, M. Vlig, J. F. de Boer, and P. P. M. van Zuijlen, "In vivo polarization-sensitive optical coherence tomography of human burn scars: birefringence quantification and correspondence with histologically determined collagen density," J. Biomed. Opt. **22**(12), 121712 (2017).

[32] S. G. Adie, T. R. Hillman, and D. D. Sampson, "Detection of multiple scattering in optical coherence tomography using the spatial distribution of Stokes vectors," Opt. Express **15**, 18033-18049 (2007).

[33] P. Gong, L. Chin, S. Es’haghian, Y. M. Liew, F. M. Wood, D. D. Sampson, and R. A. McLaughlin, "Imaging of skin birefringence for human scar assessment using polarization-sensitive optical coherence tomography aided by vascular masking," J. Biomed. Opt. **19**(12), 126014 (2014).

Chapter 4: Monitoring Dental Erosion

4.1 Introduction

Dental erosion is the loss of enamel on a tooth surface, caused by persistent, non-bacterial acidic attack upon the tooth surface [1]. A tooth has three major components: pulp, dentine and enamel. The pulp is the centre of the tooth and contains nerves and blood vessels. Surrounding the pulp is the dentine, which protects the pulp and gives the tooth its structure. Lastly, the enamel is the hard inorganic outer shell of a tooth, which protects the organic dentine and pulp underneath. It is mainly composed of parallel rows of enamel rods, which lie perpendicular to the dentine surface. The enamel rods are made up of hydroxyapatite crystals. An acidic environment (pH<5.5) causes the hydroxyapatite crystals to dissolve or demineralise, which results in the erosion and shortening of the enamel rods [2]. Causes of dental erosion vary and include gastroesophageal reflux disease, environmental sources and diet [3].

The use of OCT in dental erosion was first attempted by Wilder-Smith et al. to quantify tooth demineralisation and enamel loss by measuring enamel thickness and reflectivity [4]. OCT was used in a randomized double-blind study to investigate whether esomeprazole could reduce the rate of dental erosion in patients with gastroesophageal reflux disease. Tooth demineralisation was shown to result in an increase in reflectivity.

The most common method of monitoring dental erosion using OCT is to measure the enamel thickness [5]. When measuring enamel thickness, a reference layer is needed to monitor the

effects before and after acid challenge. This is typically done by either using the dentine-enamel junction (DEJ) or creating an acid-resistant reference layer on the tooth surface using laser irradiation [5-7]. It is difficult to resolve the DEJ, as the DEJ has an uneven scallop shape and the optical reflectivity of the enamel surface increases after acid treatment [5]. Moreover, the substantial reduction in enamel thickness measured (30-100 µm) do not reflect *in vivo* environmental conditions [4]. Thus, measuring enamel thickness is not the most reliable indicator of dental erosion *in vivo*.

Recently, de Moraes et al. showed that teeth pre-treated with fluoride showed promising results for preventing dentine loss [8]. Despite different toothpaste formulations and methods of application, it has been shown that fluoride toothpastes containing stannous fluoride aid in preventing dental erosion [9]. Furthermore, casein phosphopeptide-amorphous calcium phosphate (CPP-ACP) has also been proposed to prevent dental erosion with a similar mechanism of action to stannous fluoride [10]. However, studies investigating its effectiveness have been contradictory [11-14], with decreasing effectiveness when experimental conditions more closely mimic clinical conditions.

This study investigates whether treating teeth with stannous-containing fluoride toothpaste or tooth mousse with CPP-ACP before acid challenge helps to protect against dental erosion. When teeth undergo dental erosion, they become more porous and the tooth enamel would have a more uneven surface. This is because the dissolution of hydroxyapatite does not occur uniformly on the surface of enamel, resulting in pits forming on the enamel surface. The uneven surface of acid-eroded enamel has been previously imaged using confocal laser scanning microscopy [15]. This allows more light be reflected at the air-enamel interface and the reflectivity is expected to increase. Teeth that have a layer of stannous-containing fluoride

toothpaste or tooth mousse applied before treatment should have a lower increase in reflectivity. Based on past literature, toothpaste should be more effective at preventing dental erosion compared to tooth mousse and hence, should have the lowest increase in reflectivity.

4.2 Materials & Methods

4.2.1 Treatment of teeth with acid

21 human teeth, of varying ages and types, are randomly divided into 3 groups, each undergoing different pre-treatments prior to acid challenge. The first group is the control. The second group is covered with a layer of stannous-containing fluoride toothpaste (Oral-B Pro-expert) for 2 minutes. The third group is covered with a layer of tooth mousse containing CPP-ACP (GC tooth mousse) for 5 minutes.

After pre-treatment, all teeth are treated with acid using the following procedure. Firstly, any toothpaste or tooth mousse is washed off using running tap water. The teeth are stored in tap water for an hour before immersion in apple juice with continuous stirring for 20 minutes. Apple juice contains citric and malic acid and has a pH of around 3. The teeth are then removed from the apple juice and washed under running tap water. They are stored in tap water for later use.

A single treatment cycle consists of one round of pre-treatment and immersion in apple juice. The teeth undergo 14 cycles in total, twice daily for 7 days.

4.2.2 OCT imaging

Prior to pre-treatment, each tooth is varnished with acid resistant nail polish (Revlon red nail polish), as shown by Fig. 4.1. The blue line shows the specific B-scan that is being imaged. This is to ensure that the same slice is imaged before and after acid challenge, because teeth do not erode uniformly. The swept-source PS-OCT system was used to obtain B-scans for each tooth before and after acid challenge. Details and specifications of the OCT system used can be found in Ch 3.2.3. While the PS-OCT system is capable of collecting information on the phase retardance of the sample, it is used here only for imaging tissue reflectivity. The B-scan obtained is a cross-section covering an area of 4mm × 2mm.

Fig. 4.1. Photograph of a sample tooth being imaged using the PS-OCT. Red nail varnish was used to delineate the specific B-scan slice to be imaged (blue line). [16]

4.2.3 Image processing

Fig. 4.2 (top) shows an original B-scan of a sample tooth without any image processing. This particular sample is from the tooth mousse group after treatment. The curved surface of the

tooth, as well as the nail varnish on either side, are clearly visible. The unvarnished tooth enamel has a lower intensity in comparison with the highly reflective nail varnish. The nail varnish is seen as the bright layer on the left and right sides of the blue box. The B-scan contains horizontal stripe artefacts as well as reverberation artefacts. The highly scattering varnish layer show especially strong reverberation artefacts. The artefacts are mostly likely caused by reflections between the fibre connectors within the fibre optic components of the system. The image is first cropped to exclude the nail varnish (blue box). The crack present within the tooth (red arrow) is also cropped out.

For each B-scan, the tooth surface without the nail varnish was straightened using an algorithm developed by Byers and Matcher [17]. A wavelet-FFT filtering algorithm was also used to reduce ghost artefacts in the image [17]. The resulting filtered structural image is shown in Fig. 4.2 (bottom-left). The average reflectivity profile was obtained by taking the arithmetic mean of the reflectivity profiles across the surface of the tooth (Fig. 4.2 bottom-right).

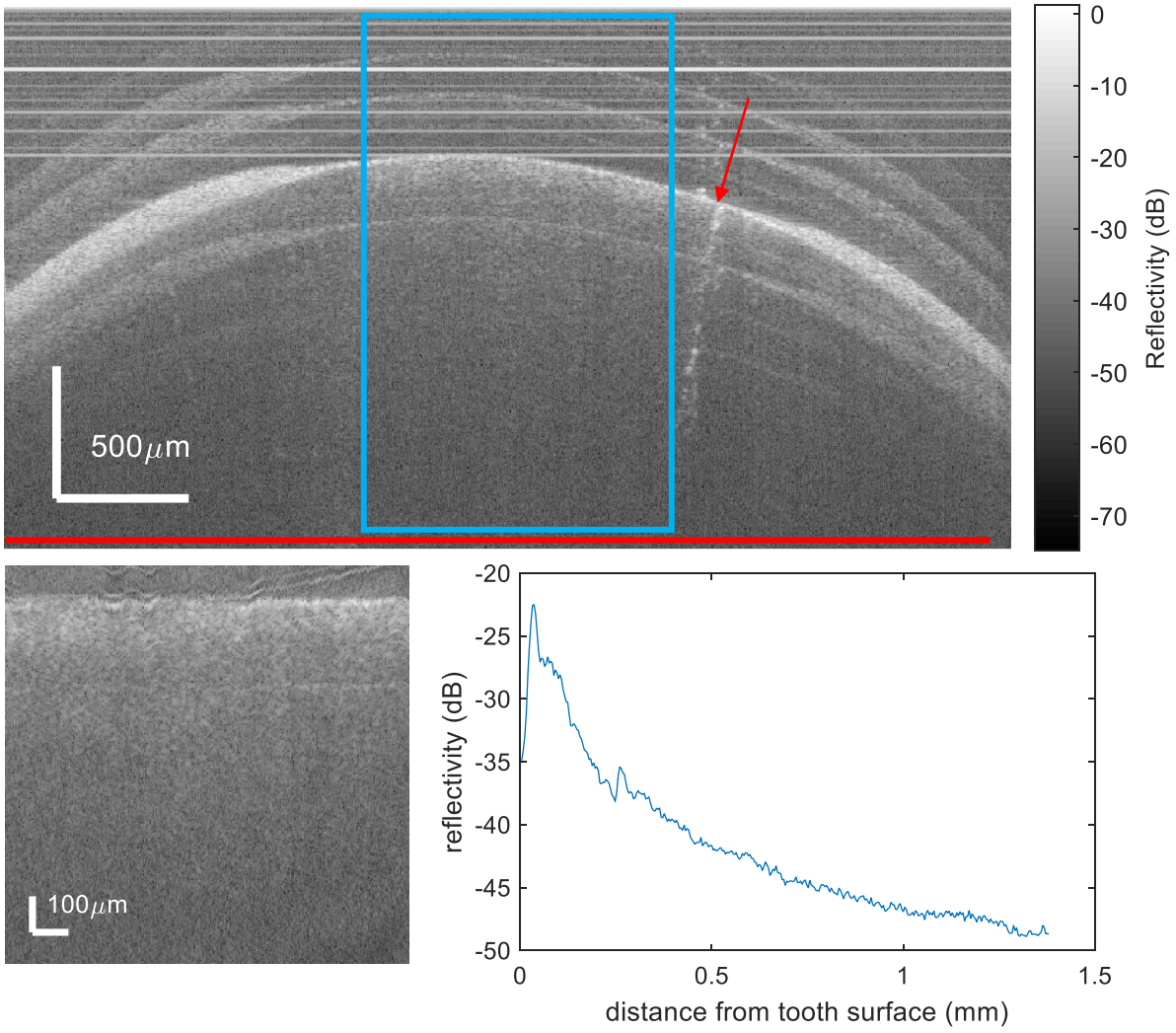

Fig. 4.2. Images of a sample structural image after image processing. This particular sample is from the tooth mousse group after acid treatment. Top: Original structural image, showing the exposed enamel and nail varnish. The image is cropped to within the blue box. The crack present within the tooth (red arrow) is also cropped out. Bottom-left: Structural image after applying a wavelet-filtering algorithm to straighten the image and reduce artefacts. Bottom-right: Reflectivity profile, obtained by taking the arithmetic mean across the tooth surface.

We tried out two methods for quantifying tooth demineralization. Firstly, the peak reflectivity is found by taking the absolute reflectivity at the tooth surface and subtracting the noise floor. The absolute reflectivity is found by taking the peak reflectivity of the reflectivity profile. The noise floor is calculated by taking the arithmetic mean of the last row of pixels in the B-scan (red line in Fig. 4.2 top). Secondly, the initial slope of the reflectivity profile is calculated. This is done by finding the slope from the initial peak to a depth of 0.2 mm. All image processing steps were done in MATLAB (MATLAB, R2019a).

4.3 Results

4.3.1 Structural image

Fig. 4.3 shows the structural images of a sample teeth in all three groups before (left) and after (right) treatment. The intensity of the tooth enamel surface has increased slightly after treatment. The lack of strong visual differences between the before and after images indicates the importance of analysing the reflectivity profile instead of relying solely on the structural images.

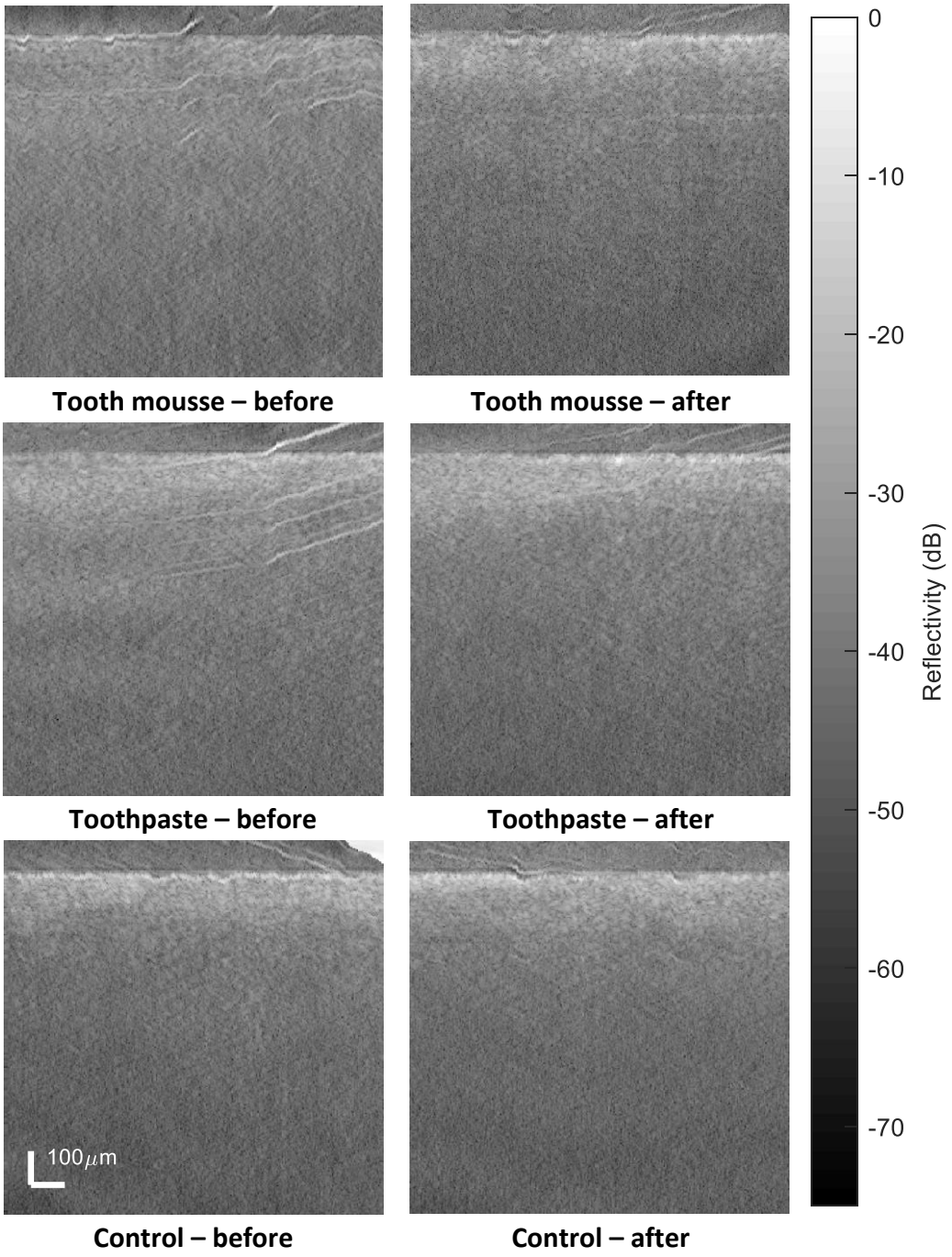

Fig. 4.3. Structural images of teeth before (left) and after (right) treatment. All images have been cropped, straightened and filtered. Samples are from the tooth mousse group (top), toothpaste group (centre) and control group (bottom).

4.3.2 Reflectivity profile

The tooth surface of each B-scan is straightened and an average reflectivity profile is obtained. Fig. 4.4 shows the reflectivity profile of a sample tooth from the tooth in Fig. 4.2 before and after treatment. Peak reflectivity increases from 21dB above the noise floor to 26dB. The

slope of the reflectivity profile, calculated from the initial peak to a depth of 0.2 mm, is steeper after treatment, decreasing from -23 dB/mm to -69 dB/mm. The steeper profile indicates that more light is being attenuated near the surface of the tooth due to demineralisation of the enamel. The peak present at 0.25mm for the reflectivity profile after treatment is due to a ghost artefact and does not correspond to any morphological features within the tooth. The DEJ shows up as a slight increase in reflectivity at 1 mm in the reflectivity profile before treatment, but is not visible after treatment. As more light is being reflected at the enamel surface, less light is able to penetrate to reach the DEJ.

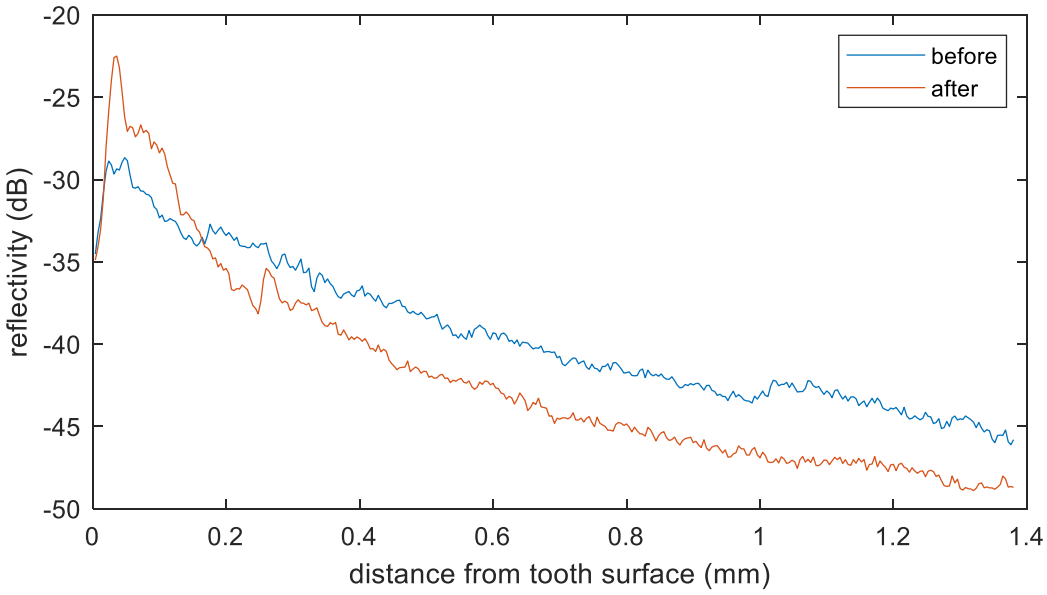

Fig. 4.4. Reflectivity profile of a sample tooth in the tooth mousse group before and after treatment. The peak reflectivity above noise floor is 20.8 dB before treatment and increases to 26.0 dB after treatment. The slope of the reflectivity profile, calculated from the initial peak to a depth of 0.2 mm, decreased from -23 dB/mm to -69 dB/mm.

4.3.3 Statistics

Fig. 4.5 shows the change in peak reflectivity against the initial peak reflectivity readings before treatment. For the most part, the graph shows that the peak reflectivity increases after treatment. This fits with the hypothesis that acid erosion leads to the demineralization of

tooth enamel, leading to higher backscatter at the tooth surface and hence, an increase in peak reflectivity above the noise floor.

A higher initial reflectivity reading correlates with a lower change in reflectivity after treatment. A simple linear regression has been used to fit the data in Fig. 4.5. The Pearson correlation coefficient is -0.78 with a *p*-value of 3.3e-5, suggesting that the change in peak reflectivity has a significant negative correlation with the initial peak reflectivity. The change in reflectivity is unlikely to be due to the effect of tooth mousse or toothpaste, but rather a result of the initial reflectivity present. Before treatment, it is thus important to ensure that teeth in each group have an even distribution of initial reflectivity measurements. If not, the subsequent changes in peak reflectivity could be a result of differences in the distribution of teeth of different initial peak reflectivity, leading to inaccurate results.

As this was a preliminary study, we were unaware that the initial peak reflectivity would play a significant role in the changes after treatment and this was reflected in the results obtained. Although teeth were randomly selected for the different treatment regimes, teeth in the toothpaste group had the narrowest range of initial reflectivity readings of 23-30dB. In contrast, teeth in the control group had the largest range, with initial reflectivity readings from 20dB to 36dB. Assuming the change in peak reflectivity is proportional to the initial reflectivity, as shown in Fig. 4.5, the change in reflectivity for the toothpaste and control group would have the narrowest and largest range respectively. This is demonstrated by their respective standard deviations, where the toothpaste and control groups had the lowest and highest standard deviation. The mean change in reflectivity for the control, tooth mousse and toothpaste groups were +1.0 ±6.0 dB, +3.1 ±3.2 dB and +2.1 ±1.9 dB respectively.

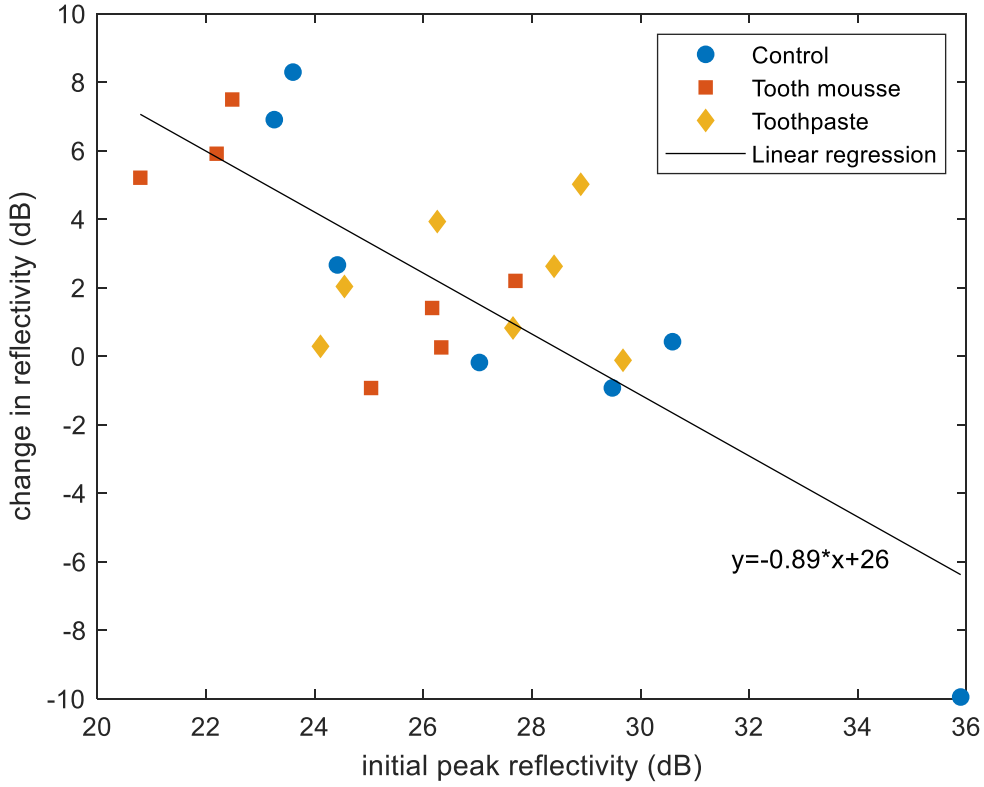

Fig. 4.5. Change in peak reflectivity against initial peak reflectivity measurement. There is a negative correlation between initial peak reflectivity and the change in reflectivity after treatment. Teeth with lower initial peak reflectivity tend to have a higher change in peak reflectivity after treatment.

The second method of quantifying the extent of tooth demineralisation involves the calculation of the slope of the reflectivity profile, from the initial peak to a depth of 0.2mm. A depth of 0.2mm was used because a ghost artefact was present at a depth of 0.25mm, which would affect slope calculations.

Fig. 4.6. shows the change in slope plotted against the initial slope, with a simple linear regression used to calculate the line of best fit. Similar to the results obtained in Fig. 4.5, a steeper initial slope leads to a smaller change in slope after acid treatment. The control group also has the greatest range in initial slope values, whereas the toothpaste group has the narrowest range. The Pearson correlation coefficient is -0.88 with a *p*-value of 1.4e-7. This is significantly higher than the correlation coefficient obtained using peak reflectivity as a

metric, and this is reflected in the graph. It is visibly easier to see that there is a negative correlation between the change in slope and the initial slope.

Between the two metrics used, calculating the slope seems to be a more reliable indicator of the extent of acid erosion compared to using peak reflectivity. This makes sense, as the slope is calculated using a greater number of data points over a distance of 0.2mm and uses relative, not absolute, reflectivity measurements. In contrast, the peak reflectivity is a single data point, which may be affected by the position of the tooth within the imaging area and the noise levels.

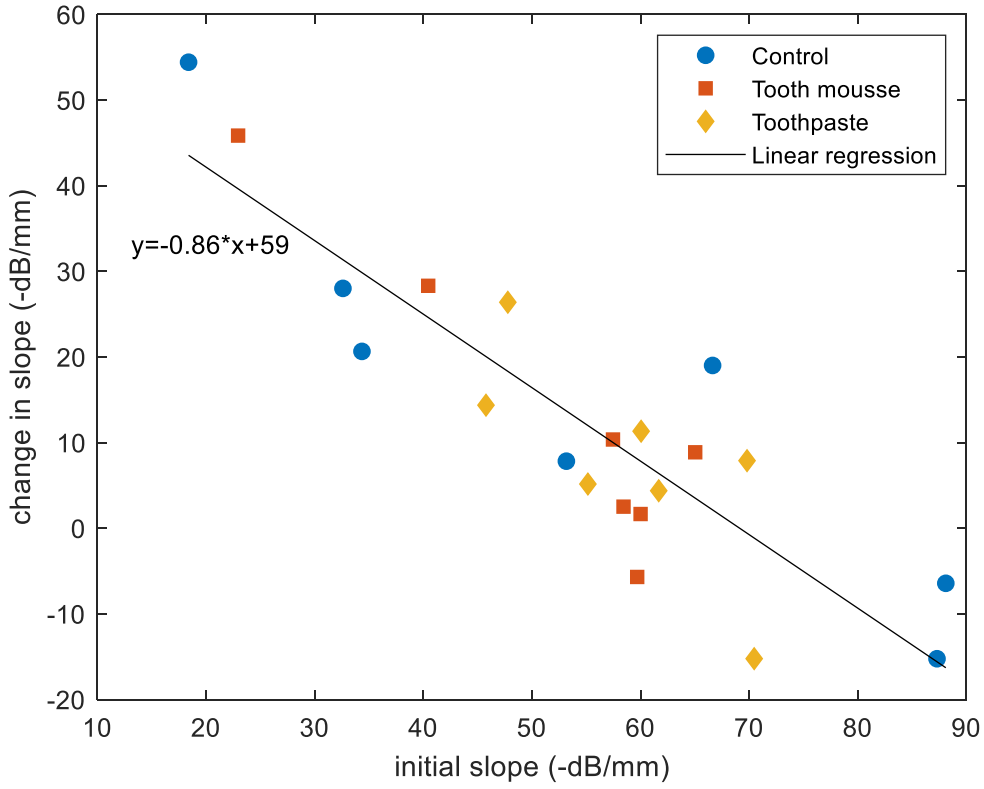

Fig. 4.6. Change in slope of reflectivity against initial slope. The mean change in slope for the control, tooth mousse and toothpaste groups are -16 ±23 dB/mm, -13 ±18 dB/mm and -8 ±13 dB/mm respectively.

4.4 Discussion & Conclusions

Previous studies using OCT to measure the effects of acid erosion used highly acidic treatment regimes that caused rapid erosion of tooth enamel [4-8]. This led to the visible loss of tooth enamel in the structural images and quantification methods focussed on measuring the distance from the tooth surface to the DEJ [4,5] or the deformation of the tooth enamel [6-8]. The treatment regime used in this study is less challenging on the tooth surface in order to more closely mimic *in vivo* conditions. It is important to note the differences in this treatment regime compared to actual *in vivo* conditions. Firstly, the abrasive effect of brushing one's teeth for example would lead to a faster erosion rate. Secondly, saliva acts as a buffer to limit changes in pH when teeth encounter a strong acid or alkali, which would slow down the erosion rate. Regardless of these differences, the treatment regime here is weaker than those used in previous studies. There would not be visible signs of dental erosion and so we would need a different method of quantifying tooth demineralisation. We were able to use the tooth surface reflectivity as a measure of demineralisation. This was used to measure whether any preventative effects can be achieved from stannous-containing fluoride toothpaste or tooth mousse with CPP-ACP.

Two methods of quantifying tooth demineralisation were used: peak reflectivity readings and calculation of the slope of the reflectivity profile. Calculating the slope seems to be a more reliable method, as there is a greater correlation between the initial readings and the change in readings. Regardless of the quantification method used, the results show that peak reflectivity and slope before treatment is an important factor in determining the magnitude of reflectivity changes after treatment. Thus, for comparison purposes, it is important that teeth assigned to different groups have similar distribution of initial reflectivity readings. In

the toothpaste group, teeth displayed higher initial measurements on average compared to the control and tooth mousse group. Thus, the lower mean reflectivity change for the toothpaste group is a result of the higher initial readings rather than the effect of pre-treatment with toothpaste. Thus, it is not possible to draw any conclusions regarding the effect of tooth mousse with CPP-ACP or stannous-containing fluoride toothpaste on dental erosion.

There are several limitations to this study. The sample size of 21 (7 per group) is too small to draw strong conclusions about the effect of toothpaste and tooth mousse on dental erosion. It is not known whether the age and type of tooth affects the results. Furthermore, this is an *in vitro* study; more studies are necessary to determine whether teeth display similar results *in vivo*. It was not initially known that reflectivity measurements before treatment correlate with reflectivity changes. This means that the preventative effect of stannous-containing fluoride toothpaste on dental erosion are inconclusive.

Possible future work includes comparing the sensitivity of OCT to previous methods such as profilometry and surface hardness measurements. It would also be interesting to use ANOVA (analysis of variance) techniques to examine whether, for example, the initial slope is the strongest predictor of change in slope.

References

[1] E. O'Sullivan and A. Milosevic, "UK National Clinical Guidelines in Paediatric Dentistry: diagnosis, prevention and management of dental erosion," Int. J. Paediatr. Dent. **18**, 29–38 (2008).

[2] O. Fejerskov, B. Nyvad, E.A. Kidd, "Dental caries: The disease and its clinical management," Oxford, Blackwell Munksgaard **2**, 20-48 (2008).

[3] A. C. Sosa, J. M. Solis, N. Cruz-Fierro, S. López, and S. Nakagoshi, "Dental Erosion: Causes, diagnostics and treatment.," J. Oral Res. **3**(4), 257–261 (2014).

[4] C. H. Wilder-Smith, P. Wilder-Smith, H. Kawakami-Wong, J. Voronets, K. Osann, and A. Lussi, "Quantification of Dental Erosions in Patients With GERD Using Optical Coherence Tomography Before and After Double-Blind, Randomized Treatment With Esomeprazole or Placebo," Am. J. Gastroenterol. **104**(11), 2788–2795 (2009).

[5] K. H. Chan, A. C. Chan, C. L. Darling, and D. Fried, "Methods for monitoring erosion using optical coherence tomography," Lasers in Dentistry XIX, International Society for Optics and Photonics **8566**, 856606 (2013).

[6] K. H. Chan, H. Tom, and D. Fried, "Monitoring the inhibition of erosion by a CO laser with OCT," Lasers in Dentistry XX, International Society for Optics and Photonics **8929**, 89290F (2014).

[7] K. H. Chan, H. Tom, C. L. Darling, and D. Fried, "A method for monitoring enamel erosion using laser irradiated surfaces and optical coherence tomography," Lasers Surg. Med. **46**(9), 672–678 (2014).

[8] M. C. D. de Moraes, A. Z. Freitas, and A. C. C. Aranha, "Progression of erosive lesions after Nd:YAG laser and fluoride using optical coherence tomography," Lasers Med. Sci. **32**(1), 1–8 (2017).

[9] M. C. Huysmans, A. Young, and C. Ganss, "The role of fluoride in erosion therapy," Erosive Tooth Wear, Karger Publishers **25**, 230-243 (2014).

[10] M. A. R. Buzalaf, A. C. Magalhães, and A. Wiegand, "Alternatives to fluoride in the prevention and treatment of dental erosion," Erosive Tooth Wear, Karger Publishers **25**, 244-252 (2014).

[11] X. Wang, B. Megert, E. Hellwig, K. W. Neuhaus, and A. Lussi, "Preventing erosion with novel agents," J. Dent. **39**(2), 163–170 (2011).

[12] A. Wiegand and T. Attin, "Randomised in situ trial on the effect of milk and CPP-ACP on dental erosion," J. Dent. **42**(9), 1210–1215 (2014).

[13] S. Ranjitkar, J. A. Kaidonis, L. C. Richards, and G. C. Townsend, "The effect of CPP–ACP on enamel wear under severe erosive conditions," Arch. Oral Biol. **54**(6), 527–532 (2009).

[14] S. Ranjitkar, J. M. Rodriguez, J. A. Kaidonis, L. C. Richards, G. C. Townsend, and D. W. Bartlett, “The effect of casein phosphopeptide–amorphous calcium phosphate on erosive enamel and dentine wear by toothbrush abrasion,” J. Dent. **37**(4), 250–254 (2009).

[15] A.M.A. Maia, C. Longbottom, A.S.L. Gomes, and J.M. Girkin, “Enamel erosion and prevention efficacy characterized by confocal laser scanning microscope,” Microsc. Res. Tech. **77**, 439–45 (2014).

[16] R. Kilano, “The effect of Stannous-containing fluoride toothpaste and Tooth Mousse in the prevention of dental erosion: an in-vitro study using Optical Coherence Tomography”, The University of Sheffield, 2018.

[17] R. Byers, and S. Matcher, “Attenuation of stripe artifacts in optical coherence tomography images through wavelet-FFT filtering,” Biomed. Opt. Express **10**(8), 4179-4189 (2019).

Chapter 5: Real-time Tracking of Plant Wounding Response

5.1 Introduction

When plants are wounded, such as through herbivory, they produce the volatile methyl jasmonate as a defence mechanism [1]. A precursor of this organic compound, jasmonate, accumulates in adjacent plant tissue minutes after wounding. Investigations of the mechanisms for wounded tissue signalling and subsequent accumulation of jasmonate in distal regions have revealed the enzymes involved and the role of vascular tissue [1,2]. To track jasmonate synthesis, previous studies have used electrodes and dyes to measure the electrochemical potential and transcript synthesis respectively [1]. Farmer et al. has proposed the "squeeze cell hypothesis", which claims that changes in the axial pressure in xylem vessels upon wounding lead to jasmonate synthesis through a series of mechanical and chemical pathways [2]. An intermediate pathway involves changes in radial pressure in the xylem vessels. These changes in turgor pressure within the plant are hypothesised to effect small changes in the diameter of the plant stem. OCT has been proposed as a means of measuring these changes in real time and without damaging the plant.

The investigation aims to determine the extent to which the diameter of a plant petiole can be consistently and precisely measured using OCT. If so, OCT will then be used to determine if there are any inherent fluctuations in an attached petiole diameter, in order to establish a baseline measurement of the plant in a state of equilibrium. If these experiments are successful and OCT is seen as a feasible method of measuring in vivo changes in plant petiole

diameter, the overarching goal would then be to induce a wound in the plant and the response to plant diameter over time.

5.2 Materials & Methods

5.2.1 OCT imaging of petioles

Three *Arabidopsis thaliana* specimens from separate plants were imaged using an in-house higher-resolution spectrometer-based OCT system (SD-OCT). *Arabidopsis thaliana* is a flowering plant that is commonly used as a model organism in botany. We are interested in imaging the midrib or the petiole of the plant. Fig. 5.1 is a simple diagram that shows the difference between the midrib and petiole of a plant. The petiole is the stalk that connects a leaf to the main plant stem, while the midrib is the main vein that runs through the centre of a leaf.

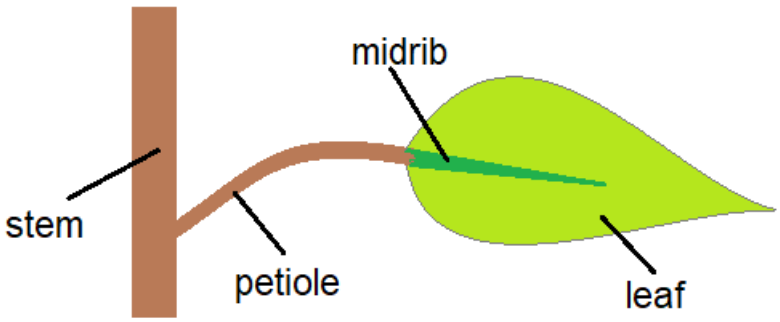

Fig. 5.1. Diagram showing different parts of a plant. The midrib and/or petiole is the region that we are interested in imaging.

Fig. 5.2 shows B-scans of the top and underside of an *Arabidopsis* rosette leaf. It is difficult to pick out the midrib due to the unevenness of the leaf surface. Hair-like structures called

trichomes, present on the top surface of the leaf (highlighted by blue circles), also make subsequent image processing difficult. Therefore, imaging the petiole is preferred.

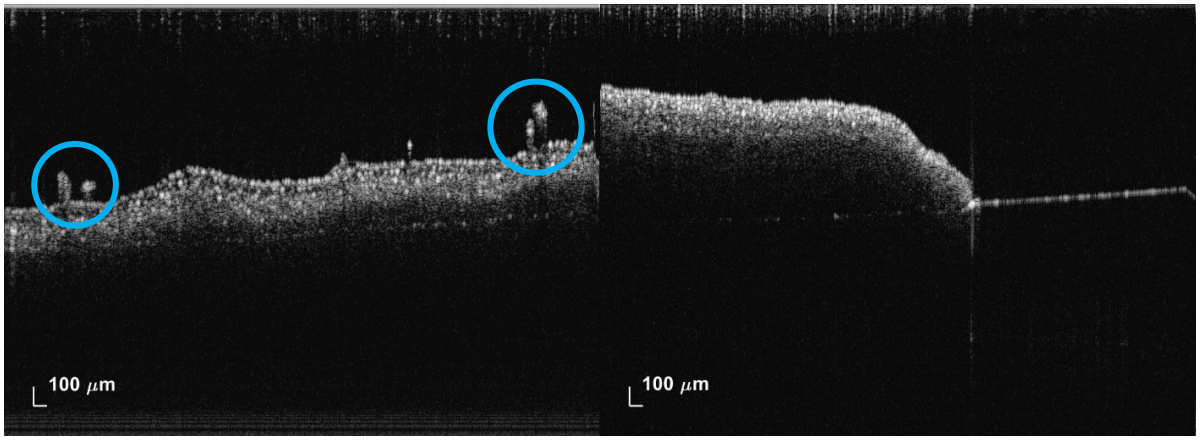

Fig. 5.2. B-scans of the top (left) and underside (right) of an Arabidopsis rosette leaf. The presence of trichomes on the top surface of the leaf (highlighted by the blue circles) and the unevenness of the leaf surface makes finding the midrib diameter during image processing difficult. Therefore, imaging the petiole is preferred.

A lightweight cover holds the leaf in place without wounding it. It also acts as a reference during image processing. Different materials were tested for the cover and 1 mm-thick opaque polycarbonate sheet was chosen for its flat and even surface that could be clearly seen in the OCT B-scan.

Table 5.1 displays the total number of B-scans taken for each specimen, the total time taken for the scans and the resultant frame rate. Specimen 1 was detached from the plant for 6 days. It should be completely dehydrated and therefore any fluctuation in plant diameter is a result of the inherent noise in the OCT system rather than any changes within the plant itself. Specimens 2 was scanned the same day it was detached. Specimen 2 would still be dehydrating and we would like to see if we can capture this change using the SD-OCT. Specimen 3 was still attached to the plant.

Table 5.1. Time scale of B-scans for the various specimens

Specimen	No. of B-scans	Total time for scans (s)	Time per scan (s)	Frame rate (Hz)
1	1000	344	0.344	2.91
2	2000	717	0.359	2.79
3	1000	489	0.489	2.04

Fig. 5.3 shows an example B-scan of a plant petiole. The example here is an image of Specimen 2. The plant petiole is positioned in the centre of the image, with a plastic cover on either side. False reflection artifacts are seen in the top section of the B-scan. Careful positioning of the petioles and plastic cover minimises these artifacts, which improves the accuracy of subsequent image processing.

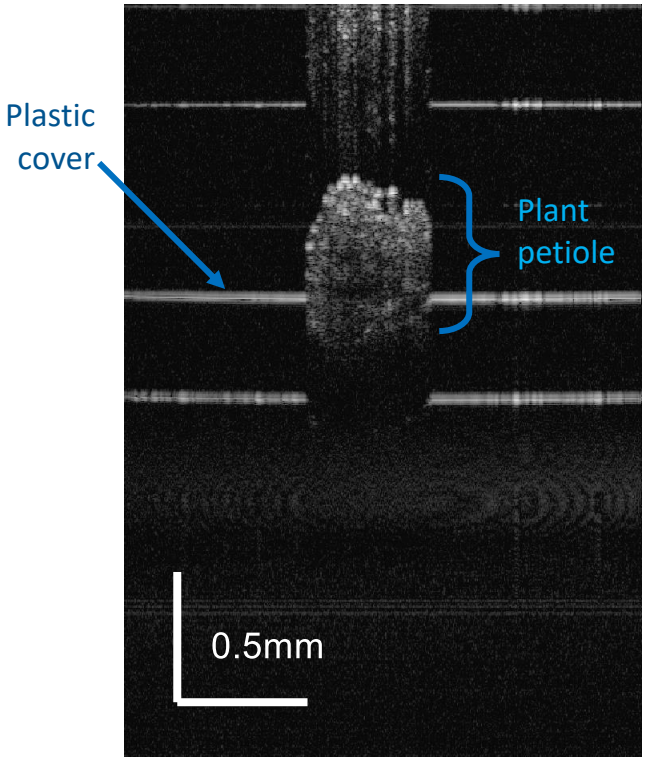

Fig. 5.3. An example of a B-scan image of a plant petiole. The plant petiole is positioned in the centre of the image, with plastic cover on either side. False reflection artifacts are seen in the top section of the B-scan.

5.2.2 Spectrometer-based OCT

The SD-OCT system used is an in-house system with a dual super-luminescent diode as the light source (Broadlighter D890-HP, Superlum, Carrigtwohill, Ireland). The laser emits at a central wavelength of 890nm and has a 150nm bandwidth. The system was previously measured to have an axial resolution of 2.5µm and a lateral resolution of 6.2µm [3].

Fig. 5.4 shows a schematic diagram of the SD-OCT system. The laser beam is passed through an optical fibre isolator (IO-F-SLD150-895, Thorlabs) and split into reference and sample beams using a 50:50 coupler (Nufern 630-HP fibre, Gould Fibre Optics, Millersville, Maryland).

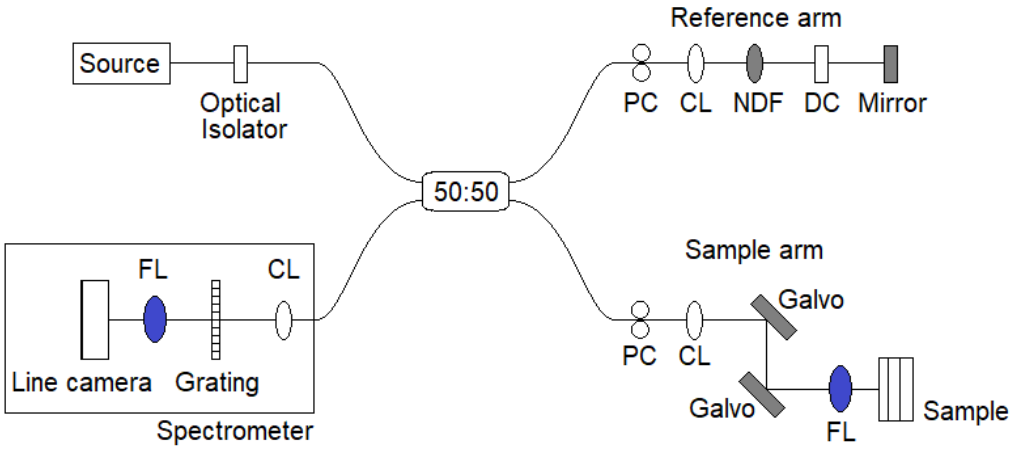

Fig. 5.4. Schematic diagram of the in-house spectrometer-based OCT used to image plants. PC = polarization controller, CL = collimator, FL = focus lens, NDF = neutral density filter, DC = dispersion compensator

In the reference arm, the reference beam is passed through a polarization controller (PolaRITETM, General Photonics, Chino, California), a collimator (PAF-X-5-B; Thorlabs) and a dispersion compensator (LSM02DC, Thorlabs) before being reflected by a fixed plane mirror. The light intensity is adjusted using a neutral density filter.

In the sample arm, the incident beam is once again passed through a polarization controller (PolaRITETM, General Photonics, Chino, California) and collimator (PAF-X-5-B; Thorlabs). A

pair of galvo-mounted mirrors aid in acquiring B-scans and C-scans. The beam is focused using a telecentric OCT scan lens (LSM02-BB, Thorlabs).

The reference and sample beams interfere and the interferogram is measured using a spectrometer. The spectrometer consists of a 1200-line pair/mm diffraction grating (Wasatch Photonics, Inc, Durham, North Carolina) and a 2048-pixel line camera (Aviiva, EV71yEM1GE2014-BA9, e2v, Chelmsford, United Kingdom).

5.2.3 Thresholding

Image processing of the B-scans was done using MATLAB's Image Processing Toolbox (MATLAB, 2017b). Firstly, the grayscale B-scans were converted into black and white (binary) images. The effect of different thresholds on a B-scan was investigated. Any grayscale value below this threshold is assigned a zero value (black), whereas any value above the threshold is given a new value of 1 (white). By default, MATLAB's *imbinarize* function chooses an appropriate threshold using Otsu's method. The thresholding is, therefore, adaptive and every B-scan has a different threshold. Dynamic speckle is expected due to the nature of OCT, so we expect an adaptive threshold to be more suited for this application.

Fig. 5.5 (centre-left) shows the effects of using an adaptive threshold. An adaptive threshold using Otsu's method resulted in a binary image that still had significant false reflections around the peak of the plant stem and could affect the detection of the stem peak. This threshold is thus too low. In contrast, when the threshold is set too high, the binarized image may have reduced noise but this can lead to an inaccurate stem peak being detected. Fig. 5.4 (far-right) shows the binarized image obtained when the threshold is too high, using a global threshold of 0.5. The optimal threshold value, which reduces false reflections while

maintaining an accurate stem peak was found to be 0.1 above the threshold found using Otsu's method (Fig. 5.5, centre-right). This adaptive threshold was also suitable threshold for the other specimens.

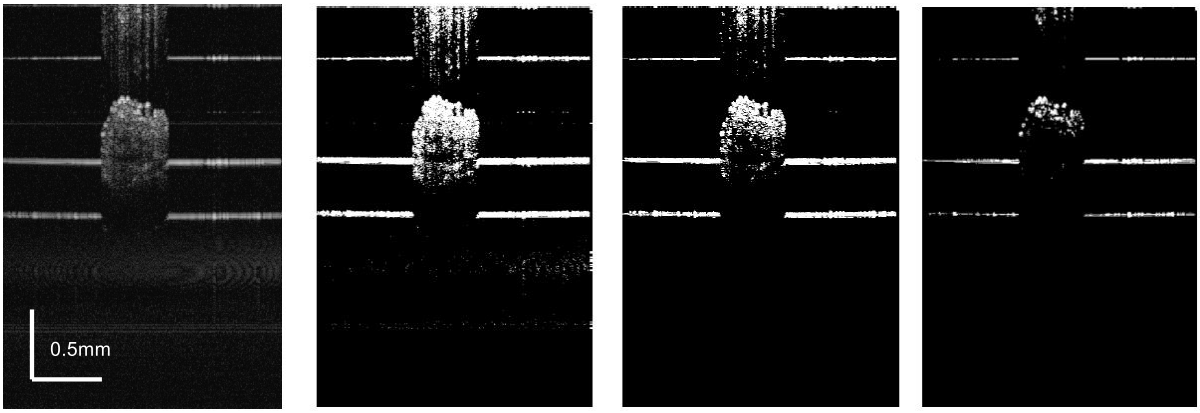

Fig. 5.5. Effect of different threshold values for specimen 2. Far-left: Original image shown for comparison. Centre-left: An adaptive threshold using Otsu's method (threshold value = 0.24) still generated noise that would affect the detection of the petiole peak. Centre-right: The optimal threshold value, which reduces false reflections while maintaining an accurate stem peak was found to be 0.1 above the threshold found using Otsu's method (threshold value = 0.34). Far-right: A threshold that is too high (threshold value = 0.5) leads to an inaccurate stem peak being detected.

5.2.4 Image processing to find plant petiole height

To find the position of the petiole peak, a rectangle around the petiole peak is given as a priori knowledge (blue box in Fig. 5.6). MATLAB then locates the white pixel within this rectangle that has the highest position, i.e. the point with the smallest value of z, and records its z-coordinate.

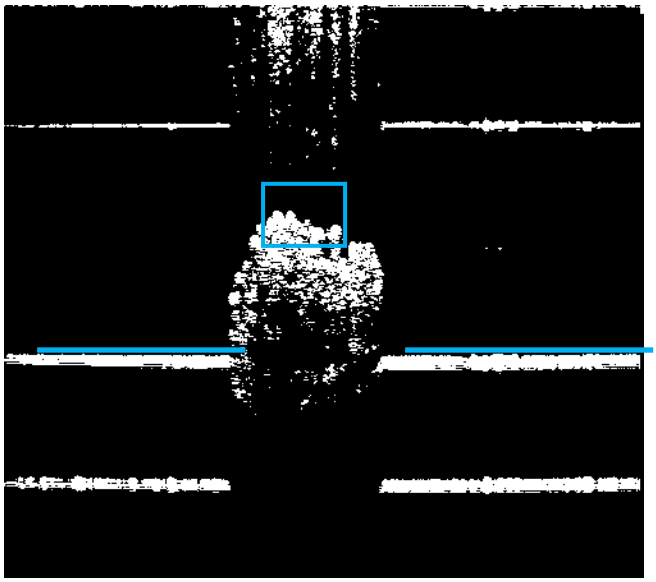

Fig. 5.6. Binary image of a B-scan of specimen 2, showing the a priori knowledge given for petiole peak and cover detection. The petiole peak is located within the blue rectangle, while the position of the plastic cover is underneath the blue horizontal lines.

Due to the nature of OCT, dynamic speckle as well as noise is expected. Thus, there is variation in the position of the cover. Moreover, the cover may not have uniform thickness. By giving a priori knowledge to MATLAB about where the top of the cover is (blue horizontal lines in Fig. 5.6), MATLAB can find the mean z-coordinate of the cover. The vertical distance between the mean z-coordinate of the cover and the z-coordinate of the petiole peak gives us a measure of the petiole height.

As the cover is used as the reference, the actual diameter of the petiole is not determined. The unknown refractive index of plant tissue also renders any calculation of the petiole diameter uncertain. Furthermore, due to the limited penetration depth of the SD-OCT, it is impossible to determine the interface between the petiole and the plastic cover. Instead, the change in position of the petiole peak with respect to the first B-scan is recorded.

5.2.5 Statistical analysis

For each specimen, the mean and corrected sample standard deviation of the petiole diameter over the entire scanning period is calculated. In addition, to improve the stability of the petiole diameter measurements over time, the mean is calculated over moving time-windows of length 25 B-scans and 100 B-scans and compared against results using no time-averaging. Table 5.2 shows the resultant frame rate for each specimen.

Table 5.2. Frame rate and period for different averaging lengths. Using a moving time average of 25 B-scans would decrease the frame rate by 25 times; an averaging length of 100 B-scans would decrease it by 100 times

Averaging length / Specimen	1 B-scan		25 B-scans		100 B-scans	
	Frame rate (Hz)	Period (s)	Frame rate (Hz)	Period (s)	Frame rate (Hz)	Period (s)
1	2.91	0.344	0.116	8.60	0.0291	34.4
2	2.79	0.359	0.112	8.98	0.0279	35.9
3	2.04	0.489	0.082	12.23	0.0204	48.9

If the petiole diameter remains stable over time, the time-series of the change in petiole peak position should fluctuate randomly about zero. The standard error (SE) of the 25 B-scans and 100 B-scans time averages should be 5 times and 10 times lower than the standard deviation respectively. If this expectation does not hold true, it suggests that there is a correlation between consecutive frames and measurements of the petiole diameter may be contaminated by more than stationary white noise.

To characterize the noise of the measurements, a fast Fourier transform is performed and the power spectral density is calculated by taking the squared modulus of the Fourier transform, scaled by the sampling interval and the total number of B-scans. This is the same formula used to calculate the noise spectral density in Ch 2.2.3. For reference, the equation is replicated below.

$$P[f] = \frac{\Delta t}{N}\left|\sum_{n=0}^{N-1} x[n] \cdot e^{-i2\pi f n}\right|^2 \quad , \frac{-1}{2\Delta t} < f < \frac{1}{2\Delta t} \tag{5.1}$$

Δt is the sampling interval, *N* is the number of data points, *f* is the frequency and *x* is the value of the data point at $t = n \cdot \Delta t$.The variance of the zero-mean random noise is found by looking at the floor of the power spectrum. The mean and standard deviation at higher frequencies should be equal and indicate the variance of the random noise.

5.3 Results

5.3.1 Specimen 1 – completely dehydrated leaf

Specimen 1 was detached from the plant stem and allowed to dehydrate completely for 6 days. Fig. 5.7 shows how the petiole diameter fluctuates over time. The data has a standard deviation of 1.0 µm. The overall mean change in petiole diameter is 0.2 µm. The diameter fluctuates over a range of 5 µm, which is the equivalent of 2 pixels. The minimum change in diameter is 2.5µm, as this was the previously measured axial resolution of the system [3]. The axial resolution reported is measured in air, as the refractive index of the plant tissue is unknown.

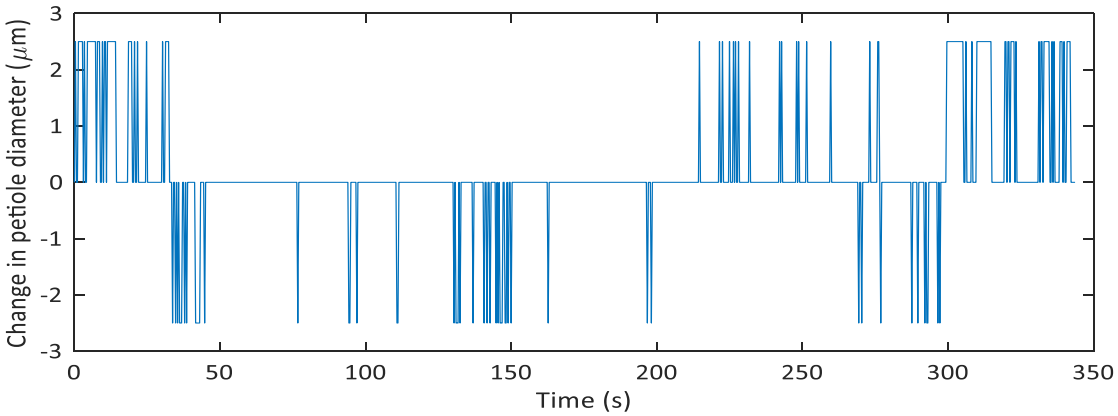

Fig. 5.7. Changes in petiole diameter over time for specimen 1 (dehydrated petiole). The petiole diameter varies by ±2.5 µm over time, which is the equivalent of a 2-pixel range. The standard deviation is 1.0 µm.

A moving time averaging window of 25 and 100 B-scans is applied and Fig. 5.8 shows how these compare with the mean. The time-averaged samples have a smaller range compared to Fig. 5.7, as indicated by their smaller SE, which are 0.6 µm and 0.5 µm for the averaging lengths of 25 and 100 B-scans. Based on their averaging lengths, one would expect a standard deviation of 0.2 µm and 0.1 µm respectively. The discrepancy in the actual and expected standard deviation could allude to a correlation between consecutive diameter measurements.

Specimen 1 was detached from the plant for 6 days before being scanned, so it was assumed completely dehydrated and, disregarding any noise, should display a steady diameter measurement. The time-averaged diameters fluctuate randomly around the overall mean diameter, but is significantly above the overall mean at the start (t < 30s) and end (t > 300s) of the measurement period. To find out whether this is simply noise or if the measurements have been contaminated by a deterministic signal, the power spectrum of the diameter measurements is computed (Fig. 5.9). The power spectrum has a peak of $3.6 \times 10^7 \mu m^2/Hz$ at 0 Hz but no other discernible peaks. The floor of the power spectrum has a mean of 0.5 µm^2/Hz with a frequency resolution of 1.5 mHz. The standard deviation of random noise is

therefore 0.7 µm over a measurement bandwidth of 1.45 Hz, which is slightly smaller than the standard deviation of 1.0 µm calculated above.

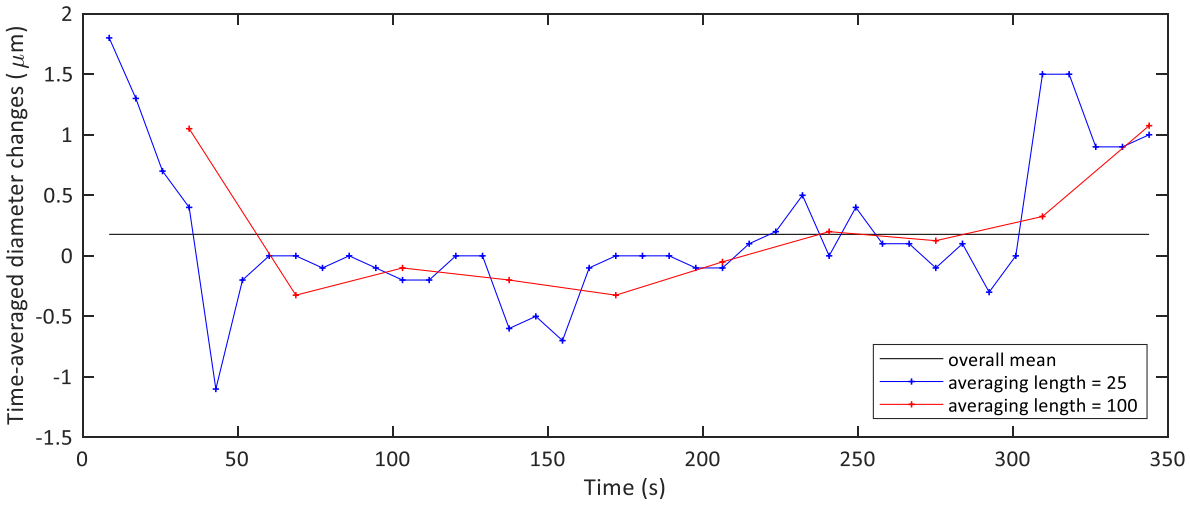

Fig. 5.8. Moving time average of specimen 1 (dehydrated petiole) using different averaging lengths. The black line shows the mean of all 1000 B-scans, which is 0.2 ±1.0 µm. The time series, using averaging lengths of 25 and 100 B-scans, hover around the overall population mean, with an increase in petiole diameter at the start and end of the scanning period. The SE are 0.6 µm and 0.5 µm for the averaging lengths of 25 and 100 respectively.

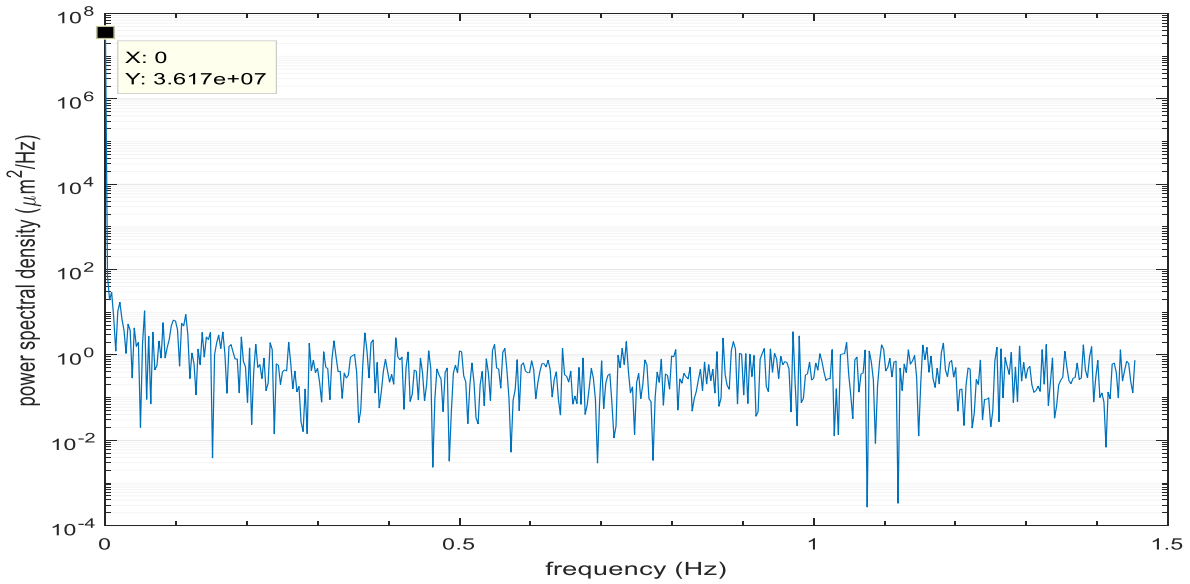

Fig. 5.9. Power spectral density of the petiole diameter measurements of specimen 1 (dehydrated petiole). There is a peak at 0 Hz but no discernible peaks otherwise. The floor of the power spectrum has a mean of 0.5 µm^2/Hz, indicating that the standard deivation of random noise is around 0.7 µm over a measurement bandwidth of 1.45 Hz.

5.3.2 Specimen 2 – dehydrating leaf

The petiole diameter decreases steadily over time from 2.5 µm to -20 µm in 717s (Fig. 5.10). The overall population mean is -9.2 µm with a standard deviation of 6.5 µm. As specimen 2 was scanned the same day it was detached from the plant, the reduction in diameter is assumed to be due to dehydration of the specimen. The standard deviation was at least 6 times more than that for specimen 1, which suggests that using a constant overall population mean does not adequately represent the data. A moving mean, which decreases linearly over time, would be more appropriate. The residual, which is the difference between the data and the moving mean, is used instead to calculate the standard deviation.

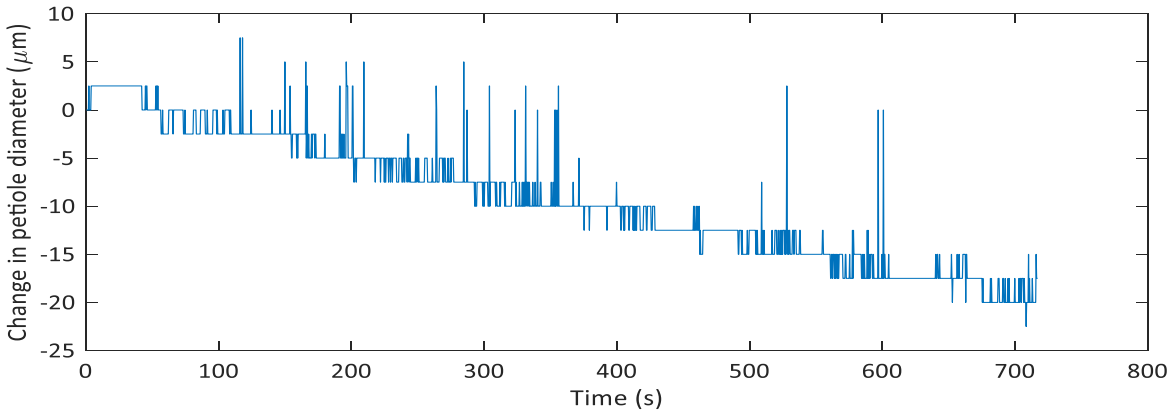

Fig. 5.10. Change in petiole diameter over time for specimen 2 (dehydrating petiole). The diameter decreases steadily over time from 2.5 µm to -20 µm.

Fig. 5.11 shows a trendline fitted using simple linear regression and the time-averaged petiole diameters. For both averaging lengths, the time averages follow the trendline quite closely. With a moving mean, the SE for averaging lengths of 1, 25 and 100 are 1.7 µm, 0.7 µm and 0.4 µm. These are similar to those obtained from specimen 1, which were 1.0 µm, 0.6 µm and 0.5 µm. This suggests that using a 100 B-scan moving average window results in a consistent 0.5 µm degree of accuracy. Without time averaging, the measurements would have an accuracy of around 1.3 µm.

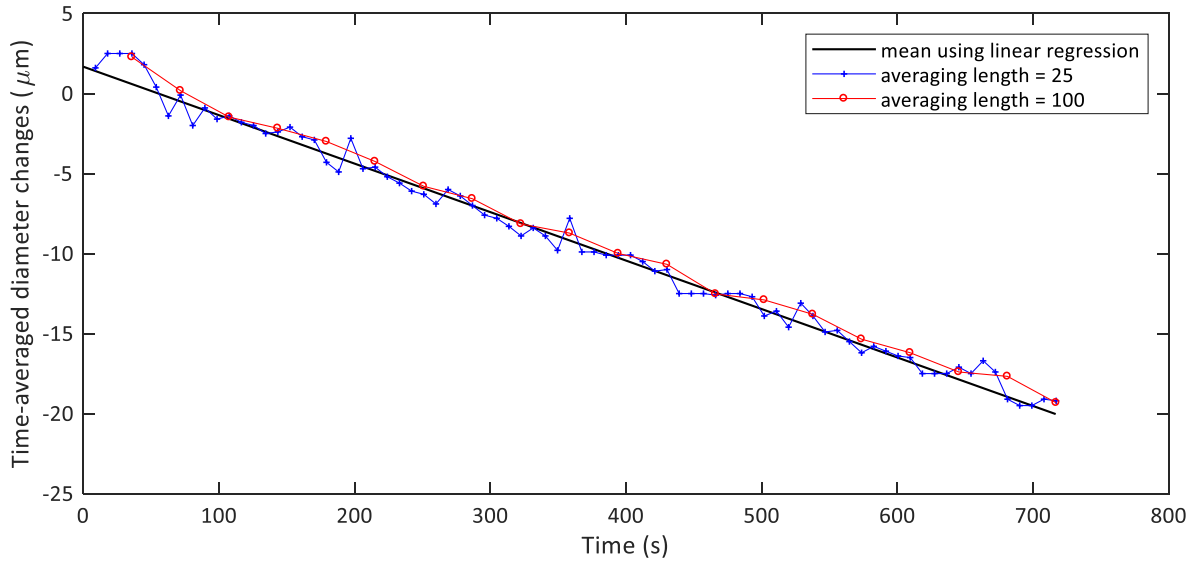

Fig. 5.11. Moving time average for specimen 2 (dehydrating petiole) using a simple linear regression line. The line has a gradient of -0.03 and a y-intercept of 1.7. The standard deviation of the residuals, which is the difference between the diameter measurements and the regression line, is 1.7 µm. The SE using the averaging lengths of 25 and 100 are 0.7 µm and 0.4 µm respectively.

The power spectrum for specimen 2 has a 0 Hz peak of $1.5 \times 10^8 \mu m^2/Hz$. The floor of the power spectrum has a mean of 2.0 µm^2/Hz, giving an standard deviation of random noise of 1.5 µm over a measurement bandwidth of 1.39 Hz, which is close to the standard deviation of 1.7 µm. Besides the peak at 0 Hz, there are no discernible peaks otherwise. These observations of the power spectrum are comparable to those obtained for specimen 1.

5.3.3 Specimen 3 – still attached

Specimen 3 is used to ascertain whether there are any deterministic fluctuations in the petiole diameter while the petiole is still attached to the plant. Fig. 5.12 shows changes in the petiole diameter over time for specimen 3. The diameter fluctuates over a range of 7.5 µm, which is the equivalent of 3 pixels. The standard deviation is 1.5 µm.

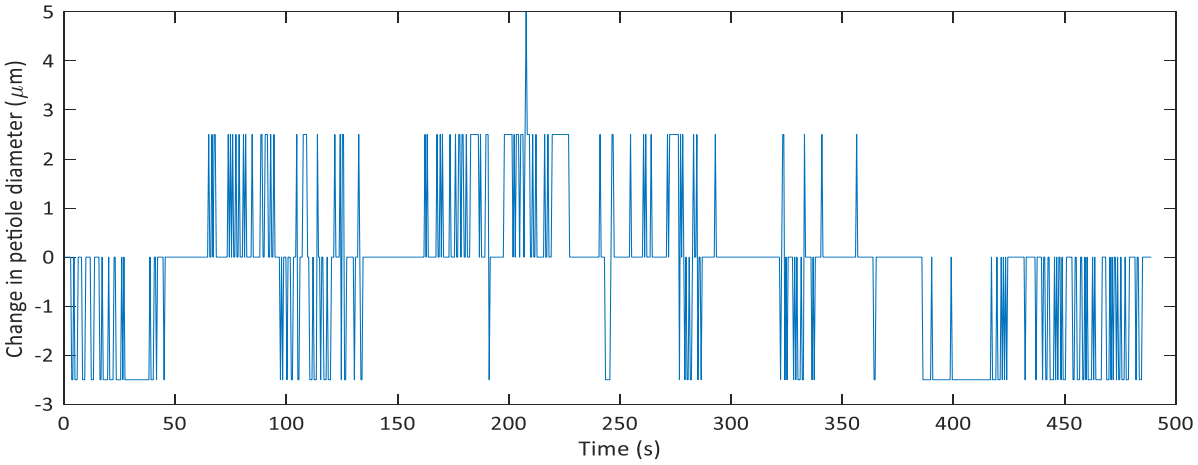

Fig. 5.12. Change in petiole diameter over time for specimen 3 (attached petiole). The petiole diameter varies by 7.5 µm over time, equivalent to a 3-pixel range. The standard deviation is 1.5 µm.

Fig. 5.13 shows the mean change in petiole diameter, calculated using different time averaging windows. Like specimen 1, the time series hover around the overall population mean, with a decrease in petiole diameter at the start (t < 150s) and end (t > 300s) of the measurement period.

To determine whether this is simply noise or if the measurements have a deterministic signal, the power spectrum is computed. The power spectrum has a peak at 2.04 mHz, or a period of 489s, which is the length of the sample. No other significant peaks present. The floor of the power spectrum is around 1.0 µm^2/Hz. The standard deviation of random noise is therefore 1.2 µm over a measurement bandwidth of 0.9 Hz, which is slightly smaller than the standard deviation obtained.

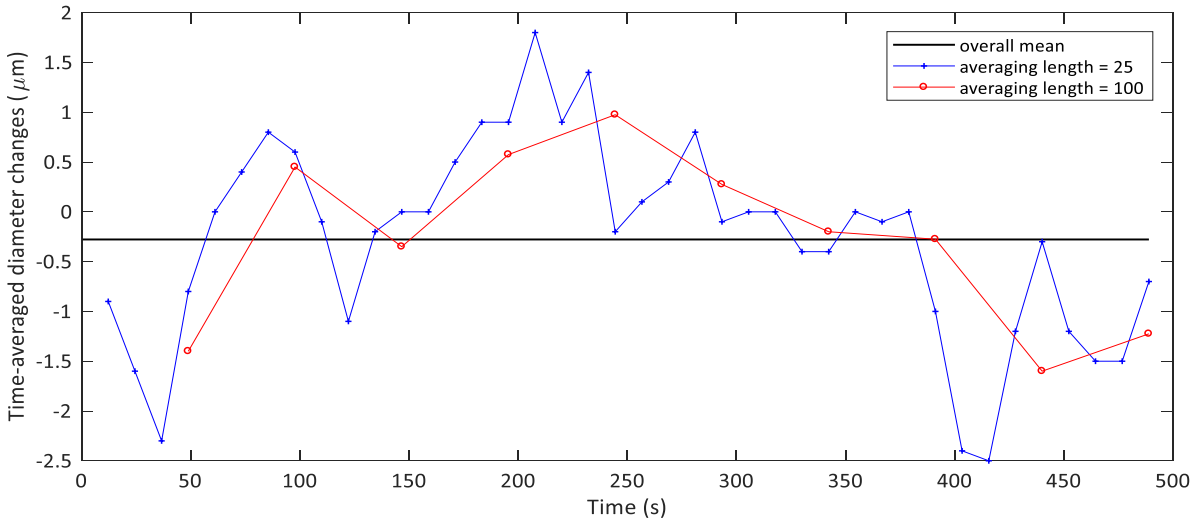

Fig. 5.13. Moving time averages for specimen 3 (attached petiole) using different averaging lengths. The black line shows the mean of all 1000 B-scans, which is -0.25 ±1.47 µm. For the averaging length of 25 and 100 B-scans, the averaged petiole diameter hovered around the overall population mean, with a decrease in petiole diameter at the start and end of the scanning period.

5.4 Discussion & Conclusions

This is an exploratory study investigating the stability of diameter measurements of plant petioles. OCT can image the plant petiole to an accuracy of around 1.2 µm using a frame rate of around 2.5 Hz. Table 5.3 summarizes how the standard deviation of random noise, calculated using the power spectral density, changes depending on the specimen. Specimen 1 has the lowest standard deviation of 0.7 µm over a measurement bandwidth of 1.45 Hz, most likely due to it being completely dehydrated before imaging. Specimen 2 shows an standard deviation of 1.5 µm over a measurement bandwidth of 1.39 Hz. When detached from the plant and immediately imaged, specimen 2 shows a linear decrease in the petiole diameter over time, possibly because of the dehydration of the petiole. When the petiole is still attached to the plant, dehydration does not occur and the standard deviation is 1.2 µm over a bandwidth of 0.9 Hz.

Table 5.3. Summary of petiole diameter stability for all specimens. The table shows whether the specimen is attached to the plant and its state of dehydration.

Specimen	Attached to plant	State of dehydration	Standard deviation of random noise using power spectrum over bandwidth of around 1.5 Hz
1	No	Dehydrated	0.7 µm
2	No	Dehydrating	1.5 µm
3	Yes	N/A	1.2 µm

Using moving time averaging windows of 25 and 100 B-scans reduces the frame rate, but lowers the standard deviation of the random noise to 0.7 µm and 0.5 µm respectively. Each frame encompasses around 9s and 36s respectively and any changes to the plant petiole within this period would be rendered unnoticeable. Knowledge about the time scale within which changes to the plant petiole occur is needed before a suitable frame rate can be decided upon. According to Mousavi et al. [1], when measuring the surface potential changes in response to wounding, the changes occur within 10s of seconds and last for up to 3 mins. The sampling rate used is around 1Hz. This falls within the limits of our SD-OCT system.

We have demonstrated that SD-OCT is a suitable imaging modality for accurately tracking changes in plant petiole diameter. This gives us an indication of the changes in turgor pressure within the plant stem. Due to the limited number of specimens available, we were unfortunately unable to repeat the experiments in order to test for reliability. The next step would be to wound the plant while measuring changes in petiole diameter.

The results of this experiment have been published by Williams et al [4]. To avoid mechanically agitating the plant whilst it is being imaged, the wounding mechanism is a 30s-long laser pulse from an 800nm 6W laser. The central vein of an adjacent leaf is imaged with ~1Hz frame rate. The algorithm used tracks displacements in both the z and x directions, to account for potential translations and rotations of the leaf that are not part of the wounding

response. The results conclusively show that OCT is able to detect 10-30 µm changes to the central vein diameter over the course of 10mins.

References

[1] S. A. R. Mousavi, A. Chauvin, F. Pascaud, S. Kellenberger, and E. E. Farmer, “Glutamate receptor-like genes mediate leaf-to-leaf wound signalling,” Nature **500**(7463), 422–426 (2013).

[2] E. E. Farmer, D. Gasperini, and I. F. Acosta, “The squeeze cell hypothesis for the activation of jasmonate synthesis in response to wounding,” New Phytol. **204**(2), 282–288 (2014).

[3] J. Boadi, "Clinical applications of ultra-high resolution and phase-sensitive optical coherence tomography," University of Sheffield (2016).

[4] J. Williams, W. C. Lin, W. Li, S. Wang, S. J. Matcher, and A. A. Chauvet, "Translating Optical Coherence Tomography Technologies from Clinical Studies to Botany: Real Time Imaging of Long-Distance Signaling in Plants," Optical Coherence Tomography, Optical Society of America, OM4E-6 (2020).

Chapter 6: Quantification of Biofilm Thickness

6.1 Introduction

Biofouling is the scenario where pipes in water distribution and water filtration systems become contaminated from the build-up of bacterial biofilm. Besides the health risks involved, biofouling also bears economic costs, as pipes and filters need cleaning and replacing [1]. Dreszer et al have demonstrated the potential of OCT for imaging biofilm *in situ* to study its spatial and temporal distribution [2]. This could allow researchers to understand how and when biofouling occurs, aiding in the design of biofilm-resistant membrane systems [3]. Dreszer et al used a spectrometer-based OCT system with an axial resolution of less than 5.8 µm and a lateral resolution of 8 µm. The biofilm was grown in a test cell with a fixed crossflow velocity. Due to the flow conditions, the OCT system was able to pick out biofilm growth of around 200 µm thickness in 4 days. The rate of biofilm growth is dependent on the flow conditions of the pipes as well as the growth period [4]. The thickness of biofilm when imaged with OCT can vary from 50-400 µm [5] to 1.3-1.6 mm [6].

The aim of this investigation is to determine if there is a minimum detectable limit when using OCT for the quantification of biofilm thickness. The biofilm samples are grown within a testing rig that simulates a potable water distribution system [7]. As the water circulating the pipes is drinking water, a high volume of biofilm growth is neither desired nor expected. Therefore, the biofilm thickness measured would be very thin (<50 µm).

Two batches of biofilm samples were evaluated. Samples in the first batch were allowed to accumulate biofilm for a maximum of 28 days. The samples were grown in water with differing chlorine regimes. It is hypothesized that a higher concentration of chlorine prevents the growth of biofilm and results a lower biofilm thickness.

In the second batch, the samples were fed by water containing different concentrations of assimilable organic carbon (AOC). A greater concentration of AOC is hypothesized to cause greater accumulation of biofilm, as growth of bacteria, and consequently biofilm, would not be limited by the amount of carbon.

6.2 Materials & Methods

6.2.1 Biofilm samples and expected volume

Fig. 6.1 shows a schematic diagram of the testing rig. The testing rig is a pipe loop that simulates a water distribution system by circulating potable water [7]. It consists of pipe loops made of high-density polyethylene (HDPE). Pipes in the UK's water distribution system are made from this material. Water is constantly circulated within these pipes and biofilm grows on the inside surface of the pipes. The coupon sampling device is a detachable section within the testing rig that is used to sample the amount of biofilm build-up within the pipe. The "insert" is part of the coupon that can be removed. As biofilm grows within the pipes, it also grows on top of the insert. Biofilm was grown and the insert samples were provided by Dr Frances Pick and Dr Katherine Fish from the Department of Chemical and Biological Engineering at The University of Sheffield.

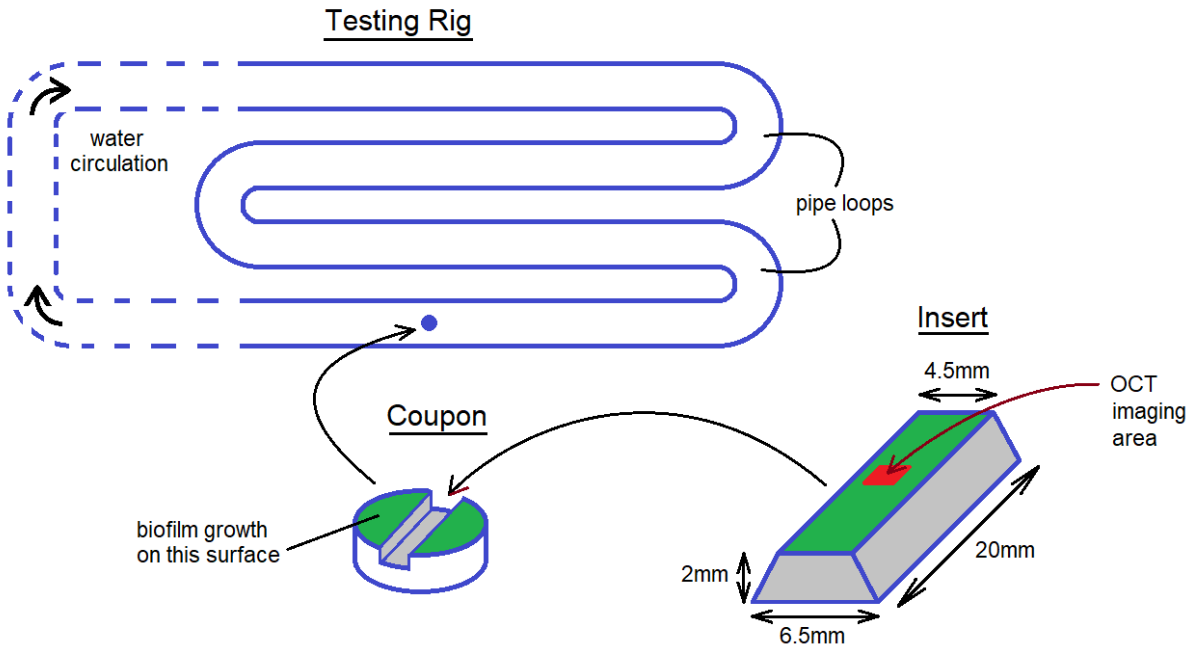

Fig. 6.1. Schematic diagram of testing rig used to grow biofilm. Water is constantly circulated within the pipe loops of the testing rig. The coupon sampling device is part of the pipe loop and made of the same HDPE material. As biofilm grows inside the pipes, it also grows on the coupon. The insert is a part of the coupon that is removed for imaging purposes. OCT was used to image the top of the insert, where biofilm is expected.

Samples in batch 1 are made of blue-coloured HDPE. Table 6.1 shows the growth regimes of the different samples. Sample 000 is a control sample that does not contain any biofilm and was never inserted into the testing rig. Sample 133 was in the pipe loop for ≤90 minutes, which should be too short a duration for any biofilm to develop. Samples 138 and 353 have biofilm growing in the pipe loop for 28 days. Sample 353 was grown in dechlorinated water and is expected to have the highest volume of biofilm. The water was dechlorinated by dosing it with a 1% solution of sodium ascorbate (Vit-D Chlor, United States) [8]. Samples 133 and 138 were not dosed, which meant that their chlorine concentration was determined by incoming tap water.

Table 6.1. Growth regimes of samples in batch 1. Sample 133 has the shortest growth duration, so is expected to have the lowest volume of biofilm. Samples 138 and 353 were both grown for 28 days each. Sample 353 was grown in dechlorinated water, so is expected to have the highest volume of biofilm. Sample 000 is a control sample that does not contain any biofilm.

Sample Code	Chlorine Regime	Growth duration (days)	Expected Volume
000	n/a	0	None
133	No Dosing	0	Lowest volume
138	No Dosing	28	
353	Dechlorinated	28	Highest volume

Samples in batch 2 are made of black-coloured HDPE. They were grown in a pipe loop test facility at three water treatment works at Scottish Water [9]. Table 6.2 shows the growth regimes of this batch of samples. Samples in this batch are grown for 9 months, about 9 times longer than samples in batch 1. The volume of biofilm in batch 2 is expected to be significantly more than those in batch 1. Sample 3 is grown in water with the highest concentration of AOC, so is expected to have the highest volume of biofilm. By the same logic, sample 2 is expected to have the lowest biofilm volume.

Table 6.2. Growth regimes of samples in batch 2. All samples are grown for 9 months. Sample 2 and 3 have the lowest and highest AOC concentration respectively. Hence, they are expected to have the lowest and highest volume of biofilm.

Sample Code	AOC Concentration	Growth duration (months)	Expected Volume
1	Med	9	
2	Low	9	Lowest volume
3	High	9	Highest volume

6.2.2 Comparing different OCT systems for imaging

The two different OCT systems available are used to image batch 1, to determine the best OCT system to use: the spectrometer-based OCT (SD-OCT) described Ch 5.2.2 and the polarization-sensitive (PS) OCT described in Ch 3.2.3. The samples are tilted at an angle to reduce reflections at the surface of the insert, which would interfere with viewing the biofilm. The parameters for OCT imaging are given by Table 6.3. The samples in batch 1 were imaged using both the PS-OCT and the SD-OCT. As it was determined that the SD-OCT was better at imaging biofilm, samples in batch 2 were only imaged using the SD-OCT.

Table 6.3. Parameters for OCT imaging of biofilm samples.

Batch no.	OCT system used	Lateral pixel size (μm)	Area imaged (mm)
1	PS-OCT	4.2	4.0 × 2.0
	SD-OCT	4	4.0 × 3.0
2	SD-OCT	4	4.0 × 1.0

6.2.3 Image processing

Fig. 6.2(top) shows the original structural image for a sample with biofilm and one without. The image on the right is an example with biofilm (specifically, sample 3 of batch 2) and the image on the left is the underside of the same sample, which acts as a control.

To analyse these structural images quantitatively, the images were first straightened using *ImageJ* software. Fig. 6.2 (middle row) shows the structural images when they have been straightened in this way. As there is poor depth penetration with the insert material and the biofilm is expected to be very thin, it is difficult to determine the biofilm-insert interface. The

central dark line in the image, as indicated by the red arrow, is taken as the biofilm-insert interface and is manually determined in *ImageJ*. It is this line that is used to straighten the image.

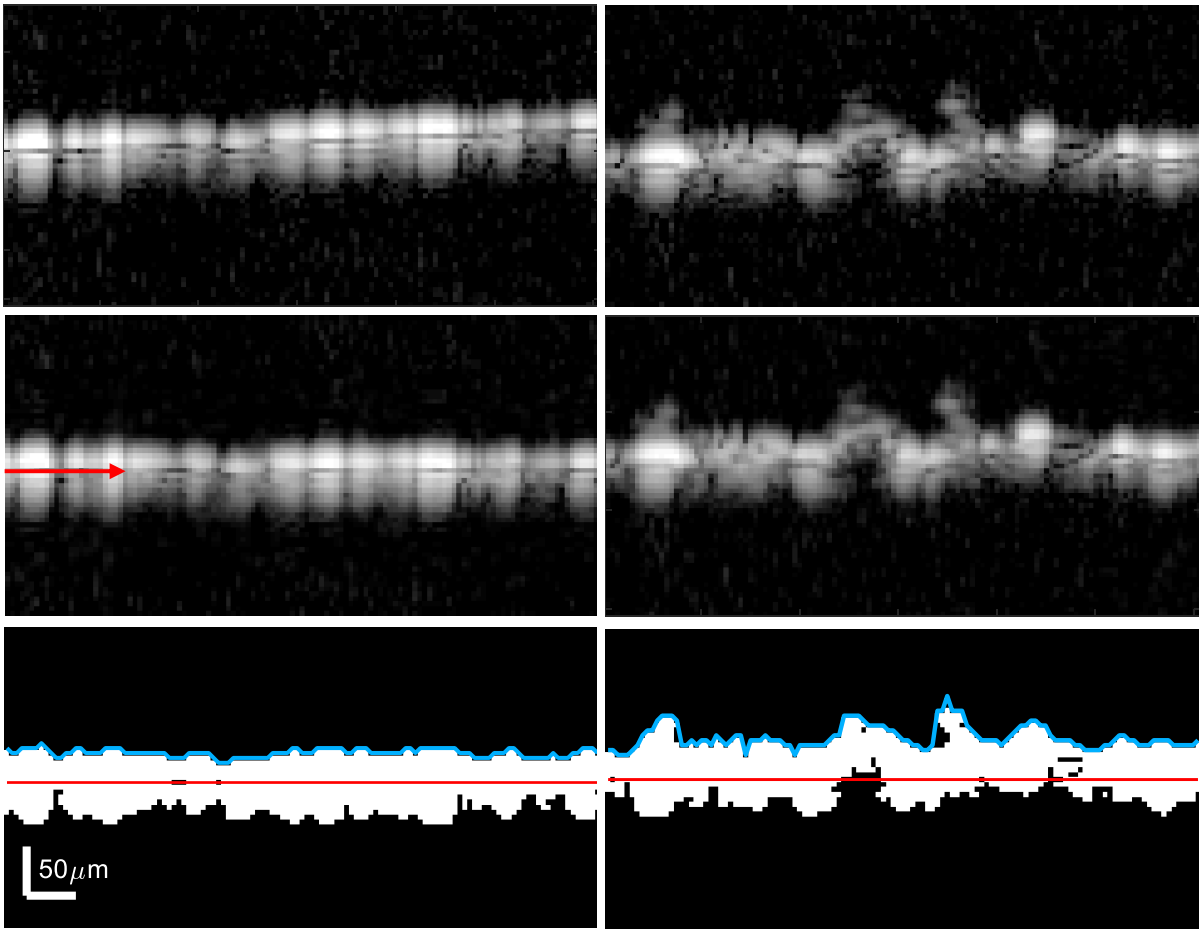

Fig. 6.2. Structural images of a sample with (right) and without (left) biofilm. Top: original B-scan. Middle row: structural images after being straightened using *ImageJ*. The red arrow is taken as the biofilm-insert interface. Bottom: Binarized image, with the top of the biofilm highlighted in blue and the biofilm-insert interface outlined in red.

MATLAB (MATLAB, 2019a) was then used to binarize the image using Otsu's method before finding the top of the biofilm. More details on the selection of the threshold using Otsu's method can be found in Ch 5.2.3. Fig. 6.2 (bottom) shows the binarized image with the top of the biofilm highlighted in blue. The thickness of the biofilm is determined by finding the distance between the top of the biofilm and the biofilm-insert interface (red line). The average biofilm thickness is calculated by taking the arithmetic mean. When converting the biofilm

thickness from pixels to microns, the refractive index of the biofilm is assumed to be 1.333 [4].

6.3 Results and discussion

6.3.1 Comparing different OCT systems

Fig. 6.3 shows the retardance images of the four samples in batch 1. Retardance bands can clearly be seen, indicating that the samples are birefringent. However, it is unclear whether this is a manifestation of the biofilm present or variations in the insert material. Therefore, the undersides of the inserts are also imaged. There are bands present on the underside as well, indicating that the insert material is birefringent and that the birefringence is a property of the plastic insert material rather than due to biofilm thickness. A possible reason for birefringence in the material could be that it was introduced during manufacturing. The heating and cooling processes to mould plastic created stresses in the material which led to birefringence.

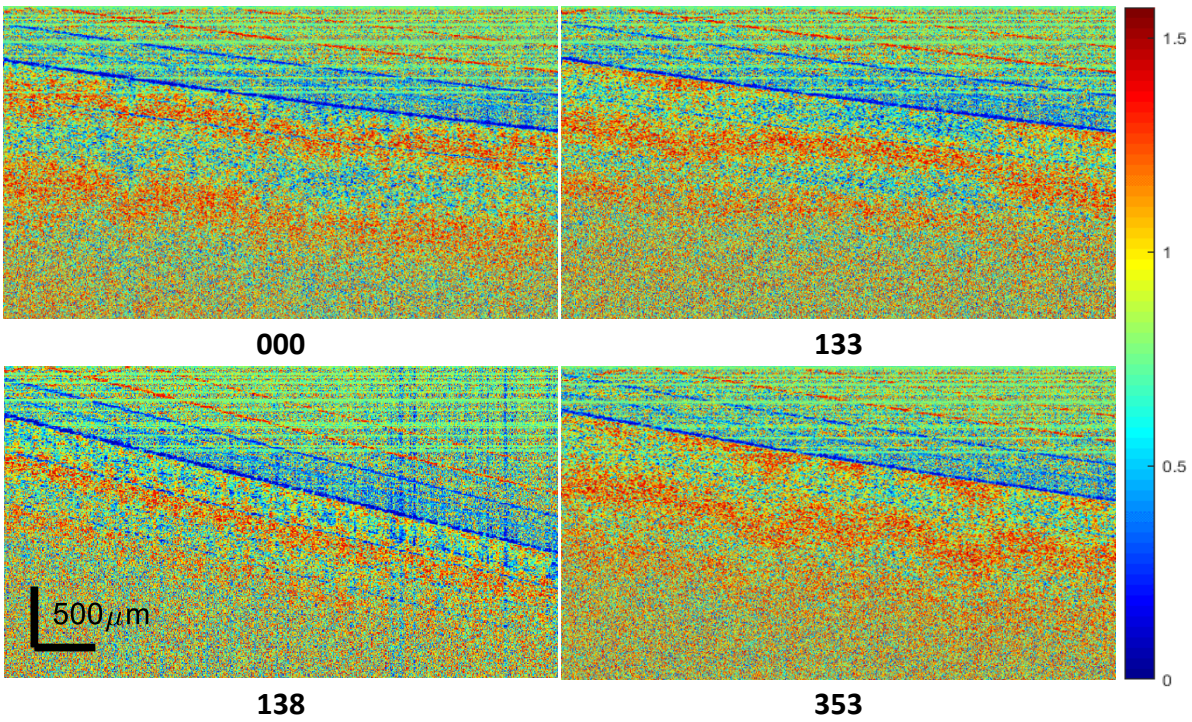

Fig. 6.3. Retardance images of batch 1 using PS-OCT. These images show the top of the insert where biofilm is expected. The samples are clearly birefringent. Retardance images of the underside of the insert also show birefringence, suggesting that the birefringence shown here is due to variations in the plastic insert material rather than biofilm thickness.

The width of the retardance bands, or band spacing, is the distance by which the retardance shifts by 2π radians (refer to Ch 3.2 for a more detailed explanation). By measuring the band spacing, and using Eq. 3.4, a rough estimate of the birefringence can be calculated. A difference in band spacing implies a difference in birefringence of the plastic between the samples. Table 6.4 shows estimates of the birefringence for the four samples for both sides of the insert. There seems to be a large variation in birefringence between the inserts but no correlation with the amount of biofilm present on the sample, which concurs with what is observed in the retardance images.

Table 6.4. Birefringence estimate of the top and underside of the samples. There seems to be a large variation between the inserts and no correlation with the amount of biofilm present on the sample.

Sample	Estimate of birefringence	
	Top of insert	Underside of insert
000	2.0×10^{-3}	No discernible bands
133	2.8×10^{-3}	4.4×10^{-3}
138	2.5×10^{-3}	3.7×10^{-3}
353	2.8×10^{-3}	4.9×10^{-3}

These results show that the insert material is birefringent and birefringence cannot be used to quantify biofilm thickness. Hence, the SD-OCT system is used to image the biofilm samples, as it has a smaller axial resolution and less ghost artefacts compared to the PS-OCT.

6.3.2 Biofilm thickness in batch 1

Fig. 6.4 shows the structural images obtained using the SD-OCT system. At first glance, biofilm cannot be seen on the surface of the substrate. The distinction between the samples, both with and without biofilm, is unclear.

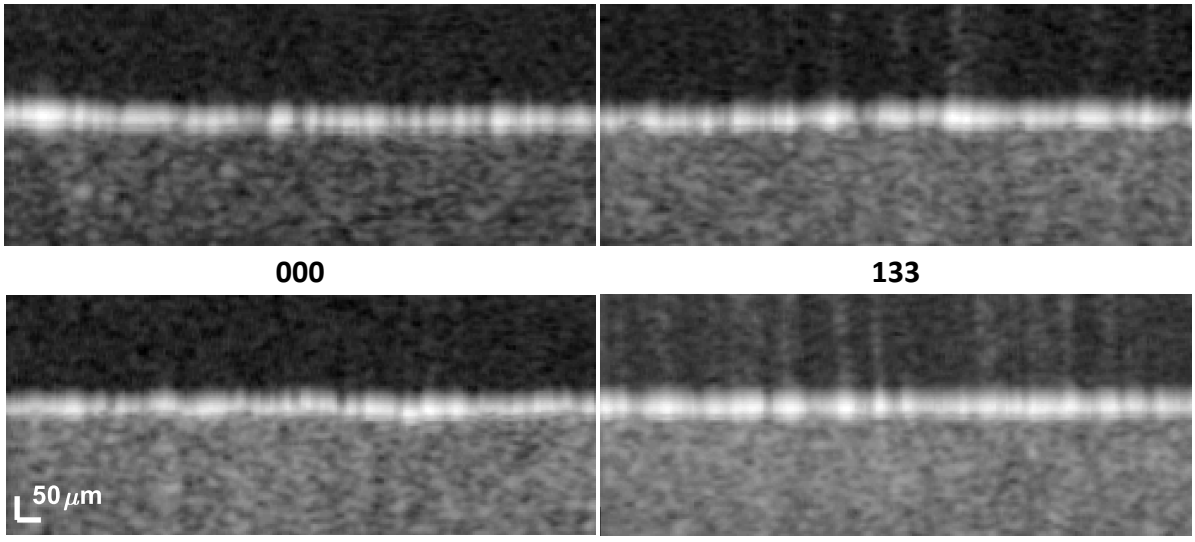

Fig. 6.4. Structural images of the four samples using the SD-OCT system. There are no clearly visible differences between the samples.

The images are straightened and the thickness of any biofilm is quantified. Table 6.5 shows the mean thickness calculated as well as the standard deviation, using 1000 A-scans. There is a greater calculated thickness in the samples with biofilm compared to the control sample (000), with the greatest thickness in sample 353.

Although the control sample 000 does not have biofilm, the algorithm used still calculated a "biofilm thickness" of 25.5 µm. Sample 133, which was grown in the pipe loop for 90 minutes, demonstrated a similar thickness to the other samples, even though it is not expected to have any biofilm. This could be due to the highly reflective insert material, as shown by Fig. 6.4. The resulting thickness calculated could be taking into account the Fresnel reflections at the surface. One way that this could be ameliorated is to tilt the insert at an angle so that the reflection from the incident beam is not picked up by the detector.

The standard deviation is similar for all four samples, with sample 000 having the highest standard deviation. This further contributes to the argument that the mean thickness calculated is a result of surface reflections rather than any indication of the presence of biofilm. Therefore, it is not possible to quantify biofilm in this batch of samples, most likely because the biofilm growth duration of 28 days is too short.

Table 6.5. Mean biofilm thickness for samples in batch 1.

Sample	Mean thickness (µm)
000	25.5 ±5.2
133	32.1 ±4.1
138	31.7 ±4.5
353	36.6 ±4.5

6.3.3 Biofilm thickness in batch 2

Fig. 6.5 shows the B-scans obtained from both the top and underside of the HDPE insert using the SD-OCT. As this batch had no control sample, the underside of the insert where there was no biofilm growth was taken as the control. This batch is made of black-coloured HDPE and shows poor depth penetration into the insert material.

The surface of at the top of the insert has visibly greater variation in local biofilm thickness compared to the underside, where no biofilm is expected. Thus, there is a visible difference between B-scans with and without biofilm. Sample 3 is expected to have the thickest biofilm and sample 2 the thinnest, but it is difficult to determine this by simply looking at the images.

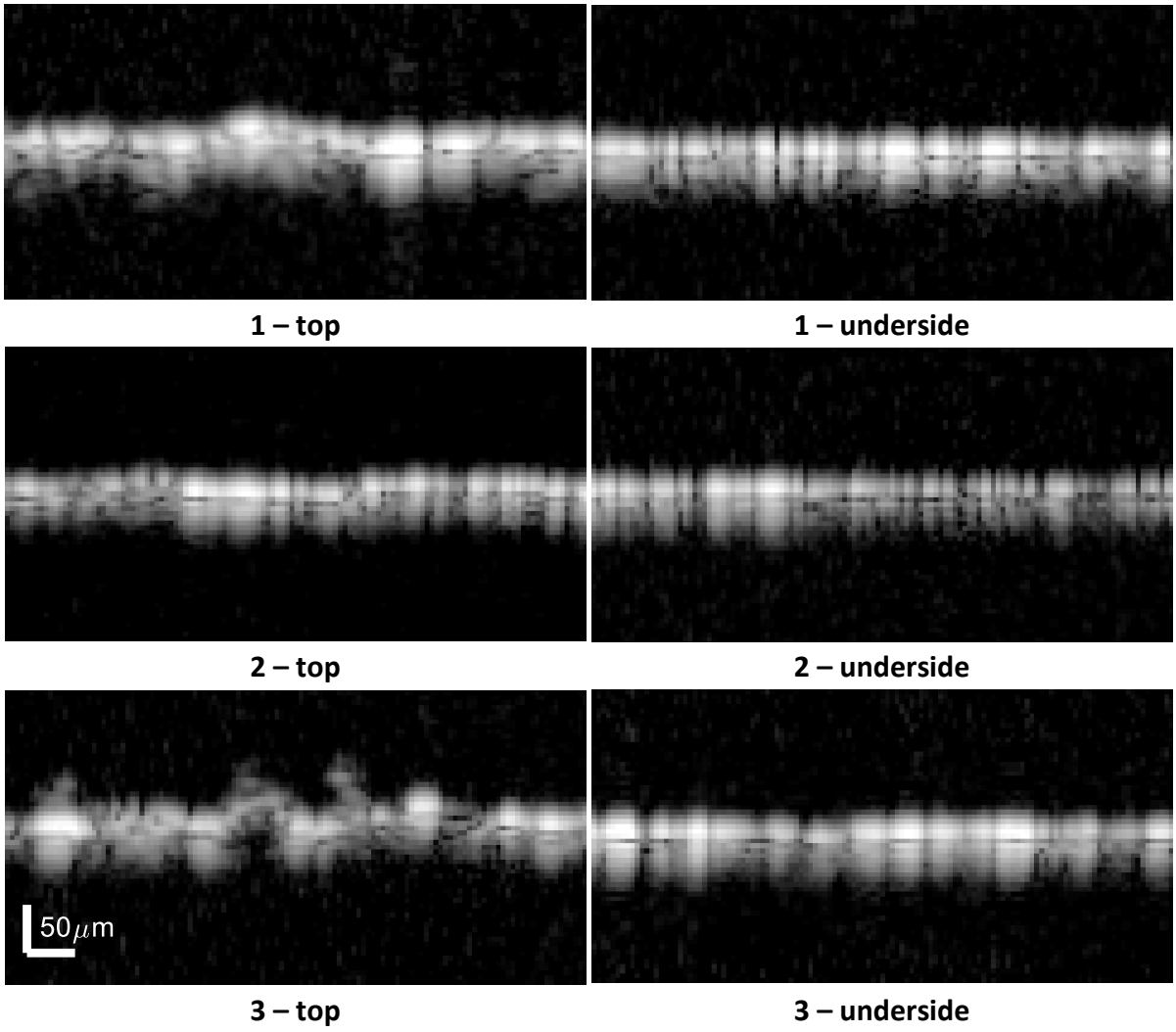

Fig. 6.5. SD-OCT structural images of samples in batch 2. Biofilm is expected to be present on the top of the insert. The underside of inserts, where biofilm is absent, is taken as the control.

B-scans of each sample are straightened using *ImageJ* and MATLAB was used to find the average thickness of the biofilm. Table 6.6 shows the average thickness for all samples, as well as the standard deviation. The mean thickness is higher for the top of the insert (with biofilm) compared to the underside of the insert (no biofilm), which indicates the presence of biofilm on the top of the insert. Samples without biofilm have a mean thickness of around 11.6 µm, while samples with biofilm have a mean thickness which varies from 13.1 µm to 16.6 µm. As biofilm does not grow evenly and varies spatially, surfaces without biofilm (i.e., the underside of the insert) are expected to have a lower standard deviation than samples with biofilm (top of the insert), which is demonstrated here.

Table 6.6. Mean biofilm thickness, for the top of the insert (with biofilm) and underside of the insert (no biofilm). The standard deviation is also given. The mean thickness is higher for the top of the insert (with biofilm) compared to the underside of the insert (no biofilm), showing that there is biofilm on the top of the insert. There is also a higher standard deviation for the top of the insert compared the underside. Sample 3 has the thickest biofilm and the highest standard deviation.

Sample	Mean thickness, top (μm)	Mean thickness, underside (μm)	*p*-value of *t*-test
1	14.1 ± 5.5	11.7 ± 3.8	1.5×10^{-28}
2	13.1 ± 5.2	11.0 ± 3.5	2.8×10^{-21}
3	16.6 ± 7.2	12.1 ± 3.1	2.6×10^{-73}

Using an unpaired two-sampled *t*-test, we aim to determine if the thickness calculated are statistically different between samples with biofilm (n=950) and samples without (n=950). Table 6.6 shows the *p*-value of the tests for each sample in batch 2. The *p*-value is less than 0.05 for all samples. Thus, we can reject the null hypothesis at the 5% significance level and conclude that the biofilm samples show significantly different thickness compared to the clean samples.

Sample 3 had the highest average thickness of 16.6 μm, indicating that it has the thickest biofilm. Likewise, sample 2 has the thinnest biofilm with an average thickness of 13.1 μm. This suggests that a higher AOC concentration leads to higher biofilm thickness, as hypothesised.

Batch 2 showed a lower thickness calculated compared to batch 1 even though the latter had a shorter growth duration. This could be a result of the Fresnel reflections on the surface of the samples. Even though the two batches of inserts are made from the same HDPE material, batch 2 attenuates NIR light more strongly than batch 1. There is clearly variation in the insert material that we were initially unaware of. It is possible that batch 1 samples had a more reflective surface than batch 2, resulting in a brighter reflection and higher "thickness" calculated. Future work in imaging biofilm using these inserts should therefore take into

account its highly reflective surface and take steps to reduce the surface reflections if possible.

6.4 Conclusions

For batch 1, the aim was to determine whether the presence of chlorine negatively affected the growth of biofilm. Based on the retardance images, the insert material is clearly birefringent, with large variations between the different inserts. Therefore, birefringence is clearly not an accurate measurement for the quantification of biofilm. The variation in biofilm volume between samples in batch 1 is seemingly absent, most likely due to the short growth period and low biofilm volume. Therefore, it is not possible to determine the effect of chlorine on biofilm growth from these samples.

For batch 2, the aim was to investigate the effect of AOC concentration on biofilm growth. Unlike batch 1, biofilm was clearly present in the structural images. It is possible to quantify the thickness of this biofilm by finding the distance between the surface of the insert and the top of the biofilm. Samples without biofilm have a lower mean thickness and a lower standard deviation. Sample 3 had the highest average thickness of 16.6 µm, while sample 2 has the thinnest biofilm with an average thickness of 13.1 µm. These results concur with our hypothesis, where the lowest biofilm volume is expected in Sample 2 and the highest biovolume in Sample 3. Therefore, we can conclude that a higher AOC concentration leads to a higher biofilm growth.

The average thickness is often used in OCT imaging of biofilm as a quick and simple indicator of biofilm growth [4]. The biofilm samples here were grown in drinking water pipes, where a low volume of bacteria is expected. This, coupled with the short growth duration, meant that

it was not possible to detect very thin biofilms in batch 1 with accuracy; the algorithm used did not produce large enough differences between surfaces with biofilm and those without. However, in batch 2, we were able to detect biofilms as thin as 13.1 µm.

Biofilm growth would not be distributed uniformly over the insert area, so it was also possible that the areas imaged coincidentally have a lower biofilm volume. The very thin biofilm on the surface of the insert and the Fresnel reflections present resulted in difficulty in determining the biofilm-insert interface needed for calculating the thickness. There was also a lack of positive control due to apparent time constraints. Future work could focus on constructing better algorithms to accentuate these differences and imaging samples with thicker biofilm for comparison as positive control.

References

[1] H.C. Flemming, G. Schaule, T. Griebe, J. Schmitt, and A. Tamachkiarowa, “Biofouling—the Achilles heel of membrane processes,” Desalination, **113**(2-3), 215-225 (1997).

[2] C. Dreszer, A. D. Wexler, S. Drusová, T. Overdijk, A. Zwijnenburg, H.-C. Flemming, J. C. Kruithof, and J. S. Vrouwenvelder, “In-situ biofilm characterization in membrane systems using Optical Coherence Tomography: Formation, structure, detachment and impact of flux change,” Water Res. **67**, 243–254 (2014).

[3] S. Chellam, J.G. Jacangelo, T.P. Bonacquisti, and B.A. Schauer, “Effect of pretreatment on surface water nanofiltration,” J. Am. Water Work. Assoc. **89**(10), 77-89 (1997).

[4] M. Wagner, and H. Horn, “Optical coherence tomography in biofilm research: a comprehensive review,” Biotechnol. Bioeng. **114**(7), 1386-1402 (2017).

[5] M. Piculell, C. Suarez, C. Li, M. Christensson, F. Persson, M. Wagner, M. Hermansson, K. Jönsson, and T. Welander, “The inhibitory effects of reject water on nitrifying populations grown at different biofilm thickness,” Water Res. **104**, 292-302 (2016).

[6] M. Wagner, D. Taherzadeh, C. Haisch, and H. Horn, “Investigation of the mesoscale structure and volumetric features of biofilms using optical coherence tomography,” Biotechnol. Bioeng. **107**(5), 844-853 (2010).

[7] P. Deines, R. Sekar, P.S. Husband, J.B. Boxall, A.M. Osborn, and C.A. Biggs, “A new coupon design for simultaneous analysis of in situ microbial biofilm formation and community structure in drinking water distribution systems,” Appl. Microbiol. Biotechnol. **87**(2), 749-756 (2010).

[8] K.E. Fish, and J.B. Boxall, “Biofilm microbiome (re)growth dynamics in drinking water distribution systems are impacted by chlorine concentration,” Front. Microbiol. **9**, 2519 (2018).

[9] F.C. Pick, K.E. Fish, and J.B. Boxall, “Assimilable organic carbon cycling within drinking water distribution systems,” Water Res. **198**, 117147 (2021).

Chapter 7: Conclusions

This thesis chronicles the development of a MIR-OCT system and various applications of NIR-OCT.

With regards to the development of MIR-OCT, the ultimate goal is to build a swept-source system with a commercial ECQCL light source, using heterodyne detection to improve the SNR. To this end, we have characterized the sources of noise within the system: quantization noise from the ADC, shot noise from the detectors and RIN of the laser. We have first measured the noise spectral density of the ADC and the HgCdTe photovoltaic detectors, which are 2.8 pW/√Hz and 21.4 pW/√Hz respectively over a bandwidth of 100MHz.

The RIN of the laser is the most prominent source of noise in such a system and much of the focus of this chapter of the thesis has been to find possible methods to reduce RIN. The lowest possible value of RIN, measured with a soldering iron as a source of continuous MIR radiation, is -123 dB/Hz using a ±2V input voltage range. This shows that the "RIN" measured is actually composed of the true RIN plus the detector and ADC noise. When the laser is made to emit at a fixed wavelength (λ=7.1μm), with pulses of 1MHz repetition rate and 50ns pulse width, the RIN measured is -97dB/Hz. By using pulse-to-pulse normalization with two paired detectors, the RIN measured is reduced by 15dB/Hz to -115dB/Hz. RIN can also be reduced by using a higher pulse repetition rate. However, the effect of changing pulse parameters on RIN is limited by the duty cycle limit. Due to beam divergence, there was difficulty in focussing the laser beam onto the detector. This was mitigated by using aspheric lenses to focus the beam onto the detectable area, and then using neutral density filters or iris diaphragms to

avoid saturating the detector. The next steps in MIR-OCT development include quantifying RIN while sweeping the laser and measuring the interferogram of a biological sample such as skin.

Next, we investigate the feasibility of using PS-OCT to quantify the severity of striae distensae (SD). To do this, we used the PS-OCT to measure the birefringence of SD-affected skin and the adjacent visually normal skin. Image processing of the PS-OCT raw data produces en-face images of the estimated tissue birefringence. From these en-face images, four different metrics of birefringence were used to quantitatively compare between samples: mean, median, 75^{th} and 90^{th} percentile values. Using these metrics, we have shown that striae-affected skin is significantly different (p<0.001) from visually normal skin. Among the various metrics used, the 90^{th} percentile value showed the largest standard deviation among striae samples compared to other metrics, indicating that it is potentially the best metric for differentiating SD severity. The PS-OCT measurements are then compared to subjective visual scores obtained from digital dermoscopy photographs. We have demonstrated that there is a loose correlation between tissue birefringence percentile scores and the subjective visual scores.

One limitation of this study is the large variation in striae severity between patients, which depends on many factors such as genetics. Moreover, the differences in tissue birefringence between SD skin and visually normal skin were not large enough to place an unknown sample into either category with high accuracy. This could be because visually normal samples were collected from a location adjacent to the striae. Therefore, more data is needed from a control group of healthy volunteers to determine the standard of tissue birefringence for healthy skin. Another limitation is that there was a limited number of samples for striae rubra compared

to stria alba. Furthermore, samples with striae rubra are more likely to be given a higher visual score. Thus, we were unable to differentiate between the two types of striae with high statistical confidence. More samples of striae rubra are needed. Future work would include collecting data from healthy volunteers and using Jones matrix PS-OCT systems, which would give more insight into the spatial variation of the local birefringence and optic axis.

Thirdly, we investigate the effect of acid erosion on tooth demineralisation and whether treating teeth with stannous-containing fluoride toothpaste or tooth mousse with CPP-ACP before acid challenge helps to protect against dental erosion. Previously, the extent of dental erosion in OCT structural images was quantified by measuring the height of the enamel before and after acid treatment. However, the strong acid treatment needed to change the enamel thickness is not reflective of in vivo conditions. Calculating the slope of the reflectivity profile is a more reliable way of quantifying tooth demineralisation after a weaker acid treatment. We initially aimed to investigate whether pre-treating teeth with stannous-containing fluoride toothpaste or tooth mousse with CPP-ACP can protect against erosion. However, the results show that the initial measurements of peak reflectivity and slope of reflectivity determine the magnitude of change. As the teeth samples between different treatment groups were not sorted based on their initial reflectivity readings, we were unable to draw any conclusions about the effects of toothpaste or tooth mousse on tooth demineralisation.

Overall, we have demonstrated that even with a weak acid treatment, it is possible to quantify and potentially monitor the demineralisation of teeth. Calculating the slope seems to be a more reliable method of quantification, as there is a greater correlation between the initial readings and the change in readings. Regardless of the quantification method used, the results show that the initial peak reflectivity and slope before treatment is an important factor

in determining the magnitude of reflectivity changes after treatment. Thus, it is recommended that future studies take this into consideration when designing experiments.

The limited sample size of 21 teeth is the key limitation of this study, leading to inconclusive results regarding the effect of toothpaste and tooth mousse on dental erosion. This is an in vitro study and more studies are necessary to determine whether teeth display similar results in vivo. Possible future work includes comparing the use of OCT reflectivity to previous methods such as profilometry and surface hardness measurements.

In botany, we aimed to investigate the stability of plant petiole diameter measurements using OCT. We have demonstrated that spectrometer-based OCT can accurately track changes in the diameter of plant petioles, with an accuracy of 0.7 µm over a measurement bandwidth of 1.45 Hz for a plant specimen that has been completely dehydrated. When a plant petiole is undergoing changes to its diameter such as dehydration, the accuracy is reduced to 1.5 µm over a measurement bandwidth of 1.39 Hz. Lastly, we measured the stability of diameter measurements on a plant in vivo and attained an accuracy of 1.2 µm over a bandwidth of 0.9 Hz. Using moving time averaging windows of 25 and 100 B-scans reduces the standard deviation of the random noise to 0.7 µm and 0.5 µm respectively. This improves the accuracy of the measurements at the cost of a reduced frame rate.

The greatest limitation to this study is the limited number of specimens available. As the plant initiates a wounding response once a petiole is removed, it is not possible to repeat experiments on the same specimen to test for reliability. A follow-up to this study measures changes to the petiole diameter after an adjacent leaf has been wounded by a 30s-long laser pulse from an 800nm 6W laser. The algorithm used is an improvement to the algorithm used here, as it can track displacements in both the z and x directions. The results conclusively

show that OCT is able to detect 10-30 µm changes to the central vein diameter over the course of 10mins.

With regards to biofilm, we aimed to determine whether there is a minimum detectable limit when a spectrometer-based OCT is used for the quantification of biofilm thickness. Concurrently, if biofilm could be detected in the samples, we also investigated whether a lower concentration of chlorine or a greater concentration of AOC causes thicker biofilm build-up. We have shown that the insert material made from HDPE is clearly birefringent with large variations between different inserts. Therefore, birefringence cannot be used to help quantify the biofilm present. As the biofilm samples were grown in drinking water pipes, very thin biofilms are expected. For batch 1, where the chlorine concentration was varied, we were unable to detect any biofilm. For batch 2, where samples were grown with different AOC concentrations, there was a significant difference (p-value<5%) between samples with and without biofilm. Samples without biofilm have a mean thickness of around 11.6 µm, while samples with biofilm have a mean thickness which varies from 13.1 µm to 16.6 µm. We were thus able to show that a higher concentration of AOC lead to a higher biofilm growth.

There are a few limitations to this study. Firstly, the insert material, HDPE, is highly reflective, making it difficult to discern the biofilm-insert interface. Due to surface Fresnel reflections, the algorithm used calculates a higher-than-expected biofilm thickness, even in samples where no biofilm is present. Biofilm growth would not be distributed uniformly over the insert area. It is possible that the area imaged coincidentally has a lower biofilm volume. Future work includes finetuning the algorithm to mitigate these issues and imaging samples with thicker biofilm as a positive control.